APPROVAL SHEET

Title of Dissertation: Design, Modeling, Analysis, Control and Testing of an Infinitely Variable Transmission

Name of Candidate: Xuefeng Wang
Doctor of Philosophy, 2017

Dissertation and Abstract Approved:

Weidong Zhu
Professor
Mechanical Engineering

Date Approved: _____

NOTE: *The Approval Sheet with the original signature must accompany the thesis or dissertation. No terminal punctuation is to be used.

ABSTRACT

Title of Document: DESIGN, MODELING, ANALYSIS, CONTROL AND TESTING OF AN INFINITELY VARIABLE TRANSMISSION

Xuefeng Wang, Ph.D., 2017

Directed By: Professor, Weidong Zhu, Mechanical Engineering

A novel infinitely variable transmission (IVT) based on scotch yoke systems is designed to provide a continuously varied output-to-input speed ratio from zero to a specified value, which can be widely used in wind turbine and vehicle applications. Its zero-speed-ratio-start-up feature and scalability are especially suitable for construction or agriculture vehicles. The IVT consists of a pair of noncircular gears and the main body including two modules: an input-control module and a motion conversion module; the speed ratio is changed in the motion conversion module with use of scotch yoke systems. The Lagrangian approach is used to develop its dynamic model that can be used to design a robust and efficient controller, and the steady-state solution of the IVT is obtained using the incremental harmonic balance (IHB) method. A modified IHB method is developed here to significantly increase the computational efficiency and reduce the derivation complexity comparing with the classic IHB method, where the residual is approximated by the fast Fourier transform,

and Jacobian matrix is approximated by Broyden's method. A time-delay feedback controller combined with an open loop control is used for the IVT to stabilize the system and adjust its average input speed to a desired value for a vehicle application. Local stability of the system at the equilibrium can be proved by the stability of its linearized dynamic equation that is a time-delay linear time periodic (LTP) system, and its stability is numerically evaluated by converting the time-delay LTP system to a partial differential equation without time delay. A prototype of the IVT is manufactured and assembled. Functionality of the IVT is validated and parameter estimation is conducted for use in the design of the controller, and driving tests using feedback control are conducted to examine the performance of the controller.

DESIGN, MODELING, ANALYSIS, CONTROL AND TESTING OF AN INFINITELY VARIABLE TRANSMISSION

By

Xuefeng Wang

Dissertation submitted to the Faculty of the Graduate School of the
University of Maryland, Baltimore County, in partial fulfillment
of the requirements for the degree of
Doctor of Philosophy
2017

Table of Contents

Table of Contents ii
List of Tables iv
List of Figures v
Chapter 1: Introduction 1
1.1 Motivation and Background 1
1.2 Introduction to a New Gear IVT 5
1.3 Outlines and Contributions 9
Chapter 2: Mechanism and Kinematics of the New IVT 12
2.1 Crank-slider Based Geared IVT (GIVT) 12
2.1.1 Principle of the GIVT 12
2.1.2 Layout and Overview of the GIVT 13
2.1.3 Input-control Module of the GIVT 15
2.1.4 Motion Conversion Module of the GIVT 17
2.1.5 Noncircular Gears of the GIVT 24
2.1.6 Direction Control Module of the GIVT 27
2.2 Scotch-Yoke Based Geared IVT (SGIVT) 29
2.2.1 Principle, Layout and Overview of the SGIVT 30
2.2.2 Input-control Module of the SGIVT 34
2.2.3 Motion Conversion Module in the SGIVT 37
2.2.4 Noncircular Gears in the SGIVT 45
2.3 Modifications for the SGIVT 49
Chapter 3: Modified Incremental Harmonic Balance (IHB) Method 55
3.1 Introduction to the IHB Method 55
3.2 Modified IHB Method 59
3.2.1 IHB Method in Solving Duffing's Equation 59
3.2.2 Modified IHB Method 63
3.2.3 Arc-length Method for the Modified IHB Method 67
3.2.4 Stability of Periodic Solutions 71
3.2.5 Bifurcations of Mathieu-Duffing Equation by IHB Method 73
3.3 Spatial and Temporal Harmonic Balance (STHB) Method 78
3.3.1 Introduction to the STHB Method 78
3.3.2 Preliminaries for Deriving the STHB Method 81
3.3.3 The STHB Method for a Fixed-fixed String with Nonlinearity 85
3.3.4 Stability Analysis of Periodic Responses and Results 91
3.3.5 The STHB Method for a String with Complex Boundary Condition 95
Chapter 4: Dynamics, Controller Design and Testing of the IVT 99
4.1 Dynamic Model of the IVT System 99
4.2 Dynamic Analysis of the IVT System for Design of its Open Loop Control . 105
4.2.1 Design of an Open Loop Control using the IHB Method 105
4.2.2 Existence and Convergence of Periodic Solutions for the IVT System .. 111
4.3 Design of an Integral Time-Delay Feedback Control for the IVT System 122
4.4 Testing of the SGIVT 132
4.4.1 Experimental Setup 132

4.4.2 Experimental Validation of Average and Instantaneous Speed Ratios ... 133
4.4.3 Driving test of the SGIVT ... 137
Appendix A: Derivation of Eq. (121) from Eq. (120) ... 144
Appendix B: Derivation of Eq. (174) ... 145
Appendix C: Derivation of the Linear Time-Periodic System in Eq. (179) ... 147
References ... 149

List of Tables

Table 1 Parameters of the IVT

List of Figures

Figure 1 Schematic for the basic principle of the GIVT and the process to change the output-to-input speed ratio

Figure 2 Layout of the GIVT

Figure 3 Motion flow of the GIVT; connecting gears 1 through 5 are numbered in the figure

Figure 4 (a) Three-dimensional (3D) model of the input-control module, and (b) the schematic of the input-control module

Figure 5 (a) Schematic of the motion conversion module, and (b) the 3D model of the motion conversion module

Figure 6 Schematic of the crank motion when (a) the control speed is zero or (b) the input speed is zero; (c) the 3D model of the crank and crank gears

Figure 7 3D model of the driver part and output part

Figure 8 Schematic of the crank-slider motion

Figure 9 (a) Speed ratios of a crank-slider system and the motion conversion module, and (b) the average speed ratio of the GIVT

Figure 10 Reduced speed ratios with and without noncircular gears

Figure 11 Pitch profiles of NG1 and NG2 with D=10 mm

Figure 12 (a) Schematic of the direction control, and (b) the 3D model of the direction control

Figure 13 Schematic illustrating the principle of the SGIVT with scotch yoke systems

Figure 14 Difference between the GIVT and SGIVT

Figure 15 Layout of the SGIVT

Figure 16 Schematic diagram of the SGIVT

Figure 17 (a) 3D model and (b) schematic diagram of the input-control module

Figure 18 Structure of the second planetary gear set; the first planetary gear set has the same structure

Figure 19 (a) 3D model of the motion conversion module and (b) schematic diagram of the input motion conversion part

Figure 20 Structure of the first scotch yoke system; the second scotch yoke system has the same structure

Figure 21 Schematic of the first and second scotch yoke system

Figure 22 Structure of the output motion conversion part of a scotch yoke system

Figure 23 (a) Theoretical pitch profiles, (b) approximated pitch profiles with segments of circular arcs, and (c) tooth profiles based on the approximated pitch profiles in (b)

Figure 24 Speed ratios with the noncircular gears generated by the exact and approximated functions

Figure 25 Modification of the variant of the SGIVT with small pins replaced by large rollers

Figure 26 Layout of a variant of the SGIVT; two highlighted transparent gears are noncircular gears, parts on three shafts in the top layer constitute the input-control module, and parts on two shafts in the bottom layer constitute the motion-conversion module

Figure 27 Schematic of the principle of the variant of the IVT; two perpendicular arrows in the motion-conversion module indicate the 9 0 o phase difference between the two rollers.

Figure 28 Solutions of Duffing's equation from the modified IHB method and Runge–Kutta method

Figure 29 Amplitude-frequency response curve of Duffing's equation

Figure 30 Period-1 solution of Mathieu-Duffing equation with β =4.1906

Figure 31 Period-2 solution of Mathieu-Duffing equation with β =4.8390

Figure 32 Period-4 solution of Mathieu-Duffing equation with β =5.2508

Figure 33 Bifurcation diagram of Mathieu-Duffing equation

Figure 34 Frequency-response curves for the case of weak nonlinearity with k_d=10 ; N=5 and 10

Figure 35 Frequency-response curves for the case of weak nonlinearity with k_d=30 ; N=5 and 10

Figure 36 Frequency-response curves for cases of the string with fixed-fixed boundary conditions and fixed-spring boundary conditions

Figure 37 Values of f and f_θ

Figure 38 (a) Values of $\bar{r}$, (b) the boundary to distinguish different cases for the open loop control law

Figure 39 Comparison between steady-state solutions of ω from the modified IHB method and Runge-Kutta method

Figure 40 Boundary $\hat{\Gamma}$=0 compared with the boundary f_B=0

Figure 41 Analogy between a time-delay system and a distributed-parameter system without time delay

Figure 42 Maximum absolute eigenvalues of the transformation matrix

Figure 43 Histories of ω_a with and without the time-delay feedback control

Figure 44 Histories of ω_a with and without time delay

Figure 45 Histories of control variables *r* for the feedback control with and without time delay

Figure 46 Experimental setup of the SGIVT

Figure 47 Comparison of experimental and theoretical average speed ratios

Figure 48 Experimental speed ratio of the noncircular gears, experimental speed ratios of the SGIVT with and without the noncircular gears, and the theoretical speed ratio of the noncircular gears or that of the SGIVT without the noncircular gears

Figure 49 Block diagram of the controller for the SGIVT

Figure 50 Slope of linear regression from the measured speed of the DC motor and the angle of the stepper motor

Figure 51 Driving test results of the SGIVT; values of the angle of the stepper motor are scaled down by 100, and those of the input voltage are scaled up by 5

1 Introduction

1.1 Motivation and Background

Transmissions are widely used in a variety of different applications, such as agricultural, industrial, construction, and automotive equipment. They provide a speed-torque conversion by using the principle of mechanical advantage, where gear reduction is mostly provided to increase the output torque. On the other hand, a high speed ratio may be used as an overdrive to increase the output speed.

In wind turbine applications, the power extracted from the wind by the turbine rotor is affected by the tip ratio, which is the ratio of the tip speed of the blades and the wind speed [1]. To achieve the maximum efficiency of a wind turbine, the speed of the blades varies with the wind speed. A transmission used in a wind turbine converts a slow and high-torque rotation from a turbine rotor to a high-speed rotation of a generator with an input-to-output speed ratio from 1:60 to 1:200 [2]. There are four types of wind turbines using a traditional transmission with a fixed gear ratio [3]. Type A is a constant speed wind turbine, with an asynchronous squirrel cage induction generator directly connected to the grid. This type of wind turbine can only operate in a very narrow range of the wind speed. Type B is a variable speed wind turbine with variable rotor resistance. The generator torque is controlled to make the blades rotate at the maximum efficiency under the cut-off wind speed and stop the blades above the cut-off speed [4]. Type C is a variable speed wind turbine that uses a doubly-fed induction generator with a partial-scale power converter in the rotor circuit to keep the current frequency in the stator constant [5]. Type D is a variable speed wind turbine that uses a synchronous generator connected to the grid

through a full-scale power converter, which can convert variable frequency current to constant frequency current [6]. In addition, a variable speed wind turbine with a variable speed converter has been developed [7]. The speed converter can provide a continuously varied speed ratio to make the generator rotate at a constant speed and the blades rotate at the maximum aerodynamic efficiency. This type of wind turbine can operate at the maximum efficiency under a variable wind speed without using a power converter, which can increase the system efficiency and durability [7].

For a vehicle application, a transmission is used to achieve a good output performance of an engine. The engine typically operates over a range of 600 RPM to 7000 RPM, while wheels of the car rotate from 0 RPM to 1800 RPM. To achieve a large start-up torque, the transmission converts a middle engine speed to a low vehicle speed, since the highest torque of an engine is usually achieved at a middle speed. When a car is driven at a highway speed, the transmission will work in the overdrive stage to achieve a high output speed. Another benefit of a multi-ratio transmission is to maintain good fuel efficiency at different speeds. Hence, a multi-ratio transmission, such as a manual transmission or an automatic transmission, is required for vehicle applications [8]. The multi-ratio transmission can only allow a few distinct gear ratios to be selected, which cannot give optimal fuel efficiency selections for a continuously changing speed. A continuously variable transmission (CVT) is a transmission that can provide a continuously varied speed ratio between its minimum and maximum values, which allows the engine to rotate at its most efficient speed for a range of vehicle speeds. Another advantage of the CVT is to facilitate the transmission to smoothly operate while changing the speed ratio, and no sudden jerk occurs.

There are several types of CVTs available on the market [9]. The most commonly used CVT is a variable-diameter pulley (VDP) [10]. In the VDP, there are two V-belt pulleys that are split in a direction perpendicular to their axes of rotation with a V-belt running between them. The gear ratio is changed by moving two sections of one pulley closer together and two sections of the other pulley farther apart. Due to V-shaped cross-sections of the belt and the pulley, the effective diameter of one pulley that the belt rides on increases, and that of the other pulley to be ridden by the belt decreases; the length of the belt does not change, and the simultaneous change of the two effective diameters causes the change of the speed ratio. There is another type of CVTs called the toroidal or roller-based CVT. It is made up of discs and rollers that transmit power between the discs. One disc is the input and the other is the output, and they do not touch. Power is transferred from one side to the other by rollers. When the rollers contact the two discs at the same diameter locations, it gives a 1:1 gear ratio. When the rollers are moved and rotated to change their contact positions at two different diameter locations on the two discs, the gear ratio will be something other than 1:1. The toroidal CVT can transmit more power due to a large number of parallel sets of inter-wheels [11]. There are other types of mechanical CVTs such as conical CVTs [11]. They share the same disadvantages of mechanical CVTs: the torque capability is limited by the strength of their medium (chain, belt, or roller), and the ability to withstand friction wear between the pulleys and the chain or the discs and the rollers [12]. To increase the torque capability, hydraulic CVTs are designed [13, 14]. A hydraulic CVT with a variable displacement pump and a hydraulic motor is referred to as a hydrostatic CVT, and power is transmitted by hydraulic fluid. The change of the

speed ratio of the CVT is achieved by changing the displacement of the pump. This type of CVTs can be used to transmit a large torque, and has higher efficiency than the mechanical CVTs, since it eliminates efficiency loss due to friction components [13, 14]. If the hydraulic pump and motor are not hydrostatic, the hydraulic CVT is called a hydrodynamic CVT. The hydrodynamic CVT is used in wind turbine [15] and large-torque vehicle [14] applications. This concept is also used as a torque converter in vehicles to replace mechanical clutches to improve drivability, but the efficiency of the torque converter significantly decreases with its speed ratio due to energy loss in fluid and consequently the total efficiency of the vehicle running at a low speed is significantly decreased [16]. An electric variable transmission (EVT), which is also called a power split transmission, is a transmission that achieves the CVT action by splitting the engine power into mechanical power to drive vehicles and electric power to charge/discharge a generator/motor [17]. The EVT can achieve high engine efficiency, but it cannot deliver a large torque or achieve a good start-up acceleration, and the efficiency of the generator/motor is low [18]. A complex control and an electrical system are also required to combine the power from the engine and motor.

A specific type of CVTs is called an infinitely variable transmission (IVT), where the output-to-input speed ratio ranges from zero to a certain value. At the zero speed ratio, the engine shaft can be idling while the vehicle is static; the vehicle speed can be increased by continuously increasing the speed ratio. This property can eliminate the use of clutches, which can improve drivability by eliminating sudden jerks, or increase the efficiency at low speeds by eliminating a hydrodynamic torque converter in CVTs. There are some types of IVTs that have been studied.

A type of IVTs that requires eight pairs of noncircular gears, which decreases the transmission efficiency and reliability, to achieve a continuously varied speed ratio from zero by changing the phase difference between two pairs of noncircular gears is described in [19]. It is difficult to control the engagement of the noncircular gears when it operates at a high frequency. A variable speed transmission with a variable orbital path [20] is another type of IVTs. It changes the linear velocity of driving gears by increasing or decreasing the size of the orbital path, and the changed linear velocity is transferred to driven gears in the form of a gear ratio change. This type of IVTs needs a number of bevel gears, which will significantly lower the efficiency and durability and affect compactness. Reference [21] describes an IVT with two drivers that convert a concentric motion of the output shaft through one-way bearings, which is designed to change the speed ratio by varying eccentricity of cams. This type of IVTs has been studied in [22]; its main disadvantage is that the peak-to-peak instantaneous output speed variations of the IVT are very large (29% of its average output speed). Also, two small pins used in the design limit the maximum torque, and reciprocating motions of drivers introduce large vibrations.

1.2 Introduction to a New Geared IVT

A geared IVT (GIVT) using crank-slider systems with an adjustable crank length is described in [23]. It has a higher total efficiency than a CVT at a low speed ratio, since the torque converter is eliminated. It is scalable to transmit a large torque, and is durable and compact. The innovative design of the GIVT that uses rack-pinion systems to change its speed ratio makes it possible to apply a pair of noncircular gears to reduce the speed variations introduced by reciprocating motions of the

crank-slider systems. Another benefit of this design is that the holding toque for its control actuator is small when the crank length is constant, since the output torque of the GIVT can be almost evenly split into two parts and the holding torque is the difference of the two parts, which cancel each other. However, the disadvantage of the GIVT is that its output speed variations cannot be eliminated for all crank lengths by using a pair of noncircular gears, since the shape of the speed ratio of the GIVT changes with the crank length. To overcome this drawback, a novel GIVT that uses scotch yoke systems, called the SGIVT, is introduced in [24]. By using scotch yoke systems instead of crank-slider systems, the shape of the speed ratio is independent of the crank length, and the speed variations can be theoretically eliminated for all crack lengths by a pair of noncircular gears. In the design of the SGIVT, pins are used to transmit power in slots and segmented cantilever beams are installed to hold the pins. If assembly error in position dimensions of the segmented cantilever beams are large, the pins may have large misalignment with the slots, and efficiency to transmit power is significantly reduced. In a variant of the SGIVT [25], pins are replaced by large rollars so that they can be installed on an entire shaft, which yields higher assembly precision and strength than installing pins on segmented cantilever shafts.

To obtain the maximum efficiency, the speed ratio of a transmission highly depends on the speed of a prime mover, such as an engine or a wind turbine [1, 26]. Thus, a controller of the IVT to steer the speed of the prime mover to a prescribed value by adjusting the speed ratio of the IVT should be developed. A gain-scheduled feedback control combined with an open loop control based on steady-state responses of the prime mover is usually used in the vehicle application

[27, 28], and there are many feedback control methods used for the CVT speed ratio control, including the adaptive control [9], the linearization feedback control combined with the proportional-integral-derivative control [29] and the optimal control [30]. For the IVT in [21], a gain-schedule feedback controller is developed in [22], and a similar contoller is used for the IVT in [24]. However, they are non-model based controller. In [25], a model-based gain-schedule feedback control with an open loop control is developed for the control of an IVT system including the IVT and a permanent magnetic DC motor as the prime mover. A nonlinear dynamic model of the IVT system is developed using Lagrange equation, and the open loop control, as well as the feedback control, can be designed with it. The motor speed that is governed by the dynamic model is influenced by the supply voltage of the motor, the output torque from a brake and the speed ratio of the IVT, where the speed ratio is the control variable. The goal of the open loop control is to develop a look-up table for choosing the speed ratio of the IVT so that the average of the motor speed at steady state can be the prescribed value for any supply voltage and output load. To develop the controller, dynamic analysis of the IVT should be conducted first. A dynamic model of the IVT in [24] shows that the speed of the prime mover at steady state is a periodic function [31]. To reduce the testing time for the generation of the look-up table [28], a modified incremental harmonic balance (IHB) method [32] is employed here to efficiently calculate the speed ratio in the table, which is a function of the supply voltage and output load.

An IHB method may fail when a periodic solution does not exist, and it can only predict local stability. Thus, analytical properties of the dynamic equation of the IVT system with the open loop control are studied in [25]. Existence of

a periodic function for the motor speed with a prescribed average is proved with use of Gronwall-Bellman Lemma [33], and convergence of the motor speed to the speed described by the periodic function is proved by Lasalle's invariant principle for periodic systems [34]. By transforming the independent variable of the dynamic equation of the IVT system from time to the motor angle, the dynamic equation is Lipchitz in the dependent variable and piecewise continuous in the independent variable, which proves uniqueness of the periodic solution for the motor speed [35].

Since the dynamic equation of the IVT system is periodic and the motor speed at steady state is periodic, great control effort due to oscillation in the control variable is needed to make the instantaneous speed constant. For the control purpose, a time-periodic system is usually simplified by a time-invariant system, such as the engine speed control in [28, 36], where the speed in the time-invariant system is an approximated average of the speed in the time-periodic system. However, since the current engine speed is used as the feedback variable, oscillation still occurs in the control variable and engine speed [36]. In [25], a time-delay variable that is the average of the motor speed over a revolution prior to the current angular position is used as the feedback variable, which can eliminate oscillation in the control variable and reduce the control effort, and the goal of the feedback control is to make the average speed converge to the prescribed value. With the time-delay feedback control, the dynamic equation of the IVT system is a time-delay system. Stability of a linear time-delay system can be analyzed with use of linear matrix inequalities [37, 38]. For a nonlinear time-delay system, stability is usually analyzed by constructing Lyapunov functions [39, 40]. Besides analytical methods above, numerical methods, such as Chebyshev collocation method [41], the semi-discretization

method [42] and the temporal finite element analysis method [43], are usually used to obtain responses and analyze stability of time-delay systems. A new point of view for time-delay systems is proposed in this work, i.e., a time-delay system can be analogous to a distributed-parameter system without time delay. Based on this point of view, all numerical methods that are used for solving distributed-parameter systems are equivalent to those for solving time-delay systems, and the spectral Tau method [44] is used here to analyze the IVT system with the time-delay feedback control.

1.3 Outlines and Contributions

At first, mechanism of the new IVT is illustrated in Chapter 2. There two types of the IVT that are described in Sec. 2.1 and Sec. 2.2. For each type of the IVT, the principle and the overview of the layout are shown first. Then their design details are described module by module in the IVTs. Meanwhile, kinematics for each type of the IVT are developed. In Sec. 2.3, an updated version of the IVT in Sec. 2.2 is introduced to improve the performance of the system, and its kinematic relationship is given. In Chapter 3, nonlinear dynamic analysis methods for single- and multi-DOF systems and distributed-parameter systems are illustrated. In Sec. 3.2, the basic method that is called the modified IHB method for analyzing periodic solutions of single-DOF systems and their stability is developed, comparisons between the modified IHB method, the classic IHB method and Runge–Kutta method are conducted, and bifurcations for nonlinear systems are studied by the modified IHB method. In Sec. 3.3, the basic modified IHB method is successfully extended to analyze periodic solutions of distributed-parameter systems, where the method is

called the STHB method. At last, the STHB method is used to solve a distributed-parameter systems with complex boundary conditions. In Chapter 4, a dynamic model of the IVT is developed first. With use of the nonlinear dynamic analysis method shown in Chapter 3, the dynamic system of the IVT is analyzed, existence and convergence of the solution of the system is proved, and a model-based controller is developed in Chapter 4. At last, testings for a prototype of the IVT system are conducted to validate its functionality.

Contributions of the dissertation are in two aspects: the machine design and control, and the nonlinear dynamic system analysis. In the machine design and control area, an innovative design of the speed conversion mechanism with use of rack and pinion enables the IVT to change its speed ratio while it is rotating. Meanwhile, shapes of the output-to-input speed ratio of the IVT using this mechanism do not change with the average speed ratio. This property is of advantage to using a pair of noncircular gears to elinimate the instantaneous speed ratio of the IVT. In the development of the feedback controller combined with an open-loop control law for the IVT system, the IHB method is firstly used to generate the open-loop control law for a time-periodic system, and existence, convergence and uniqueness of the periodic solution of the system, which is the base of the open-loop control law, are proved mathematically. A time-delay feedback variable is intentionally used in the feedback controller to generate a more smooth control variable. In order to deal with the time-delay system, a new method that convert the time-delay system to a distributed-parameter system is developed. In the nonlinear dynamic system analysis, a modified IHB method is developed to solve the periodic solution of nonlinear single- and multi-DOF systems, which is almost a hundred times faster than

traditional methods, and its extension, the STHB method, is developed for solving partial differential equations, which is hundred times faster than traditional method and is very easy and convenient to automatically implement. To further increase the calculation speed, a semi-analytical approach to calculate Jacobian matrix for IHB and STHB methods is developed, which can be also used to analyze the stability of an ordinary or a partial differential equation.

2 Mechanism and Kinematics of the New IVT

2.1 Crank-slider Based Geared IVT (GIVT)

2.1.1 Principle of the GIVT

The basic principle of the GIVT is to convert an input rotation of a crank to a slider motion in a crank-slider system, and then convert the slider motion to an output rotation of an output gear by a rack-pinion meshing, as shown in Fig. 1. By changing the crank length, the amplitude of the slider motion is changed. Hence, if the crank rotation speed that is transmitted from the input rotation is constant, the average slider speed is changed. Consequently, the average output rotation speed is changed and the average output-to-input speed ratio is changed.

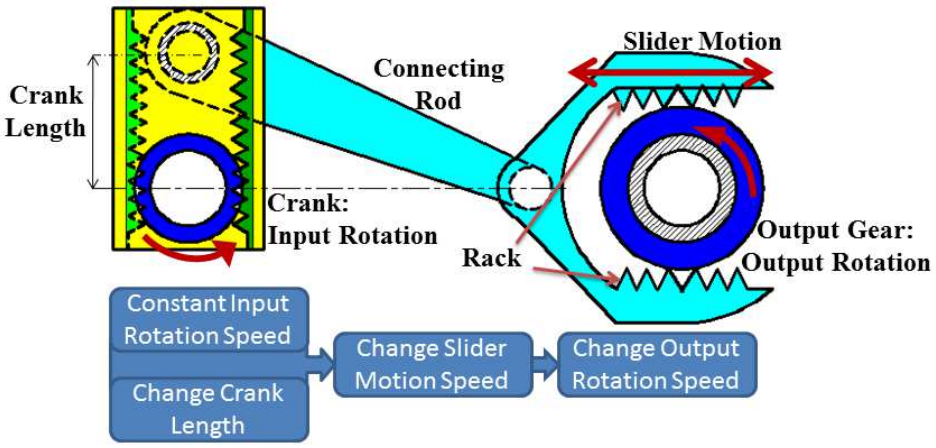

Figure 1: Schematic for the basic principle of the GIVT and the process to change the output-to-input speed ratio

2.1.2 Layout and Overview of the GIVT

The GIVT consists of two modules: a motion conversion module and an input-control module, and seven shafts: three main shafts, which are the input shaft, the crank shaft, and the output shaft, two control shafts, which are the active control shaft and the idler control shaft, and two transmitting shafts, which are transmitting shaft A and transmitting shaft B, as shown in Fig. 2. The motion conversion module that rides on the crank shaft and the output shaft consists of four crank-slider systems, which can make the output speed smoother, as discussed later in the paper. The input-control module before the motion conversion module is used to combine the input speed that is transmitted to cranks, and two control speeds with different directions to adjust the crank length, so that the crank length can be changed while the crank is rotating, i.e., the speed ratio can be changed while the transmission is running. The input-control module rides on the input shaft, and two control speeds with different directions come from control gears on the active and idler control shafts. The combined speeds will be transmitted to cranks by two pairs of gears: connecting gear A meshed with connecting gear 1, and connecting gear B meshed with connecting gear 2, as shown in Fig. 3. The speed of connecting gear 1 is transmitted to connecting gear 3 and connecting gear 5 through transmitting shaft A, and the speed of connecting gear 2 is transmitted to connecting gear 4 through transmitting shaft B. Cranks are driven by gears attached to transmitting gears 1 through 5, and then drive output gears on the output shaft.

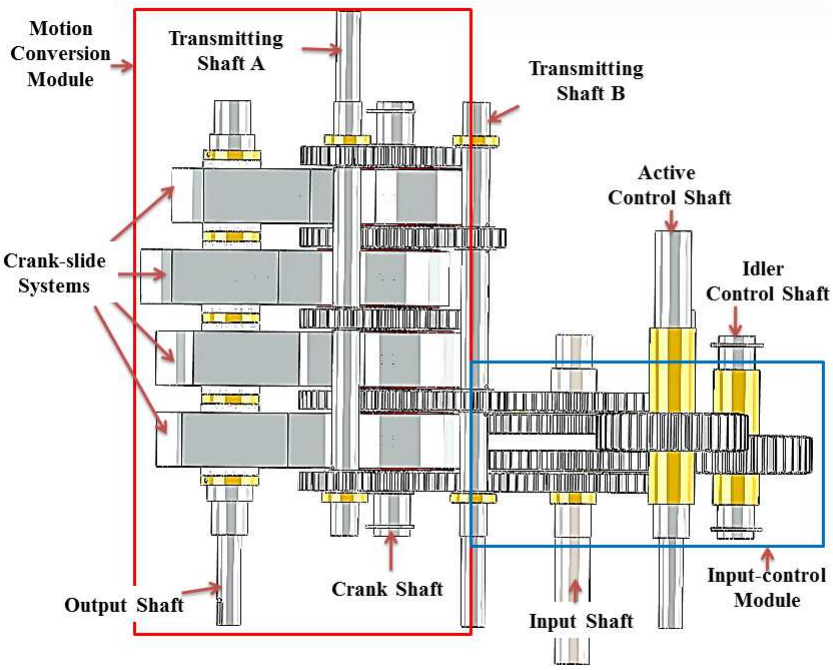

Figure 2: Layout of the GIVT

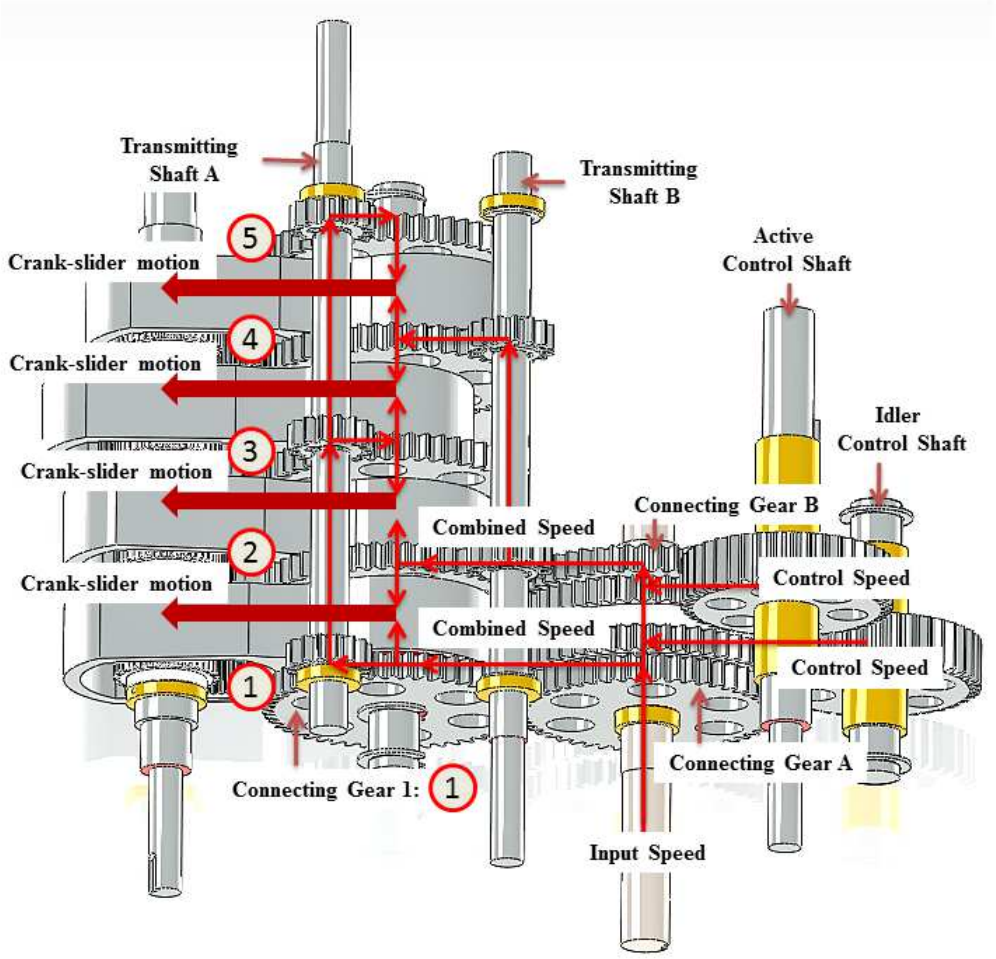

Figure 3: Motion flow of the GIVT; connecting gears 1 through 5 are numbered in the figure.

2.1.3 Input-control Module of the GIVT

In the input-control module, an active control gear splines on the active control shaft, and an idler control gear rides on the idler control shaft, as shown in Fig. 4. The active control shaft is driven by an actuator, such as a stepper motor, and

the speed of the active control gear is that of the stepper motor, which is called the original control speed denoted by ω_{c1}. The idler control gear is meshed with the active control gear, and its speed, which is called the opposite control speed denoted by ω_{c2}, is opposite to that of the active control gear. Since the two control gears have the same radius, the values of the two control speeds are the same, and $\omega_{c1} = -\omega_{c2}$.

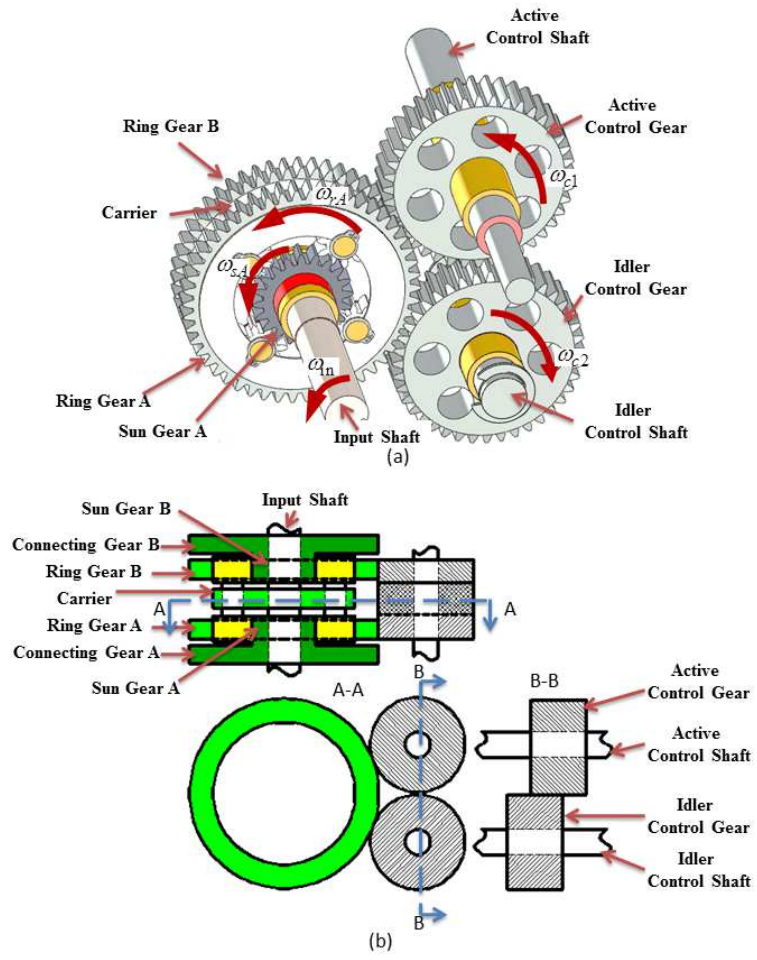

Figure 4: (a) Three-dimensional (3D) model of the input-control module, and (b) the schematic of the input-control module

There are two planetary gear sets riding on the input shaft. They have their own ring gears, sun gears, and planet gears, and they share a common carrier, as shown in Fig. 4. Each control gear connects to a planetary gear set by meshing with outside teeth of a ring gear. Since the gear ratio of the control gear over the ring gear is 1:3, the speed of a ring gear (Ring Gear A) meshed with the idler control gear is $\omega_{\mathrm{rA}} = -\omega_{c2}/3 = \omega_{c1}/3$, and that of the other ring gear (Ring Gear B) meshed with the active control gear is $\omega_{\mathrm{rB}} = -\omega_{c1}/3 = -\omega_{\mathrm{rA}}$. The carrier is fixed to the input shaft with an input speed ω_{in}. The speed of Sun Gear A ω_{sA} and that of Sun Gear B ω_{sB} are

$$\omega_{\mathrm{sA}} = \frac{2(r_{\mathrm{sun}} + r_{\mathrm{planet}})\omega_{\mathrm{in}} - (r_{\mathrm{sun}} + 2r_{\mathrm{planet}})\omega_{\mathrm{rA}}}{r_{\mathrm{sun}}} \tag{1}$$

$$\omega_{\mathrm{sB}} = \frac{2(r_{\mathrm{sun}} + r_{\mathrm{planet}})\omega_{\mathrm{in}} - (r_{\mathrm{sun}} + 2r_{\mathrm{planet}})\omega_{\mathrm{rB}}}{r_{\mathrm{sun}}} \tag{2}$$

where r_{sun} is the radius of the sun gear and r_{planet} is the radius of the planet gears. The speeds of Connecting Gear A and Connecting Gear B are ω_{sA} and ω_{sB}, respectively, since they are fixed to Sun Gear A and Sun Gear B, respectively.

2.1.4 Motion Conversion Module of the GIVT

The motion conversion module has four crank-slider systems, and each crank-slider system consists of three parts: the crank part, the output part, and the driver part, as shown in Fig. 5. A crank-slider system here is a modification of the standard crank-slider system in Fig. 1; the joint between the connecting rod and slider in Fig. 1 is eliminated, and the connecting rod and slider form an entire body, which is called a driver. With the modification, the slider moves along the direction of the

racks in the slider, which are called slider racks, and the driver that rotates around the output gear makes the output gear rotate.

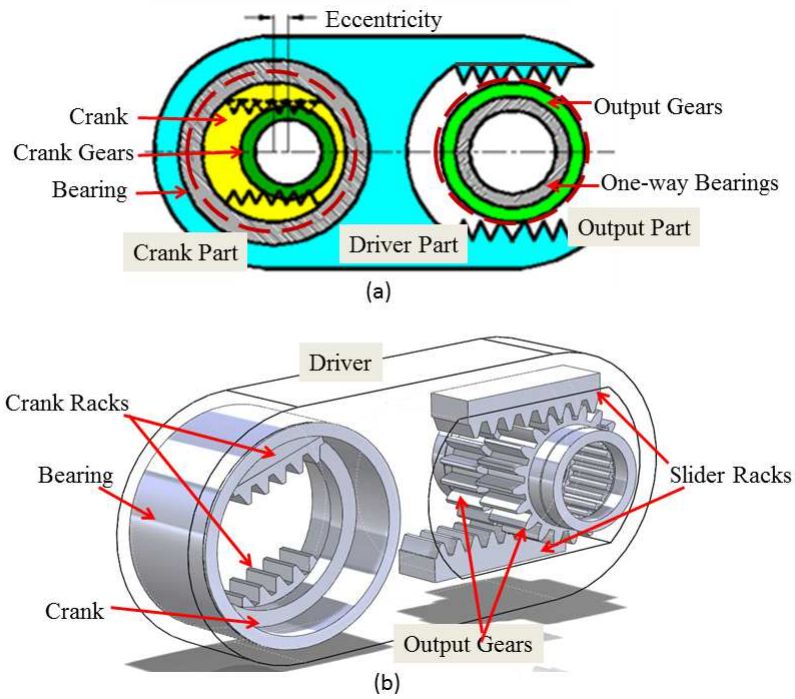

Figure 5: (a) Schematic of the motion conversion module, and (b) the 3D model of the motion conversion module

In each crank-slider system, two crank gears on the crank shaft are connected to two connecting gears, and are on two sides of the driver: crank gear A on the inner side and crank gear B on the outer side, as shown in Fig. 6(c). Two racks, called crank racks, are fixed face-to-face in the crank; crank rack A is meshed with crank gear A, and crank rack B is meshed with crank gear B. The shape of the crank is a cylinder, and it is installed in a hole of the driver through a bearing, so that it can freely rotate in the hole.

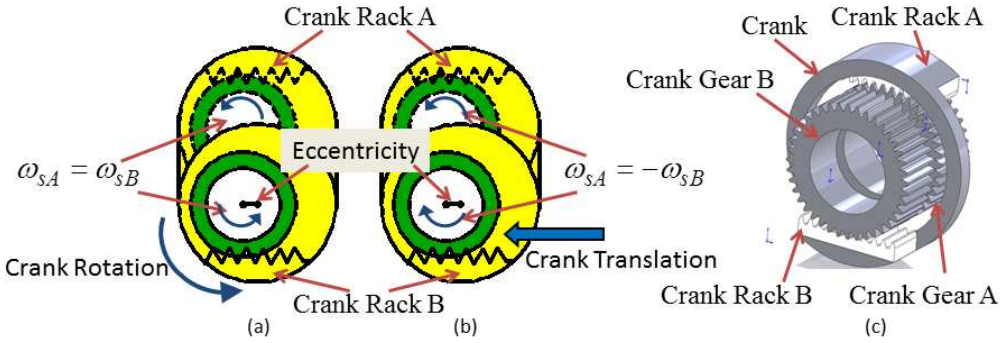

Figure 6: Schematic of the crank motion when (a) the control speed is zero or (b) the input speed is zero; (c) the 3D model of the crank and crank gears

The speed of connecting gears 1, 3, and 5 is that of connecting gear A, which is ω_{sA}, and the speed of connecting gears 2 and 4 is that of connecting gear B, which is ω_{sB}, as shown in Fig. 3. Hence, for each crank-slider system, the speed of one crank gear (e.g., crank gear A) is ω_{sA}, and that of the other crank gear (crank gear B) is ω_{sA}. If the control speed is zero, i.e., $\omega_{\mathrm{rA}}$and ω_{rB} are zero in Eqs. (1) and (2), respectively, two crank gears rotate at the same speed ($\omega_{\mathrm{sA}} = \omega_{\mathrm{sB}}$), and the crank also rotates at the same speed with crank gears, as shown in Fig. 6(a). If the control speed is nonzero and the input speed is zero, two crank gears rotate in opposite directions at the same speed ($\omega_{\mathrm{sA}} = -\omega_{\mathrm{sB}}$). Consequently, the crank translates along the direction of the crank racks without a rotation, which can change the eccentricity from the center of crank gears to that of the crank, as shown in Fig. 6(b). The eccentricity, which is the crank length, is denoted by r. When both the input speed and control speed are nonzero, the motion of the crank is the superposition of a rotation and translation, which enables the GIVT to change the

speed ratio while it is running. The rotation speed of the crank is

$$\omega_{\mathrm{crk}} = \frac{\omega_{\mathrm{sA}} + \omega_{\mathrm{sB}}}{2} \tag{3}$$

and the translation speed of the crank is

$$v_{\mathrm{crk}} = \frac{\omega_{\mathrm{sA}} - \omega_{\mathrm{sB}}}{2} r_{\mathrm{crk}} \tag{4}$$

where r_{crk} is the radius of crank gears. Time integration of the translation speed of the crank gives the eccentricity r.

One end of the driver rides on the crank through a bearing, and the other end has two racks fixed face-to-face in the driver, which are called slider racks. Slider rack A is on the inner side of the driver, and slider rack B is on the outer side of the driver, as shown in Fig. 7. There are two output gears installed on the output shaft through two one-way bearings. Output gear A is meshed with slider rack A, output gear B is meshed with slider rack B, and one-way bearings allow output gears to freely rotate only in the clockwise direction. Hence, when the driver moves leftward, output gear A freely rotates and output gear B drives the output shaft to rotate counterclockwise, and vice versa.

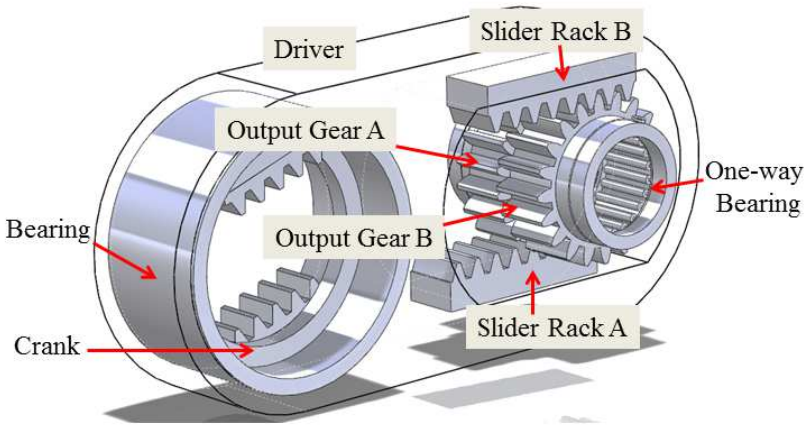

Figure 7: 3D model of the driver part and output part

To analyze the motion of the driver and output gears, a crank-slider system can be simplified by a schematic diagram in Fig. 8. The crank length is the eccentricity r, which has a fixed value. The centers of crank gears, the crank, and output gears are denoted by O_{crk}, O_c, and O_{output}, respectively. The crank rotation speed is $\omega_{\text{crk}} = \dot{\theta}$, where θ is the angle between $\overline{O_{\text{output}}O_{\text{crk}}}$ and $\overline{O_{\text{c}}O_{\text{crk}}}$, which is the input angle of the motion conversion module. The output gear rotation is a combination of the speed due to the translation of the driver along $\overline{O_{\text{output}}O_c}$ and that due to the rotation of the driver around O_{output}. The translation speed of the driver is l_2, where l_2 is the length of $\overline{O_{\text{output}}O_c}$; the rotation speed is $\dot{\theta}_s$, where θ_s is the angle between $\overline{O_{\text{output}}O_{\text{crk}}}$ and $\overline{O_{\text{output}}O_c}$. Speeds of output gear A and output gear B are $\dot{\theta}_s + \dot{l}_2/r_{\text{output}}$ and $\dot{\theta}_s - \dot{l}_2/r_{\text{output}}$, respectively, where r_{output} is the radius of output gears. The output speed transmitted to the output shaft is the maximum speed of the two output gears due to use of one-way bearings: $\dot{\theta}_s + |\dot{l}_2/r_{\text{output}}|$. The ratio of

the output speed of the crank-slider system to its input speed is

$$\frac{\omega_{\text{output1}}}{\omega_{\text{crk}}} = (\dot{\theta}_s + |\frac{\dot{l}_2}{r_{\text{output}}}|)\frac{1}{\dot{\theta}} = \frac{\dot{\theta}_s}{\dot{\theta}} + |\frac{\dot{l}_2}{\dot{\theta} r_{\text{output}}}| = \frac{d\theta_s}{d\theta} + \frac{1}{r_{\text{output}}}|\frac{dl_2}{d\theta}| \tag{5}$$

In the triangle $\triangle O_{\text{output}} O_c O_{\text{crk}}$, using laws of sines and cosines yields

$$\frac{d\theta_s}{d\theta} = \frac{r^2 - r l_1 \cos\theta}{l_1^2 - 2 r l_1 \cos\theta + r^2} \tag{6}$$

and

$$\frac{1}{r_{\text{output}}}|\frac{dl_2}{d\theta}| = \frac{r l_1 |\sin\theta|}{r_{\text{output}} \sqrt{l_1^2 - 2 r l_1 \cos\theta + r^2}} \tag{7}$$

where l_1 is the length of $\overline{O_{\text{output}} O_{\text{crk}}}$. Substituting Eqs. (6) and (7) into Eq. (5) yields

$$R_1(\theta, r) = \frac{\omega_{\text{output1}}}{\omega_{\text{crk}}} = \frac{r^2 - r l_1 \cos\theta}{l_1^2 - 2 r l_1 \cos\theta + r^2} + \frac{r l_1 |\sin\theta|}{r_{\text{output}} \sqrt{l_1^2 - 2 r l_1 \cos\theta + r^2}} \tag{8}$$

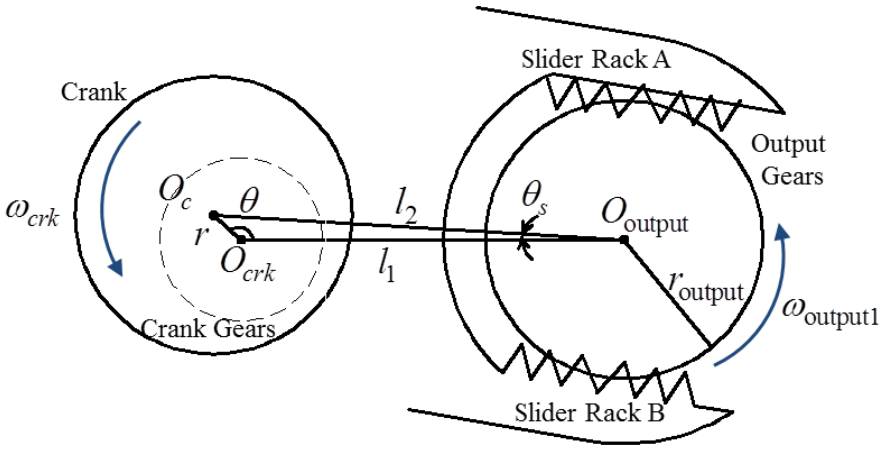

Figure 8: Schematic of the crank-slider motion

There are four crank-slider systems in the motion conversion module. Since the input angle for the four crank-slider systems are evenly distributed, the initial phases of four input angles are 0 deg, 90 deg, 180 deg, and 270 deg, respectively. The eccentricities of the four crank-slider systems are the same. When the eccentricity is constant, the instantaneous speed ratio of one crank-slider system can be calculated from Eq. (8), as shown in Fig. 9(a), and that of the motion conversion module, which is shown in Fig. 9(a), is the maximum value of those of the four crank-slider systems at each angle:

$$R(\theta,r) = \max\{R_1(\theta,r), R_1(\theta+90^o,r), R_1(\theta+180^o,r), R_1(\theta+270^o,r)\} \quad (9)$$

Note that $R(\theta,r)$ is a periodic function of θ with a period of 2π, which is a revolution of crank gears. For a constant eccentricity, the speed ratio of ω_{crk} over the input

speed of the GIVT ω_{in} is $2(r_{\text{sun}}+r_{\text{planet}})/r_{\text{sun}}$; the final speed ratio of the GIVT is

$$F(\theta,r)=\frac{\omega_{\text{out}}}{\omega_{\text{in}}}=\frac{2(\omega_{\text{sun}}+\omega_{\text{planet}})}{\omega_{\text{sun}}}R(\theta,r)=3R(\theta,r) \tag{10}$$

When $\omega_{\text{sun}}=2\omega_{\text{planet}}$, the average of $F(\theta,r)$ over a period of θ is called the average speed ratio of the GIVT for an eccentricity r, which is shown in Fig. 9(b).

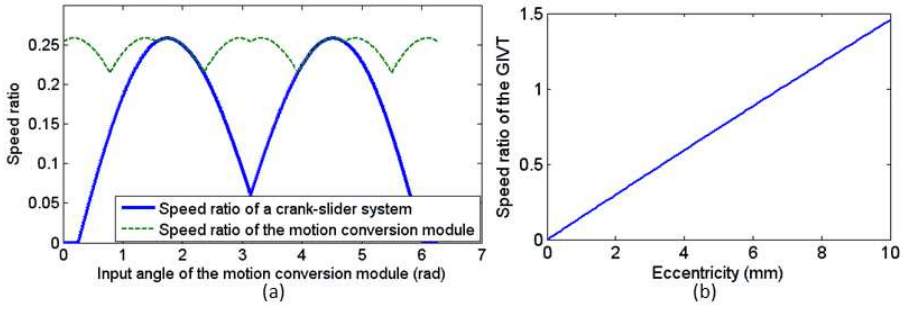

Figure 9: (a) Speed ratios of a crank-slider system and the motion conversion module, and (b) the average speed ratio of the GIVT

2.1.5 Noncircular Gears of the GIVT

There are relatively large variations in the instantaneous speed ratio of the GIVT (around 10% of the average speed ratio), which can introduce a dynamic load, decrease ride comfort for a vehicle application, and increase the failure rate of the transmission. To reduce or eliminate the speed variations, a pair of noncircular gears is used between the input and transmission.

Since average speed ratios for different eccentricities r are different from each other, the reduced speed ratio, which is the instantaneous speed ratio of the motion

conversion module divided by its average value over the period of 2π, is used to design the noncircular gears. By changing r, the shape of the reduced speed ratio is changed, as shown in Fig. 10, and the pair of noncircular gears is designed using the reduced speed ratio for a specific r ($r = 10$ mm), which means that use of the noncircular gears can only eliminate speed variations for the specific eccentricity; instantaneous speed variations for other eccentricities can be reduced from 0 to 2% of the average speed, as shown in Fig. 10.

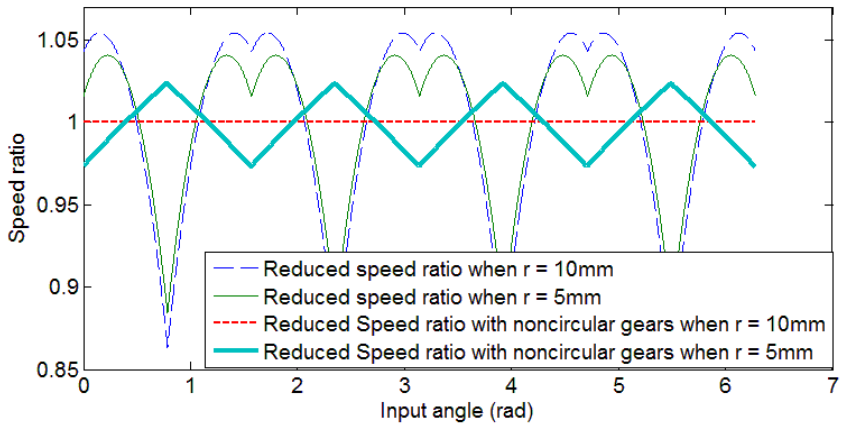

Figure 10: (a) Reduced speed ratios with and without noncircular gears when $r =$ 10 mm and $r = 5$ mm

The noncircular gear connected to the input of the GIVT is denoted by NG1, and that connected to the GIVT is denoted by NG2. Speeds of NG1 and NG2 are denoted by ω_{NG1} and ω_{NG2}, respectively, and rotation angles of NG1 and NG2 are ϕ and $\theta' = \theta/3$, respectively. Note that ω_{NG2} is the input of the GIVT ω_{in}. The

speed ratio of NG1 over NG2 in terms of θ' is

$$R_n(\theta') = \frac{\omega_{\mathrm{NG1}}(\phi)}{\omega_{\mathrm{NG2}}(\theta')} \tag{11}$$

Combining Eqs. (10) and (11) yields the final output-to-input speed ratio of the GIVT:

$$\frac{\omega_{\mathrm{out}}}{\omega_{\mathrm{NG1}}} = \frac{3R(\theta, r_o)}{R_n(\theta')} \tag{12}$$

The desired speed ratio of the noncircular gears is the average of $R(\theta, r_o)$ with respect to θ, where r_o is the desired eccentricity, and $R_n(\theta')$ can be expressed by

$$R_n(\theta') = 3R_r(\theta, r_o) \tag{13}$$

where $R_r(\theta, r_o)$ is the reduced speed ratio when the eccentricity is r_o. The radii of NG1 and NG2 are denoted by $r_{\mathrm{NG1}}(\phi)$ and $r_{\mathrm{NG2}}(\theta')$, respectively, and the distance between the centers of NG1 and NG2 is denoted by D; one has

$$R_n(\theta') = \frac{r_{\mathrm{NG2}}(\theta')}{r_{\mathrm{NG1}}(\phi)} \tag{14}$$

and

$$D = r_{\mathrm{NG1}}(\phi) + r_{\mathrm{NG2}}(\theta') \tag{15}$$

Combining Eqs. (14) and (15) yields

$$r_{\mathrm{NG2}}(\theta') = \frac{R_n(\theta')}{R_n(\theta') + 1} D \tag{16}$$

By Eq. (14), one has

$$d\phi = R_n(\theta')d\theta' \tag{17}$$

The pitch radii of NG1 and NG2 can be calculated from Eqs. (13), (15), and (16), and their profiles for D=10 mm are shown in Fig. 11.

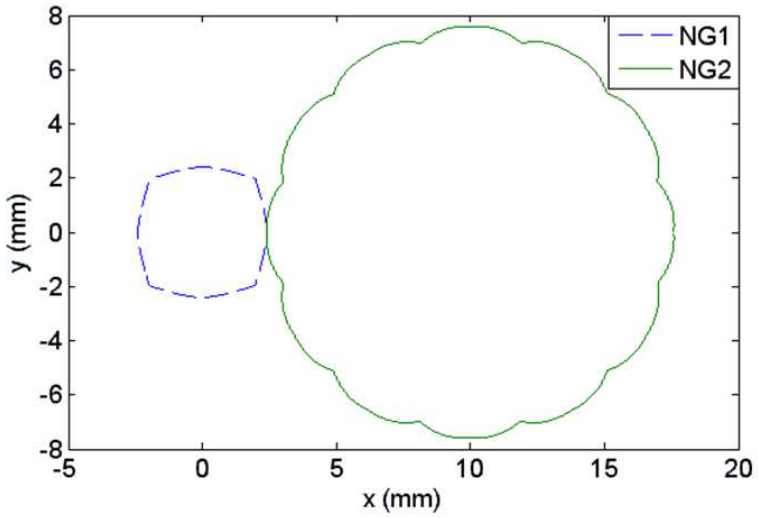

Figure 11: Pitch profiles of NG1 and NG2 with D=10 mm

2.1.6 Direction Control Module of the GIVT

In vehicle applications, the forward or the reverse direction of the vehicle is related to the output direction of the transmission. To change the output direction of the GIVT, a gear set, called the direction control module, is installed after the output of the GIVT. The direction control module consists of two planetary gear sets denoted by PG1 and PG2, as shown in Fig. 12. The input of the direction control module is a ring gear in PG2, called ring gear 2, which is driven by the output shaft of the

GIVT with a speed $\omega_{\text{rg2}} = \omega_{\text{out}}$. The output of the direction control is a carrier in PG1, called carrier 1, whose speed is denoted by ω_{carrier1}. Sun gears of PG1 and PG2 are fixed to the same shaft, and radii of the two sun gears are the same, which are denoted by r_{sunDIR}. The speed of sun gears is denoted by ω_{sunDIR}. Radii of planet gears in PG1 and PG2 are also the same, which are denoted by $r_{\text{planetDIR}}$. The carrier in PG2, called carrier 2, is fixed to the ring gear in PG1, called ring gear 1, and the speeds of carrier 2 and ring gear 1 are the same, which are denoted by ω_{rg1}. The speed relations for PG1 and PG2 are

$$\omega_{\text{sunDIR}} r_{\text{sunDIR}} + \omega_{\text{rg1}} (r_{\text{sunDIR}} + 2r_{\text{planetDIR}}) = 2\omega_{\text{carrier1}} (r_{\text{sunDIR}} + r_{\text{planetDIR}}) \quad (18)$$

and

$$\omega_{\text{sunDIR}} r_{\text{sunDIR}} + \omega_{\text{rg2}} (r_{\text{sunDIR}} + 2r_{\text{planetDIR}}) = 2\omega_{\text{rg1}} (r_{\text{sunDIR}} + r_{\text{planetDIR}}) \quad (19)$$

The forward mode is achieved when ring gear 1 and carrier 2 are grounded, i.e., $\omega_{\text{rg1}} = 0$. Combining Eqs. (18) and (19) yields

$$\omega_{\text{carrier1}} = \frac{-(r_{\text{sunDIR}} + 2r_{\text{planetDIR}})}{4(r_{\text{sunDIR}} + r_{\text{planetDIR}})} \omega_{\text{rg2}}$$

The reverse mode is achieved when sun gears are grounded, i.e., $\omega_{\text{sunDIR}} = 0$. Combining Eqs. (18) and (19) yields

$$\omega_{\text{carrier1}} = \frac{-(r_{\text{sunDIR}} + 2r_{\text{planetDIR}})^2}{4(r_{\text{sunDIR}} + r_{\text{planetDIR}})^2} \omega_{\text{rg2}}$$

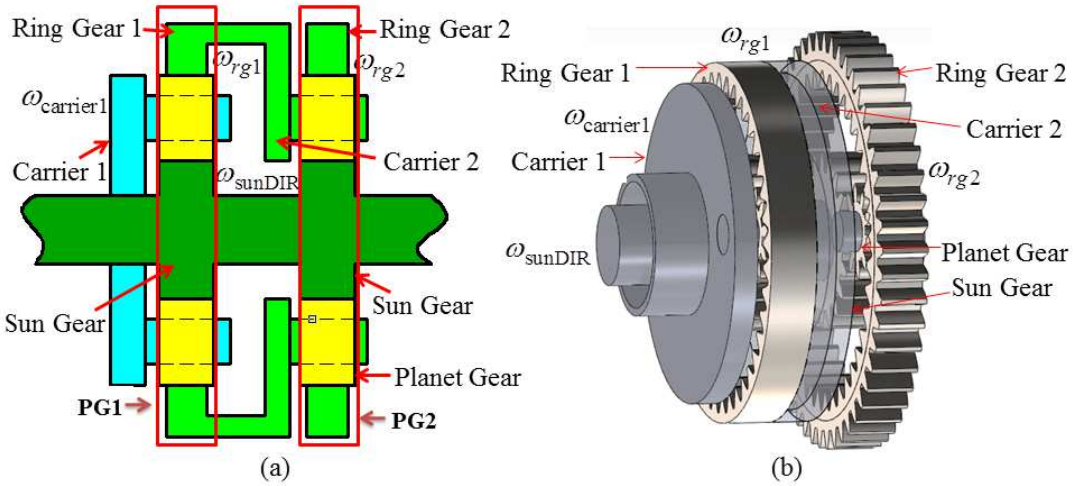

Figure 12: (a) Schematic of the direction control, and (b) the 3D model of the direction control

2.2 Scotch-Yoke Based Geared IVT (SGIVT)

In the design of the GIVT, a pair of noncircular gears are used to reduce the variation in the instantaneous speed ratio. However, from the analysis results in Fig. 10, the variation can be completely eliminated only for a specific average speed ratio. For other average speed ratios, there always are variations due to changes of shapes of intantaneous speed ratios, i.e., changes of reduced speed ratios, for different eccentricities, which can still introduce high frequency vibrations in systems. To completely eliminate variations for all average speed ratios, a scotch-yoke based geared IVT (SGIVT) is developed and illustrated in this section. As well, planetary gear sets in the SGIVT are changed so that the average speed ratio of the pair of noncircular gears can be 1:1, which makes the design of the noncircular gears easier

and their manufacturing more accurate.

2.2.1 Principle, Layout and Overview of the SGIVT

The basic principle of the SGIVT is to convert the input rotational speed of a crank to a translational speed of a yoke in a scotch yoke system, and the translational speed is converted to an output rotational speed of an output gear by a rack-pinion meshing, as shown in Fig. 13. A pin on the end of the crank is inserted in a slot that is fixed to a yoke. When the crank rotates as an input speed of the scotch yoke system, the pin rotates around the center of the crank and slides in the slot, and the slot, as well as the yoke, are driven by the pin to horizontally translate as an output speed of the system. The translation of the yoke is transmitted to the output gear by the rack-pinion meshing and the output gear is rotated. If the crank length is changed, the range of the movement of the yoke is changed, and the amplitude of the output rotational speed is changed. Consequently, the output-to-input speed ratio is changed with the crank length. The motion conversion from the yoke to the output shaft is similar to that in the GIVT. The difference of principles between the GIVT and SGIVT is shown in Fig. 14.

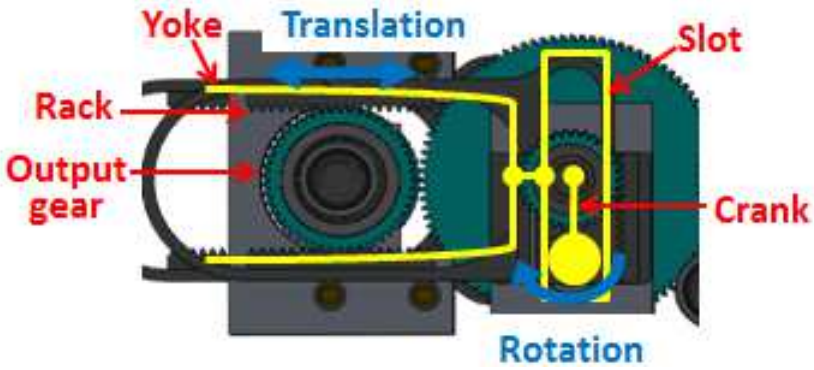

Figure 13: Schematic illustrating the principle of the SGIVT with scotch yoke systems

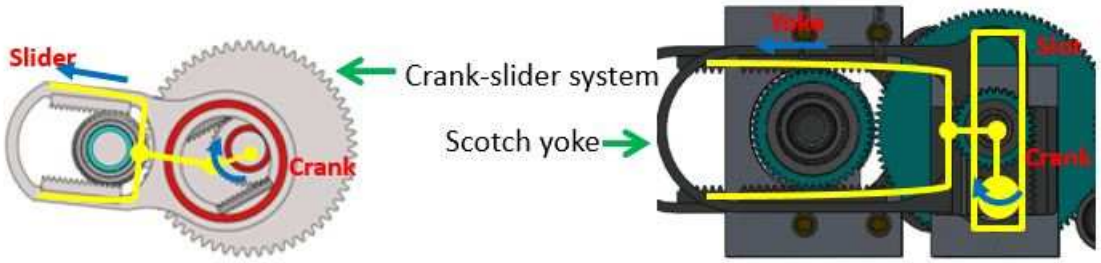

Figure 14: Difference between the GIVT and SGIVT

The structure of the SGIVT is similar to that of the GIVT. However, the detailed design in the SGIVT is different, and it is systematically described here for self-consistency. The SGIVT consists of a pair of meshed noncircular gears and two modules: an input-control module and a motion conversion module, as shown in Fig. 15. In the pair of noncircular gears, the driving noncircular gear is splined on a shaft that is connected to a prime mover, such as an engine, and the corresponding

shaft is called the engine shaft; the driven noncircular gear is splined on the input shaft of the input-control module, which is called the input shaft, and its speed is the input speed of the input-control module. There are two planetary gear sets in the input-control module, shown as the first and second planetary gear sets installed on the input shaft in Fig. 15, and two gears on a control shaft and an idler shaft. Speeds of the control shaft and the idler shaft are controlled by an actuator, such as a stepper motor. Combinations of the input speed with speeds of the control shaft and the idler shaft are the output to the motion conversion module through the first and second planetary gear sets, respectively. There are two scotch yoke systems, a transmitting shaft, and an output shaft in the motion conversion module. Output speeds of the first and second planetary gear sets are input speeds of the first scotch yoke system. The output speed of the second planetary gear set is directly transmitted to the second scotch yoke system, but that of the first planetary gear set cannot be directly transmitted. The transmitting shaft is used to transmit the output speed of the first planetary gear set to the second scotch yoke system, and this transmitted speed and the speed directly from the second planetary gear set are input speeds of the second scotch yoke system. Through the two scotch yoke systems, the input speeds are converted to translational speeds of the yokes, which are converted to rotational speeds of four output gears (two for each scotch yoke system) on the output shaft through four rack-pinion meshings (one for each output gear). The speeds of four output gears are rectified by one-way bearings and transmitted to the output shaft as the output speed of the SGIVT. A schematic diagram of the SGIVT is shown in Fig. 16, and details are illustrated in what follows.

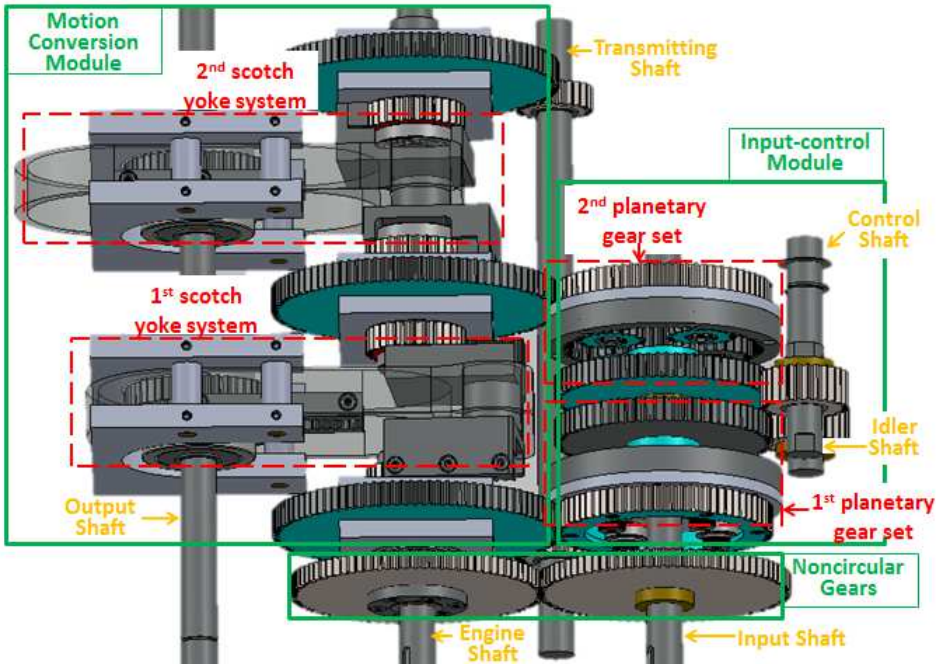

Figure 15: Layout of the SGIVT

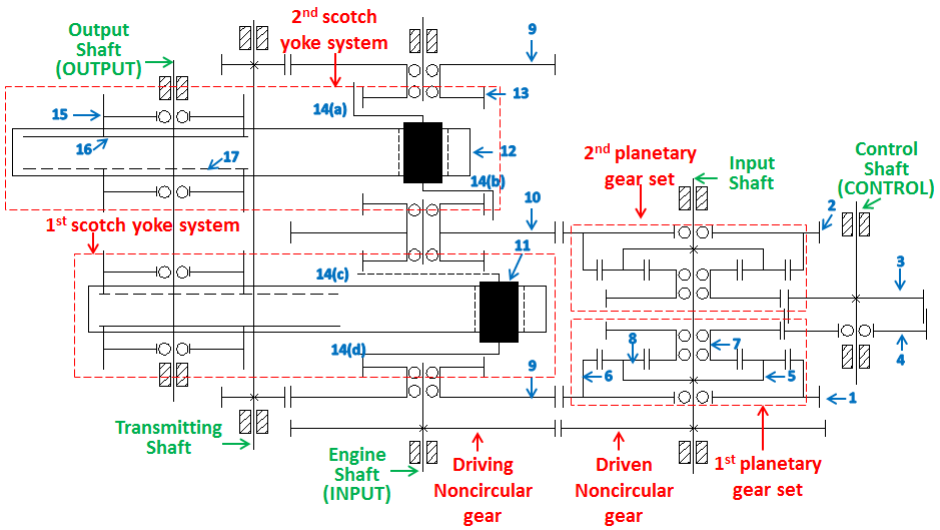

Figure 16: Schematic diagram of the SGIVT. 1- output gear of the first planetary gear set, 2- output gear of the second planetary gear set, 3- gear on the control shaft, 4- gear on the idler shaft, 5- carrier, 6- ring gear, 7- sun gear, 8- planet gear, 9- input gears of scotch yoke systems driven by the first planetary gear set, 10- input gear of scotch yoke systems driven by the second planetary gear set, 11- pin, 12- yoke, 13- crank gear, 14(a-d)- racks meshed with crank gears in four directions, 15- output gear, 16- rack meshed with the output gear on the top side of the yoke represented by a solid line, 17- rack meshed with the output gear on the bottom side of the yoke represented by a dashed line.

2.2.2 Input-control Module of the SGIVT

The major part of the input-control module consists of two identical planetary gear sets that are installed on the input shaft. Besides, there are an active control gear (ACG) on the control shaft and an idler control gear (ICG) on the idler shaft, as shown in Fig. 17. Two planetary gear sets have the same structure, and the structure of the second planetary gear set is illustrated in Fig. 18. The second planetary gear set consists of a sun gear (SG2) with an attached extended sun gear (eSG2), a

ring gear (RG2) with an attached extended ring gear (eRG2), and four planet gears (PGs) that are installed on a carrier (Carrier2). The first planetary gear set has the same structure and dimensions as the second planetary gear set; the number of its denotations is changed from 2 for the second planetary gear set to 1.

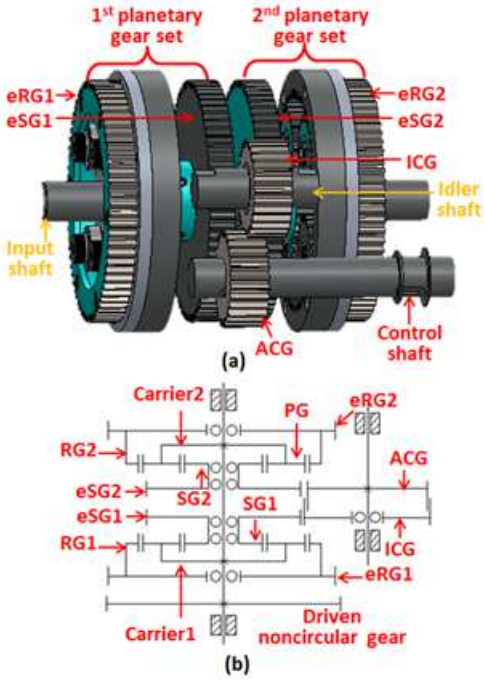

Figure 17: (a) 3D model and (b) schematic diagram of the input-control module

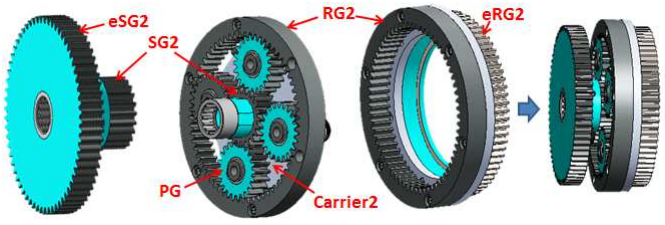

Figure 18: Structure of the second planetary gear set; the first planetary gear set has the same structure

For each planetary gear set, there are two input speeds and an output speed. Carrier1 and Carrier2 are splined on the input shaft, and their speeds are the same as that of the input shaft denoted by ω_{in}, which is one of the two input speeds of each planetary gear set. The second input speeds of the first and second planetary gear sets come from control gears ACG and ICG, respectively. Half of ACG is meshed with half of ICG; the other halves of ACG and ICG are meshed with eSG1 and eSG2 of the first and second planetary gear sets, respectively, as shown in Fig. 17. ACG is directly driven by an actuator, and its speed is called the original control speed denoted by ω_{ACG}. ICG is meshed with and driven by ACG; its speed is opposite to the original control speed and called the idler control speed, which is denoted by ω_{ICG}. Pitch diameters of ACG and ICG are the same, which is 1.75" in the prototype, and the two control speeds have the same value but opposite directions, i.e., $\omega_{\text{ACG}} = -\omega_{\text{ICG}}$. Pitch diameters of eSG1 and eSG2 are 4.5", and speeds of eSG1 and eSG2 are $\omega_{\text{SG1}} = -7\omega_{\text{ACG}}/18$ and $\omega_{\text{SG2}} = -7\omega_{\text{ICG}}/18$, which are the second input speeds of the first and second planetary gear sets, respectively. Speeds of RG1 and RG2 are denoted by ω_{RG1} and ω_{RG2}, which are the output speeds of the first and second planetary gear sets, respectively. Speed relations of the first and second planetary gear sets are

$$\omega_{\text{RG1}} = \frac{2(d_{\text{SG1}} + d_{\text{PG}})\omega_{\text{in}} - d_{\text{SG1}}\omega_{\text{SG1}}}{d_{\text{SG1}} + 2d_{\text{PG}}} \tag{20}$$

and

$$\omega_{\text{RG2}} = \frac{2(d_{\text{SG2}} + d_{\text{PG}})\omega_{\text{in}} - d_{\text{SG2}}\omega_{\text{SG2}}}{d_{\text{SG2}} + 2d_{\text{PG}}} \tag{21}$$

respectively, where $d_{SG1} = d_{SG2} = 1.375$" are pitch diameters of SG1 and SG2, and $d_{PG} = 1.375$" is the pitch diameter of the planet gears. Output speeds of the first and second planetary gear sets are transmitted to the motion conversion module as its input speeds.

2.2.3 Motion Conversion Module in the SGIVT

The motion conversion module consists of the first and second scotch yoke systems, as shown in Fig. 19(a). For each scotch yoke system, there are two motion conversion parts: the first one is an input motion conversion part whose schematic diagram is shown in Fig. 19(b) and the second one is an output motion conversion part. The input motion conversion part is introduced first. Since the two scotch yoke systems are identical, only the structure of the first scotch yoke system is illustrated in Fig. 20. In the first scotch yoke system, there is a yoke (Yoke1), a crank with two pieces connected by a pin, and two crank gears. There is a slot on one end of Yoke1, in which the pin of the crank is inserted. The pin can freely rotate and slide inside the slot. On each piece of the crank, there is a rack attached on it, as highlighted in Fig. 20. The rack on the left piece of the crank is meshed with a crank gear CG1, and that on the right piece of the crank is meshed with another crank gear CG2. Two crank gears, CG1 and CG2, are attached to two extended crank gears, eCG1 and eCG2, respectively. As inputs of the motion conversion module, eCG1 and eCG2 are meshed with extended ring gears (eRG1and eRG2) of the first and second planetary gear sets, respectively. Hence, eRG1 and eRG2 drive eCG1 and eCG2, as well as CG1 and CG2, which rotate around the center O_{CG} of CG1 and CG2, respectively. Pitch diameters of eRG1 and eRG2 are 4.5" and those of eCG1

and eCG2 are 6". Hence, speeds of CG1 and CG2 are $\omega_{CG1} = -3\omega_{RG1}/4$ and $\omega_{CG2} = -3\omega_{RG2}/4$, respectively. All dimensions in the second scotch yoke system are the same as those in the first scotch yoke system, but the positions of CG1 and CG2 are switched. In the second scotch yoke system, CG2 is meshed with the rack on the left piece of the crank, and attached on the other side of eCG2; CG1 is meshed with the rack on the right piece of the crank, and attached on an extended crank gear eCG3. Since eRG1 is not directly meshed with eCG3, speeds of eCG1 and eCG3 are synchronized through meshing with two small gears TG1 and TG2 on a transmitting shaft.

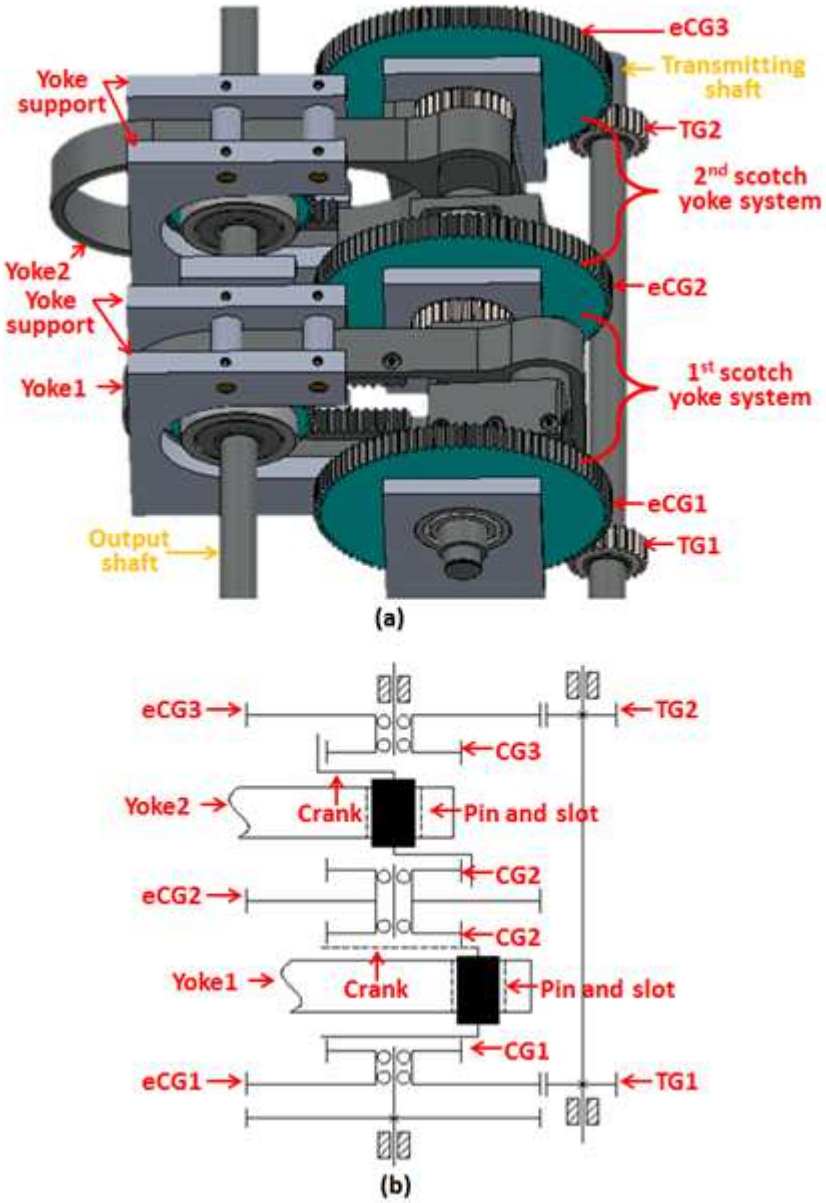

Figure 19: (a) 3D model of the motion conversion module and (b) schematic diagram of the input motion conversion part

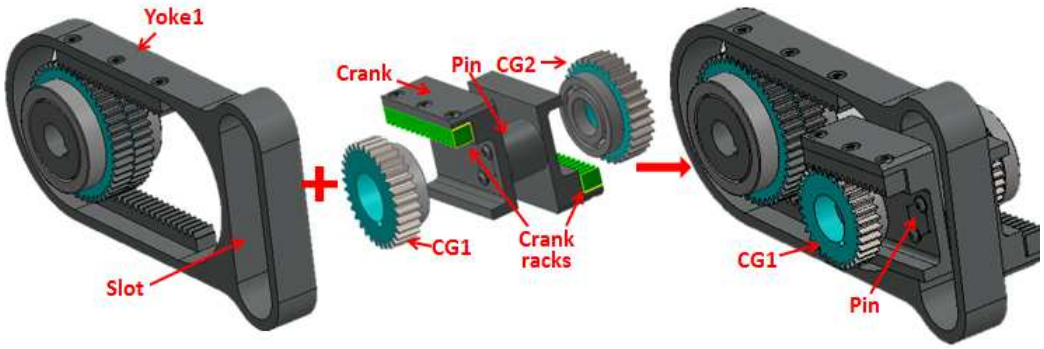

Figure 20: Structure of the first scotch yoke system; the second scotch yoke system has the same structure

In the input motion conversion part of the first scotch yoke system, two speeds ω_{CG1} and ω_{CG2} are combined to be the input speed of the crank. Similar to the GIVT, the motion of the crank in the SGIVT has three modes. First, if the control speeds are zero, i.e., $\omega_{\mathrm{SG1}} = 0$ and $\omega_{\mathrm{SG2}} = 0$, substituting values of ω_{SG1} and ω_{SG2} into Eqs. (20) and (21) yields $\omega_{\mathrm{RG1}} = \omega_{\mathrm{RG2}}$, and consequently $\omega_{\mathrm{CG1}} = \omega_{\mathrm{CG2}}$, and the crank, as well as the center of the pin denoted by O_P, rotate around the center of crank O_{CG} gears at a speed ω_{CG1} or ω_{CG2}. In this mode, the distance between O_P and O_{CG}, which is the crank length, is not changed. Second, if the control speeds are nonzero but the speed of the input shaft is zero, CG1 and CG2 rotate at the same speed but in opposite directions. Consequently, the crank only translates along the direction of the racks, and the crank length is changed. Third, if the control speeds and the speed of the input shaft are nonzero, the motion of the crank is a combination of the above rotation and translation, i.e., O_P rotates around O_{CG} at a speed of

$$\omega_{\mathrm{CRK}} = \frac{\omega_{\mathrm{CG1}} + \omega_{\mathrm{CG2}}}{2} \tag{22}$$

while the crank length is changed at a speed of

$$v_{\mathrm{CRK}} = \frac{\omega_{\mathrm{CG1}} - \omega_{\mathrm{CG2}}}{2} r_{\mathrm{CG}} \tag{23}$$

where $r_{\mathrm{CG}} = 1$" is the radius of the crank gears. The pin of the crank moves in the same way, and it drives the yoke to horizontally move, since the motion of the yoke is constrained in the horizontal direction by a yoke support. When the pin rotates around O_{CG} with a radius equal to the crank length denoted by e, which is an integral of v_{CRK} with respect to time, the pin slides in the slot of the yoke and drives the yoke to translate back and forth, as shown in Fig. 21. The displacement of a yoke is denoted by x; the angle from the right-pointed horizontal direction to the center line of the crank in the clockwise direction is denoted by θ_{CRK}, which is an integral of ω_{CRK} with respect to time. The displacement of the yoke in the first scotch yoke system is

$$x_1 = e\cos\theta_{\mathrm{CRK}} \tag{24}$$

and the speed of the yoke is

$$v_1 = \dot{x}_1 = \dot{e}\cos\theta_{\mathrm{CRK}} - e\omega_{\mathrm{CRK}}\sin\theta_{\mathrm{CRK}} \tag{25}$$

The angle from the right–pointed horizontal direction to the center line of the crank in the second scotch yoke system in the clockwise direction lags 90 deg with respect to that in the first scotch yoke system, as shown in Fig. 21. The displacement and the speed of the yoke in the second scotch yoke system are

$$x_2 = e\cos(\theta_{\mathrm{CRK}} - 90^o) \tag{26}$$

and

$$v_2 = \dot{x}_2 = \dot{e}\cos(\theta_{\mathrm{CRK}} - 90^o) - e\omega_{\mathrm{CRK}}\sin(\theta_{\mathrm{CRK}} - 90^o) \tag{27}$$

Usually, the rate to change the speed ratio in a transmission is much less than its input speed. Thus, control speeds can be assumed as zero, i.e., the crank length is constant, and setting $\dot{e} = 0$ in Eqs. (25) and (27) yields

$$v_1 = -e\omega_{\mathrm{CRK}}\sin\theta_{\mathrm{CRK}} \tag{28}$$

and

$$v_2 = -e\omega_{\mathrm{CRK}}\sin(\theta_{\mathrm{CRK}} - 90^o) \tag{29}$$

respectively.

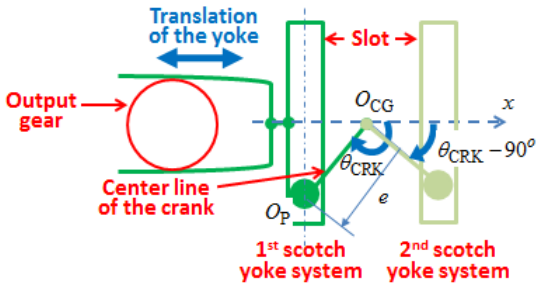

Figure 21: Schematic of the first and second scotch yoke system

In the output motion conversion part of a scotch yoke system, there are two racks fixed on the upper and lower sides of the yoke, as highlighted in Fig. 22. These two racks are placed face-to-face but not in a plane. There are two output gears meshed with the racks. The left output gear is meshed with the upper rack but not the

lower rack, and the right gear is meshed with the lower rack but not the upper rack. When the yoke translates back and forth, the left and right output gears are driven to rotate at the same speed but in opposite directions. If the clockwise direction is defined as the positive direction for output gears, speeds of the left and right output gears in the first scotch yoke system are $\omega_{OG1} = v_1/r_{OG}$ and $\omega_{OG2} = -v_1/r_{OG}$, respectively, and those of the left and right output gears in the second scotch yoke system are $\omega_{OG3} = v_2/r_{OG}$ and $\omega_{OG4} = -v_2/r_{OG}$, respectively, where $r_{OG} = 1.5$" is the radius of the output gears. Substituting Eqs. (28) and (29) into the expressions for the speeds of the output gears yields

$$\omega_{OG1} = \frac{e}{r_{OG}}\omega_{CRK}\sin(\theta_{CRK} - 180^o)$$

$$\omega_{OG2} = \frac{e}{r_{OG}}\omega_{CRK}\sin\theta_{CRK}$$

$$\omega_{OG3} = \frac{e}{r_{OG}}\omega_{CRK}\sin(\theta_{CRK} - 270^o)$$

$$\omega_{OG4} = \frac{e}{r_{OG}}\omega_{CRK}\sin(\theta_{CRK} - 90^o)$$

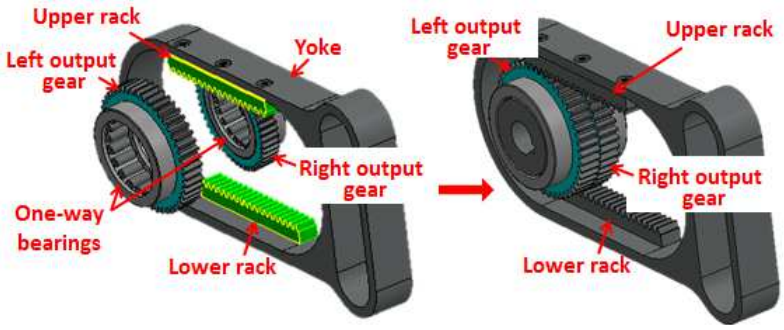

Figure 22: Structure of the output motion conversion part of a scotch yoke system

Each output gear is installed on the output shaft by a one-way bearing. One-way bearings allow output gears to freely rotate in the counterclockwise direction. Hence, when the output gears rotate more slowly than the output shaft in the clockwise direction, the output gears are disengaged from the rotation of the output shaft; when an output gear tends to rotate faster than the output shaft in the clockwise direction, the output gear is engaged to the rotation of the output shaft, and the output shaft rotates at the speed of the output gear. Consequently, the speed of the output shaft is the maximum speed of the four output gears:

$$\omega_{\text{out}} = \max\{\omega_{\text{OG1}}, \omega_{\text{OG2}}, \omega_{\text{OG3}}, \omega_{\text{OG4}}\} \tag{30}$$

Given $d_{\text{SG1}} = d_{\text{SG2}} = d_{\text{PG}}$ and $\omega_{\text{SG1}} = -\omega_{\text{SG2}}$, substituting them into Eqs. (20) and (21) yields

$$\omega_{\text{RG1}} = \frac{4}{3}\omega_{\text{in}} - \frac{1}{3}\omega_{\text{SG1}} \tag{31}$$

$$\omega_{\text{RG2}} = \frac{4}{3}\omega_{\text{in}} + \frac{1}{3}\omega_{\text{SG1}} \tag{32}$$

Substituting Eqs. (31) and (32) into Eq. (22) and using the relations $\omega_{\text{CG1}} = -3/4\omega_{\text{RG1}}$ and $\omega_{\text{CG2}} = -3/4\omega_{\text{RG2}}$ yield

$$\omega_{\text{CRK}} = \omega_{\text{in}} \tag{33}$$

Integrating two sides of the above equation with respect to time with the same initial condition yields

$$\theta_{\text{CRK}} = \theta_{\text{in}} \tag{34}$$

where θ_{in} is the angle of the input shaft. Substituting Eqs. (33) and (34) into Eq. (30) and dividing two sides of the resultant equation by ω_{in} yield

$$R = \frac{\omega_{\text{out}}}{\omega_{\text{in}}} = \frac{e}{r_{\text{OG}}} \max\{\sin(\theta_{\text{in}}), \sin(\theta_{\text{in}} - 90^o), \sin(\theta_{\text{in}} - 180^o), \sin(\theta_{\text{in}} - 270^o)\} \tag{35}$$

which is the expression for the output-to-input speed ratio of the SGIVT without noncircular gears. When e is a constant, the speed ratio changes periodically with θ_{CRK} and has a shape of sinusoidal-like wave. Changing of e does not change the shape of the speed ratio. To eliminate periodic variations in the speed ratio, a pair of noncircular gears is designed and installed on the engine and input shafts, as shown in Fig. 15.

2.2.4 Noncircular Gears in the SGIVT

The output-to-input speed ratio is used to design pitch profiles of a pair of noncircular gears. The driving noncircular gear on the engine shaft is denoted by NG1, and the driven noncircular gear on the input shaft is denoted by NG2. The angle and the speed of NG2 are the same as those of the input shaft in the input-control module. Assume the speed ratio between NG1 and NG2 is

$$R_n(\theta_{\text{in}}) = \frac{\omega_{\text{eng}}(\theta_{\text{eng}})}{\omega_{\text{in}}(\theta_{\text{in}})} = \frac{d\theta_{\text{eng}}}{d\theta_{\text{in}}} \tag{36}$$

where θ_{eng} is the angle of NG1, and ω_{eng} is the speed of NG1 at θ_{eng}. Theoretically, it is expected that the speed ratio between the output shaft and NG1

$$\frac{\omega_{\text{out}}(\theta_{\text{in}})}{\omega_{\text{eng}}(\theta_{\text{eng}})} = \frac{\omega_{\text{out}}(\theta_{\text{in}})}{\omega_{\text{in}}(\theta_{\text{in}})} \frac{\omega_{\text{in}}(\theta_{\text{in}})}{\omega_{\text{eng}}(\theta_{\text{eng}})} = \frac{R}{R_n} \tag{37}$$

is a constant. An acceptable expression for R_n is

$$R_n(\theta_{\text{in}}) = \frac{\pi}{2\sqrt{2}} \max\{\sin(\theta_{\text{in}}), \sin(\theta_{\text{in}} - 90^o), \sin(\theta_{\text{in}} - 180^o), \sin(\theta_{\text{in}} - 270^o)\} \tag{38}$$

for which the average speed ratio between NG1 and NG2 is 1:1, i.e., when NG1 rotates one revolution, NG2 also rotates one revolution. The 1:1 speed ratio provides a benefit to design pitch profiles of a pair of meshed noncircular gears, which makes the transmission more compact and the stress distribution on teeth of noncircular gears more uniform.

Profiles of the noncircular gears are derived in the following. The distance between the centers of NG1 and NG2 is

$$D = r_{\text{NG1}}(\theta_{\text{eng}}) + r_{\text{NG2}}(\theta_{\text{in}}) = 5.25\text{”} \tag{39}$$

where $r_{\text{NG1}}(\theta_{\text{eng}})$ and $r_{\text{NG2}}(\theta_{\text{in}})$ are radii of NG1 and NG2 at θ_{eng} and θ_{in}, respectively. Another relation between $r_{\text{NG1}}(\theta_{\text{eng}})$ and $r_{\text{NG2}}(\theta_{\text{in}})$ is derived from Eq. (36):

$$R_n(\theta_{\text{in}}) = \frac{\omega_{\text{eng}}(\theta_{\text{eng}})}{\omega_{\text{in}}(\theta_{\text{in}})} = \frac{r_{\text{NG2}}(\theta_{\text{in}})}{r_{\text{NG1}}(\theta_{\text{eng}})} \tag{40}$$

The differential relation between θ_{eng} and θ_{in} is obtained from Eq. (36):

$$d\theta_{\text{eng}} = R_n(\theta_{\text{in}}) d\theta_{\text{in}} \tag{41}$$

Theoretical pitch profiles of NG1 and NG2 can be generated from Eqs. (39) through (41), as shown in Fig. 23(a). There are sharp corners in the profiles, which cannot

be manufactured in practice. The sharp corners are caused by discontinuities of the first derivative of the expression in Eq. (38) with respect to θ_{in}. Hence, a fitted smooth function using a series of cosine functions can replace the theoretical speed ratio in Eq. (38):

$$R_{smooth} = 1 + 0.12\cos(4\theta_{in}) - 0.0286\cos(8\theta_{in}) + 0.0126\cos(12\theta_{in}) - 0.007\cos(16\theta_{in}) \quad (42)$$

Special tooth profiles for the speed ratio in the above equation can be generated by using a virtual rack cutter that is rolling along pitch profiles of the noncircular gears without sliding [45]. A complex mathematical calculation is required for generation of the tooth profiles, and there is no standard tolerance available for manufacturing of the nonstandard profiles. An alternative way to easily generate tooth profiles is to use approximated pitch profiles, which are segments of tangent circular arcs that replace the noncircular pitch profiles, as shown in Fig. 23(b), and standard tooth profiles of circular gears can be directly applied for the arcs. There are two requirements to select the arcs: 1) first derivatives of two adjacent arcs with respect to θ_{in} should be continuous at the connecting point, and 2) the maximum deviation of the approximated pitch profiles from the theoretical ones is less than 1% of the theoretical ones. There is an exception at a sharp corner. Every sharp corner of an approximated pitch profile is rounded with an arc to allow for a gear tooth or a gear space (the space between two teeth). Hence, the deviation at a sharp corner cannot be guaranteed to be within 1%, and it is within 5% for the current noncircular gears. Based on the approximated pitch profiles, the tooth profiles are generated and shown in Fig. 23(c). The speed ratios with the noncircular gears generated by

the exact and approximated functions are shown in Fig. 24. The speed ratio with use of the exact function has no speed variations, and the speed ratio with use of the approximated function has small speed variations that can be predicted to occur in practice.

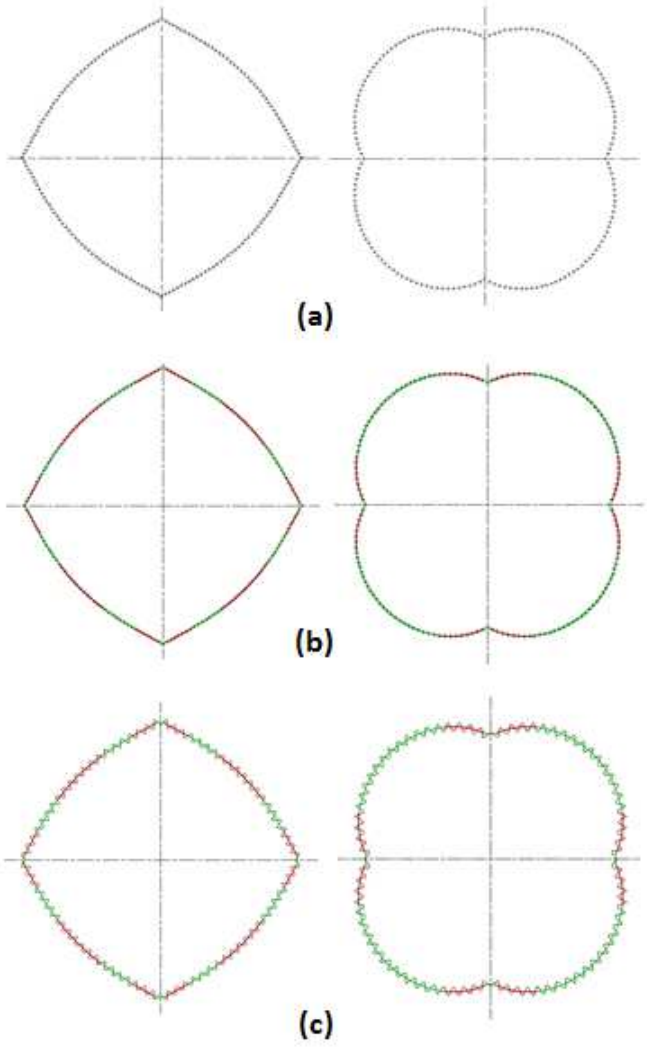

Figure 23: (a) Theoretical pitch profiles, (b) approximated pitch profiles with segments of circular arcs, and (c) tooth profiles based on the approximated pitch profiles in (b).

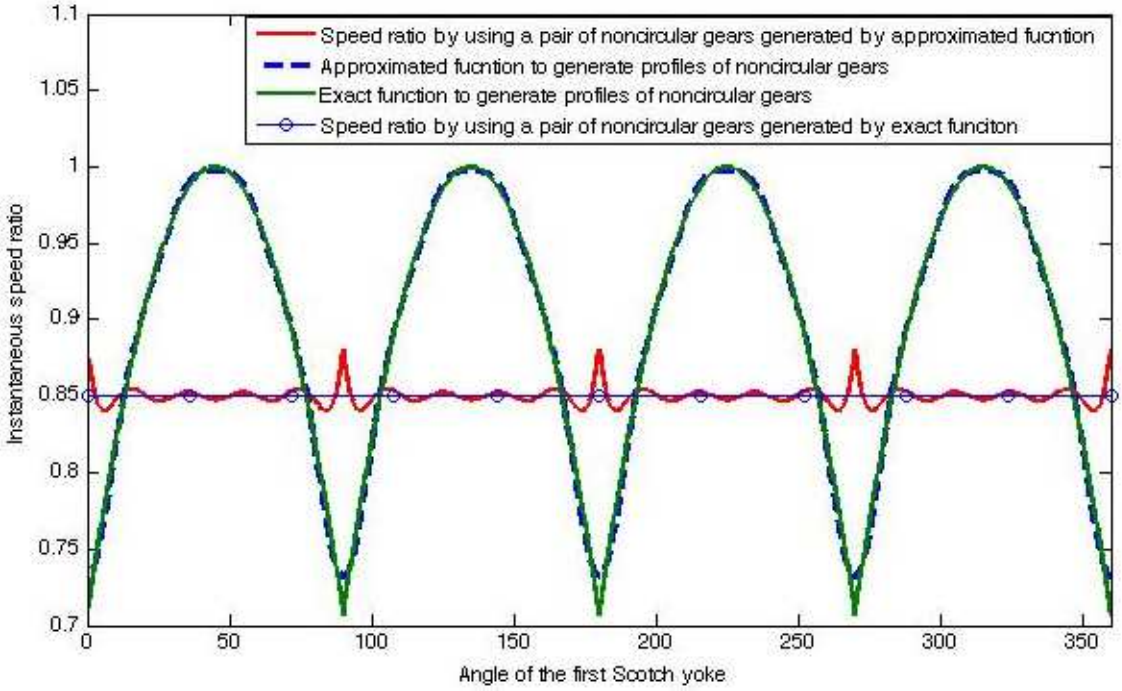

Figure 24: Speed ratios with the noncircular gears generated by the exact and approximated functions

2.3 Modifications for the SGIVT

In the testing of the prototype of the SGIVT introduced in Sec. 2.2, some problems affect the efficiency and performance of the transmission. In order to achieve zero speed ratio, i.e., drivers do not move when the input speed is nonzero, the pin in the middle of the crank should be concentric with the shaft where the crank gears are installed. Thus, the shaft is divided into three segments so that two pins can travel between them. However, the segmentation introduces some problems. First,

there are more parts required in the transmission, which make it less compact. Second, it is much more difficult to control dimension tolerance of all segments of the shaft than that of an entire shaft, as well as their postion tolerance, especially the concentricity of all segments. Once there is large error in concentricity, travelling lengths of racks on two sides of a crank cannot be accurately controlled, and the pin in the middle of the crank could have a large misalignment to the slot of a driver. Consequently, there could be large friction when the pin slides in the slot, which significantly reduces the efficiency and affects the performance of the system. Third, each segment of the shaft can be considered as a cantilever beam in load, which has lower strength and resonant frequency than supported beam. To solve these problems, a variantion of the SGIVT is developed by modifying its motion-conversion module. In the variation, small pins in the SGIVT are replaced by large rollers so that they can be installed on an entire shaft, as shown in Fig. 25.

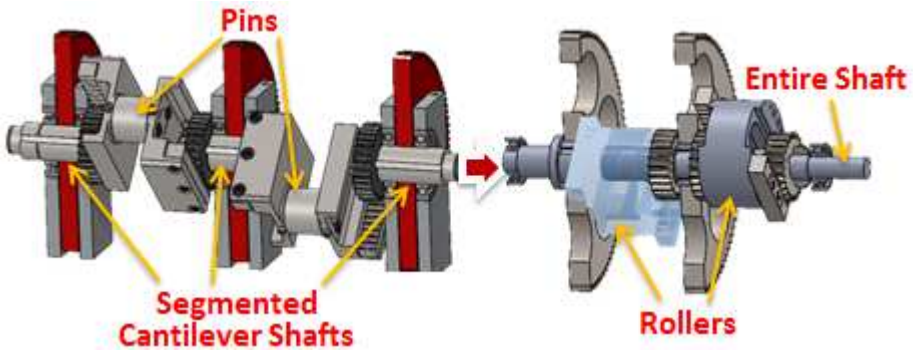

Figure 25: Modification of the variant of the SGIVT with small pins replaced by large rollers

The variation of the SGIVT has the same structure but different layout with the SGIVT, which consists of a pair of noncircular gears, an input-control module and

a motion conversion module, as shown in Fig. 26; the input-control module and motion-conversion module constitute the main body of the IVT. An input speed from a prime mover, such as an engine or a motor, is modulated through the pair of noncircular gears and transmitted to the main body of the IVT. The modulated input speed is combined with a control speed in the input-control module, and the combination of the modulated input and control speeds, which is called the combined speed, is transmitted to the motion-conversion module. In the motion-conversion module, the combined speed is converted to a translational speed and is then converted back to a rotational output speed, where the speed ratio is changed in these two conversions.

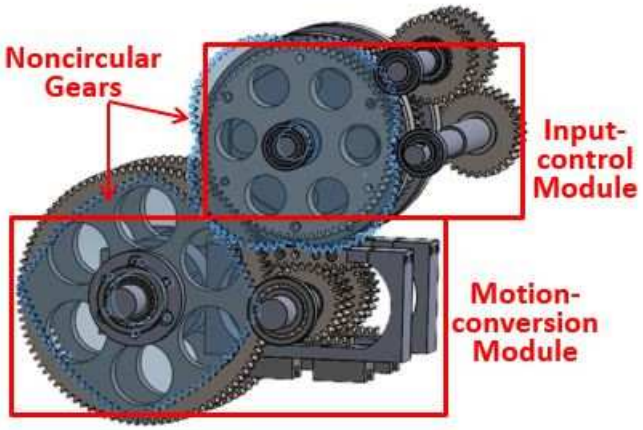

Figure 26: Layout of a variant of the SGIVT; two highlighted transparent gears are noncircular gears, parts on three shafts in the top layer constitute the input-control module, and parts on two shafts in the bottom layer constitute the motion-conversion module.

Kinematics of the variation of the SGIVT will be briefly described here, even though it is very similar to that of the SGIVT, since kinematic equations are needed

in the development of a dynamic model of the variation in the sequel. A schematic of the variant of the SGIVT is shown in Fig. 27 to illustrate its principle. The input angular speed ω_m from a prime mover is transmitted to the IVT through the pair of noncircular gears, whose speed ratio that varies with the angle θ of the driven noncircular gear is

$$\frac{\omega_m}{\omega} = f(\theta) = \frac{\pi}{2\sqrt{2}} \max\{|\sin\theta|, |\cos\theta|\} \tag{43}$$

where $\max\{\cdot,\cdot\}$ is a function that gives the maximum value of two arguments, $\omega = \dot{\theta}$ is the modulated input speed on the driven noncircular gear, and the average of $f(\theta)$ over a period of 2π in θ is unit. The modulated input speed ω is transmitted to carriers of two planetary gear sets in the input-control module, and angular speeds of two sun gears, denoted by $\pm\omega_c$, have the same value and opposite direction, which are generated by a control actuator. Angular speeds of two ring gears, denoted by ω_{ri} with $i = 1, 2$, are combinations of ω and ω_c:

$$\omega_{ri} = \frac{2(d_S + d_P)\omega \pm d_S\omega_c}{d_S + 2d_P} \tag{44}$$

where d_s and d_p are diameters of sun gears and planet gears, respectively, and they are transmitted to two sets of crank gears in the motion-conversion module. When the control actuator holds at a fixed position, i.e. $\omega_c = 0$, ω_{r1} is equal to ω_{r2}, and angular speeds of crank gears are equal to ω by choosing a proper gear ratio between ring gears and crank gears. Two rollers, whose centers are offset from the center of crank gears with an eccentricity r, rotate around the center of crank gears at the same speed ω as those of crank gears. The angle between directions of

eccentricities of the two rollers is 90^o, as shown in the motion-conversion module in Fig. 27 by two perpendicular arrows. The block in the motion-conversion module in Fig. 27, which contacts with a roller, is called the driver, and there are two drivers corresponding to the two rollers. Eccentric rotations of the two rollers are converted to translational motions of two drivers through the contact force, and the translational speeds are

$$v_{d1} = \omega r \sin\theta \tag{45}$$

$$v_{d2} = \omega r \cos\theta \tag{46}$$

There are two output gears meshing with an upper and a lower rack on each driver, and angular speeds of the two output gears are $\pm v_{di}/r_u$ with $i = 1,2$, where r_u is the radius of the output gears. Speeds of four output gears are rectified by one-way bearings so that they transmit speeds in the same direction, and the speed of the output shaft is the combination of the four rectified speeds:

$$\omega_U = \max\{|\frac{v_{d1}}{r_u}|, |\frac{v_{d2}}{r_u}|\} = \frac{2\sqrt{2}}{\pi r_u} f\omega r = \frac{2\sqrt{2}}{\pi r_u} r\omega_m \tag{47}$$

which shows that the speed ratio of ω_U and ω_m is constant due to the modulation in Eq. (43) and is controlled by r.

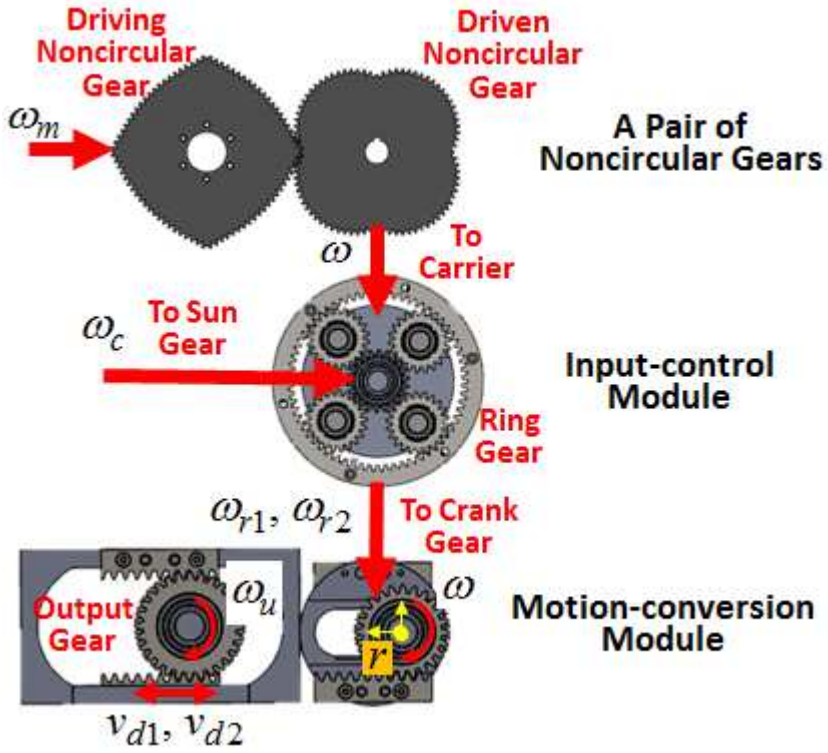

Figure 27: Schematic of the principle of the variant of the IVT; two perpendicular arrows in the motion-conversion module indicate the 90^o phase difference between the two rollers.

3 Modified Incremental Harmonic Balance (IHB) Method

3.1 Introduction to the IHB Method

The dynamic model of the IVT is governed by a nonlinear ordinary differential equation [31, 25]. In analysis of nonlinear problems, perturbation methods [46], such as the multiple scales method and the averaging method, are often used to derive analytical solutions. However, the perturbation methods are feasible and reliable for low-degree-of-freedom systems with weak nonlinearities. In the work of Bajkowski and Szemplinska-Stupnicka [47], internal resonance in a two-degree-of-freedom system was investigated using both the averaging method and a numerical method, and results showed that amplitude-frequency response curves from the two methods become very different when there are strong nonlinearities in the system. To deal with multi-degree-of-freedom systems with strong nonlinearities, the incremental harmonic balance (IHB) method is one of the most amenable approaches: it can provide arbitrarily high accuracy for periodic solutions and is suitable for computer implementation [48]. The IHB method is a combination of Newton's method and Galerkin procedure [49], which was first introduced by Lau and Cheung [50]; Galerkin procedure is essentially a harmonic balance procedure. The IHB method was successfully applied to many periodic vibration problems as well as some aperiodic vibration problems [51].

To automatically and reliably obtain amplitude-frequency response curves, an incremental arc-length method with a cubic extrapolation technique was developed in [52], and an improved arc-length method with a path-following technique was presented in [53]. With the arc-length method, an amplitude-frequency response

curve can successfully trace a sharp peak, and a small number of iterations are required to obtain a convergent solution. Stability of periodic solutions of nonlinear systems was investigated using Lyapunov-Floquet transformation based on Floquet theory [54, 55, 56]. Instability occurs when the transformation matrix has a real eigenvalue that exceeds unity. There is a period doubling bifurcation when the eigenvalue is less than -1. A periodic solution is stable when all eigenvalues are inside a unit circle. An efficient numerical method for approximating the transformation matrix in one period was developed by Hsu and Cheng [57]. Friedmann et al. gave a concise formulation of Hsu's method [58]. The technique based on Floquet theory was used to study stability of steady-state solutions from the IHB method [52, 53], and bifurcations of periodic solutions can be detected and traced [59, 60, 61]. The IHB method can also be used to determine parametric instability boundaries of a parametrically excited system [48, 62].

While the IHB method provides an efficient and reliable way to solve strongly nonlinear problems, to apply Newton's method, much effort is devoted to calculating the Jacobian of nonlinear algebraic equations, which result from Galerkin procedure that is used to balance truncated terms of Fourier series of periodic solutions of nonlinear differential equations. Calculation of the Jacobian can be extremely difficult for a system with a high degree of freedom and complex nonlinearities. If numbers of truncated terms of the Fourier series are large enough, the Fourier coefficients can be approximated by coefficients of a discrete Fourier transform (DFT) that are calculated without using integrals. In practice, the fast Fourier transform (FFT) is used to efficiently calculate coefficients of a DFT [63, 64, 65], which can improve calculation efficiency of the IHB method.

However, complexity of constructing the Jacobian is still significant due to two reasons: first, calculation for obtaining FFT coefficients can be huge when there are large numbers of terms of Fourier series; second, Galerkin procedure and the following procedure to combine similar trigonometric terms are not simplified; they need cumbersome computation and are prone to making mistakes. To overcome the difficulties in constructing the Jacobian, a quasi-Newton method called Broyden's method [66] can be used, in which the true Jacobian is replaced by an approximated Jacobian that is iteratively updated. The method was proved to have Q-quadratic convergence for nonlinear problems [67]. By using Broyden's method, one does not need to construct the complex Jacobian of nonlinear algebraic equations. Instead, the Jacobian of the associated linear algebraic equations is used as the initial guess of an iteration procedure. Construction of the Jacobian of linear algebraic equations is much easier than that of nonlinear algebraic equations, which can be automatically generated with customized mass, damping, and stiffness matrices of the linear algebraic equations.

When the arc-length method with the path-following technique is used to obtain an amplitude-frequency response curve, a complete set of equations is constructed by combining nonlinear algebraic equations with an augmenting equation [53]. Consequently, the Jacobian of the complete set of equations is a combination of the Jacobian of nonlinear algebraic equations and that of the augmenting equation. By using Broyden's method to obtain the approximated Jacobian of the complete set of equations, the approximated Jacobian of the augmenting equation is also updated. However, the Jacobian of the augmenting equation that is updated by Broyden's method should be invariant since its initial guess has exact values.

In the next section, a modified IHB method based on the FFT and Broyden's method for solving ordinary differential equations is presented. The Jacobian is not exactly calculated, but approximated using Broyden's method, and Fourier coefficients of a residual are obtained using the FFT. To start Broyden's method, the Jacobian of the associated linear algebraic equations is used as an initial guess of that of the nonlinear algebraic equations, which is directly generated with the mass, damping, and stiffness matrices, as shown in what follows. To obtain an amplitude–frequency response curve using the modified IHB method, the approximated Jacobian of the complete set of equations is constructed, and the property that the updated Jacobian of the augmenting equation is invariant when the augmenting equation is selected as a linear equation is proved. Duffing's equation is used as an example to demonstrate the procedure of the modified IHB method. Solutions from the modified IHB method and Runge–Kutta method are compared, and stability of solutions is analyzed. The modified IHB method is also successfully used to calculate bifurcations of Mathieu–Duffing equation [68]. While single-degree-of freedom systems are used to illustrate the modified IHB method in this paper, the methodology can be readily extended to multi-degree-of-freedom systems. In the last section, the methodology for ordinary differential equations is also extended to the spatial and temporal harmonic balance method for solving partial differential equations.

3.2 Modified IHB Method

3.2.1 IHB Method in Solving Duffing's Equation

A second-order nonlinear differential equation for a single-degree-of-freedom system can be usually represented by

$$f(\ddot{u}, \dot{u}, t, \lambda, F) = 0 \tag{48}$$

where f is a nonlinear function, t and u are independent and dependent variables of the equation, respectively, $\dot{u}$ and $\ddot{u}$ are the first and second derivatives of u with respect to t, respectively, λ is a parameter of the equation, and F is the amplitude of a harmonic excitation. If the nonlinear equation is Duffing's equation, Eq. (48) can be written as

$$\ddot{u} + 2\xi\dot{u} + \alpha u + \varepsilon u^3 - F\cos(\omega_f t) = 0 \tag{49}$$

where ξ is the damping ratio, α is a linear stiffness coefficient, ε is a nonlinear stiffness coefficient, and ω_f is the frequency of the harmonic excitation. The procedure of the IHB method to solve Eq. (49) is shown below:

1. Assigning a dimensionless variable $\tau = \omega t$, where ω is the frequency variable. Replacing t by τ in the first and second derivatives of u with respect to t yields

   $$\dot{u} = \frac{du}{dt} = \omega\frac{du}{d\tau} = \omega u' \tag{50}$$

   and

   $$\ddot{u} = \frac{d^2u}{dt^2} = \omega^2\frac{d^2u}{d\tau^2} = \omega^2 u" \tag{51}$$

respectively.Substituting Eqs. (50) and (51) into Eq. (49) and letting $p = \omega_f/\omega$ yield

$$\omega^2 u" + 2\omega\xi u' + \alpha u + \varepsilon u^3 - F\cos p\tau = 0 \tag{52}$$

When p is an integer, one can calculate period-p solutions of subharmonic responses.

2. Linearizing Eq. (52) around a trial solution $(u_o, u'_o, u"_o, \omega_o)$ yields

$$\omega_o^2 \Delta u" + 2\omega_o\xi\Delta u' + (\alpha + 3\varepsilon u_o^2)\Delta u + f_\omega(u_o)\Delta\omega = -f_o(u_o,\tau) \tag{53}$$

where

$$f_o(u_o,\tau) = \omega_o^2 u"_o + 2\omega_o\xi u'_o + \alpha u_o + \varepsilon u_o^3 - F\cos p\tau$$

is the residual of the linearized equation, $f_\omega(u_o) = 2\omega_o u"_o + 2\xi u'_o$ is the partial derivative of f with respect to ω, and $(\Delta u, \Delta u', \Delta u", \Delta\omega)$ are increments of $(u_o, u'_o, u"_o, \omega_o)$ defined by $\omega = \omega_o + \Delta\omega$ and $u = u_o + \Delta u$.

3. Using truncated Fourier series to represent u and Δu yields

$$u = \mathbf{C}_s^{\mathrm{T}} A$$

and

$$\Delta u = \mathbf{C}_s^{\mathrm{T}} \Delta A$$

where n is the number of truncated cosine and sine terms, a superscript T

denotes a transpose of a matrix or a vector,

$$\mathbf{C}_s = \{\frac{1}{2}\ \cos\tau\ \cdots\ \cos n\tau\ \sin\tau\ \cdots \sin n\tau\}^{\mathrm{T}}$$

is the basis of the truncated Fourier series,

$$A = \{a_0\ a_1\ \cdots\ a_n\ b_1\ \cdots b_n\}^{\mathrm{T}}$$

is the vector of the truncated Fourier coefficients for u, and

$$\Delta A = \{\Delta a_0\ \Delta a_1\ \cdots\ \Delta a_n\ \Delta b_1\ \cdots \Delta b_n\}^{\mathrm{T}}$$

is the vector of the truncated Fourier coefficients for Δu, which is also the increment of A. The first and second derivatives of u are $u' = \mathbf{C}'^{\mathrm{T}}_s A$ and $u" = \mathbf{C}"^{\mathrm{T}}_s A$, respectively; the first and second derivatives of Δu are $\Delta u' = \mathbf{C}'^{\mathrm{T}}_s \Delta A$ and $\Delta u" = \mathbf{C}"^{\mathrm{T}}_s \Delta A$ respectively. Substituting $u = \mathbf{C}^{\mathrm{T}}_s A$ and $\Delta u = \mathbf{C}^{\mathrm{T}}_s \Delta A$ into Eq. (53) yields

$$(\omega_o^2 \mathbf{C}"^{\mathrm{T}}_s + 2\omega_o \xi \mathbf{C}'^{\mathrm{T}}_s + (\alpha + 3\varepsilon \mathbf{C}^{\mathrm{T}}_s A_o \mathbf{C}^{\mathrm{T}}_s A_o)\mathbf{C}^{\mathrm{T}}_s)\Delta A + f_\omega(\mathbf{C}^{\mathrm{T}}_s A_o)\Delta\omega = -f_o(\mathbf{C}^{\mathrm{T}}_s A_o, \tau) \quad (54)$$

where $u_o = \mathbf{C}^{\mathrm{T}}_s A_o$ is the trial solution of Eq. (52). Note that Eq. (54) is the incremental equation of Eq. (52).

4. Making harmonic balance for Eqs. (52) and (54) via Galerkin procedure. Premultiplying Eq. (52) with $u = \mathbf{C}^{\mathrm{T}}_s A$ by $\mathbf{C}_s$ and integrating the resulting

equation from $\tau = 0$ to 2π yield

$$\frac{1}{\pi}\int_0^{2\pi} \mathbf{C}_s(\omega^2 \mathbf{C}''^{\mathrm{T}}_s A + 2\omega_o \xi \mathbf{C}'^{\mathrm{T}}_s A + (\alpha + \varepsilon \mathbf{C}_s^{\mathrm{T}} A \mathbf{C}_s^{\mathrm{T}} A)\mathbf{C}_s^{\mathrm{T}} A - F\cos p\tau) d\tau = 0_{2n+1} \tag{55}$$

where 0_{2n+1} is the $(2n+1)$-dimensional zero vector. A similar procedure for Eq. (54) yields the incremental equation of Eq. (55):

$$\Phi_A \Delta A + \Phi_\omega \Delta\omega = -r_{A_0} \tag{56}$$

where

$$\Phi_A = \frac{1}{\pi}\int_0^{2\pi} \mathbf{C}_s(\omega_o^2 \mathbf{C}''^{\mathrm{T}}_s + 2\omega_o \xi \mathbf{C}'^{\mathrm{T}}_s + (\alpha + 3\varepsilon \mathbf{C}_s^{\mathrm{T}} A \mathbf{C}_s^{\mathrm{T}} A)\mathbf{C}_s^{\mathrm{T}} d\tau$$

is the Jacobian of Eq. (55) with respect to A,

$$\Phi_\omega = \frac{1}{\pi}\int_0^{2\pi} \mathbf{C}_s(2\omega_o \mathbf{C}''^{\mathrm{T}}_s + 2\xi \mathbf{C}'^{\mathrm{T}}_s) A_o d\tau$$

is the Jacobian of Eq. (55) with respect to ω, and

$$r_{A_0} = \frac{1}{\pi}\int_0^{2\pi} \mathbf{C}_s f_o(\mathbf{C}_s^{\mathrm{T}} A_o, \tau) d\tau$$

is the harmonic balanced residual of Eq. (55) associated with $u_o = \mathbf{C}_s^{\mathrm{T}} A_o$ and ω_o.

5. Applying Newton's method. Newton's method is an iterative method to obtain a solution q of A in Eq. (55). With a fixed ω in Eq. (55), the incremental

equation in Eq. (56) becomes

$$\Phi_q \Delta q = -r_q \tag{57}$$

where Φ_q is the Jacobian of Eq. (55) with respect to q, r_q is the residual of Eq. (55) with A_o replaced by q, and $\Delta q = -\Phi_q^{-1} r_q$ is the increment of q. One can update q by $q_o + \Delta q$, where q_o is an initial guess of A.When the norm of r_q is less than a preset tolerance, the solution of Eq. (52) is $u = \mathbf{C}_s^{\mathrm{T}} q_o$.

3.2.2 Modified IHB Method

A modified IHB method is introduced in this section, where r_q is obtained by the FFT and Newton's method is replaced by a quasi-Newton method that is Broyden's method. The associated linear differential equation of Eq. (52) is

$$\omega^2 u" + 2\omega\xi u' + \alpha u - F\cos p\tau = 0 \tag{58}$$

Substituting $u = \mathbf{C}_s^{\mathrm{T}} A$ into Eq. (58) and using Galerkin procedure for the resulting equation yield

$$\frac{1}{\pi}\int_0^{2\pi} \mathbf{C}_s(\omega^2 \mathbf{C}"_s^{\mathrm{T}} + 2\omega_o\xi \mathbf{C}'^{\mathrm{T}}_s + \alpha \mathbf{C}_s^{\mathrm{T}}) d\tau A - r_F = 0_{2n+1} \tag{59}$$

where r_F is the $(2n+1)$-dimensional vector whose $(p+1)^{\text{th}}$ entry is F. The Jacobian of Eq. (59) is used as an initial guess of Φ_q. It can be calculated as follows:

$$\begin{aligned}
\mathrm{B}_{q,0} &= \frac{1}{\pi}\int_0^{2\pi} \mathbf{C}_s(\omega^2 \mathbf{C}_s^{\text{"T}} + 2\omega_o\xi \mathbf{C}_s^{\text{'T}} + \alpha \mathbf{C}_s^{\mathrm{T}})d\tau \\
&= \omega^2 \begin{Bmatrix} 0 & 0_n^{\mathrm{T}} & 0_n^{\mathrm{T}} \\ 0_n & \mathrm{C}_1 & 0_{n\times n} \\ 0_n & 0_{n\times n} & \mathrm{S}_1 \end{Bmatrix} + 2\omega\xi \begin{Bmatrix} 0 & 0_n^{\mathrm{T}} & 0_n^{\mathrm{T}} \\ 0_n & 0_{n\times n} & \mathrm{C}_2 \\ 0_n & \mathrm{S}_2 & 0_{n\times n} \end{Bmatrix} \\
&+ \alpha \begin{Bmatrix} \frac{1}{2} & 0_n^{\mathrm{T}} & 0_n^{\mathrm{T}} \\ 0_n & \mathrm{E}_n & 0_{n\times n} \\ 0_n & 0_{n\times n} & \mathrm{E}_n \end{Bmatrix}
\end{aligned} \tag{60}$$

where

$$\mathrm{C}_1 = \mathrm{S}_1 = \begin{Bmatrix} 1^2 & \cdots & 0 \\ \vdots & \ddots & \vdots \\ 0 & \cdots & n^2 \end{Bmatrix}$$

$$\mathrm{C}_2 = -\mathrm{S}_2 = \begin{Bmatrix} 1 & \cdots & 0 \\ \vdots & \ddots & \vdots \\ 0 & \cdots & n \end{Bmatrix}$$

0_n is the n-dimensional zero vector and E_n is the n-dimensional identity matrix. With the last expression in Eq. (60), the Jacobian of the associated linear equation of Eq. (52) can be automatically generated. The solution of Eq. (59) $q_0 = -\mathrm{B}_{q,0}^{-1} r_F$ is used as an initial guess of q. The solution of Eq. (58) is $\mathbf{C}_s^{\mathrm{T}} q_0$.

If the nonlinearity in Eq. (52) is weak, i.e., ε is small, the solution of Eq. (52) can be iteratively obtained from that of Eq. (58). If the nonlinearity in Eq. (52)

is strong, i.e., ε is large, the solution of Eq. (52) can be obtained from that of Eq. (58) by gradually incrementing the nonlinear stiffness coefficient from $\varepsilon_0 = 0$ to ε with a step size $\Delta\varepsilon$. The final iterated solution $\mathrm{q}^{(h)}$, where h is the step number to recover the nonlinear stiffness coefficient, and the final approximated Jacobian $\mathrm{B}_q^{(h)}$ of Eq. (52) with an intermediate parameter $\varepsilon^{(h)} = h\Delta\varepsilon$ are used as initial guesses of the solution and the approximated Jacobian of Eq. (52) with the parameter $\varepsilon^{(h+1)}$, respectively. The procedure of the modified IHB method to solve Eq. (52) with a $\varepsilon^{(h)}$ is shown below.

1. Calculating the residual of Eq. (55) by the FFT. In the k^{th} iteration, the approximated Jacobian and the solution are $\mathrm{B}_{q,k}$ and q_k, respectively. The harmonic balanced residual of Eq. (55) with a given ω_o is

$$\mathrm{r}_{q_k} = \frac{1}{\pi}\int_0^{2\pi} \mathbf{C}_s f_o(\mathbf{C}_s^{\mathrm{T}} q_k, \tau) d\tau \tag{61}$$

   A fast and easy alternative to obtain the residual in Eq. (61) is via the FFT. The period of $f_o(\mathbf{C}_s^{\mathrm{T}} q_k, \tau)$ is $T = 2\pi$, and $2N$ points, where $N > n$, that are equally distributed in $[0, 2\pi)$ are selected as discretized points: $\tau_i = i\frac{2\pi}{2N}$,where $i = 0, \ldots, 2N-1$. Values of $f_o(\mathbf{C}_s^{\mathrm{T}} q_k, \tau)$ at τ_i are $f_o(\mathbf{C}_s^{\mathrm{T}} q_k, \tau_i)$. The DFT of $f_o(\mathbf{C}_s^{\mathrm{T}} q_k, \tau_i)$ is

$$F_o(q_k, K) = \frac{1}{2N}\sum_{i=0}^{2N-1} f_o(\mathbf{C}_s^{\mathrm{T}} q_k, \tau_i) e^{-\mathrm{j}2\pi K i/(2N)} \tag{62}$$

   where $K = 0, \ldots, 2N-1$; $F_o(q_k, K)$ is a complex number and can be written as $F_o(q_k, K) = F_{\mathrm{Re}}^{(q_k,K)} + \mathrm{j}F_{\mathrm{Im}}^{(q_k,K)}$, where $F_{\mathrm{Re}}^{(q_k,K)}$ and $F_{\mathrm{Im}}^{(q_k,K)}$ are real numbers.

Coefficients of $\cos K\tau$ and $\sin K\tau$ are

$$Cos^{(q_k,K)} = \sqrt{(F_{\mathrm{Re}}^{(q_k,K)})^2 + (F_{\mathrm{Im}}^{(q_k,K)})^2}\cos\left(\tan^{-1}\left(\frac{F_{\mathrm{Im}}^{(q_k,K)}}{F_{\mathrm{Re}}^{(q_k,K)}}\right)\right) \tag{63}$$

$$Sin^{(q_k,K)} = \sqrt{(F_{\mathrm{Re}}^{(q_k,K)})^2 + (F_{\mathrm{Im}}^{(q_k,K)})^2}\sin\left(\tan^{-1}\left(\frac{F_{\mathrm{Im}}^{(q_k,K)}}{F_{\mathrm{Re}}^{(q_k,K)}}\right)\right) \tag{64}$$

respectively. Consequently, r_{q_k} can be approximated by

$$\mathrm{r}_{q_k} = \{Cos^{(q_k,0)} \cdots Cos^{(q_k,n)}\ Sin^{(q_k,1)} \cdots Sin^{(q_k,n)}\}^{\mathrm{T}} \tag{65}$$

2. Updating the approximated Jacobian and the solution using Broyden's method. The incremental equation in Eq. (57) using Broyden's method is

$$q_{k+1} - q_k = -\mathrm{B}_{q,k}^{-1}\mathrm{r}_{q_k} \tag{66}$$

The residual in the $(k+1)^{\mathrm{th}}$ iteration $\mathrm{r}_{q_{k+1}}$ can be obtained by using Eqs. (62)–(65) again with q_k replaced by q_{k+1}, which is obtained from Eq. (66). The approximated Jacobian in the $(k+1)^{\mathrm{th}}$ iteration is updated by

$$\mathrm{B}_{q,k+1} = \mathrm{B}_{q,k} + \frac{(y_k - \mathrm{B}_{q,k}s_k)s_k^{\mathrm{T}}}{s_k^{\mathrm{T}}s_k} \tag{67}$$

where $s_k = q_{k+1} - q_k$ and $y_k = r_{q_{k+1}} - r_{q_k}$. When the norm of $r_{q_{k+1}}$ is less than a preset tolerance, the solution of Eq. (52) is $\mathbf{C}_s^{\mathrm{T}} q_{k+1}$. Accuracy of the solution from the modified IHB method given by the tolerance, which can be selected to be 10^{-6} here, is the same as that from the original IHB

method. Solutions of Duffing's equation from the modified IHB method and Runge–Kutta method are shown in Fig. 28, and they are in excellent agreement. The calculation time using the original IHB method is 0.25 s, and that using the modified IHB method is 0.003 s, which is almost one hundredth of the former.

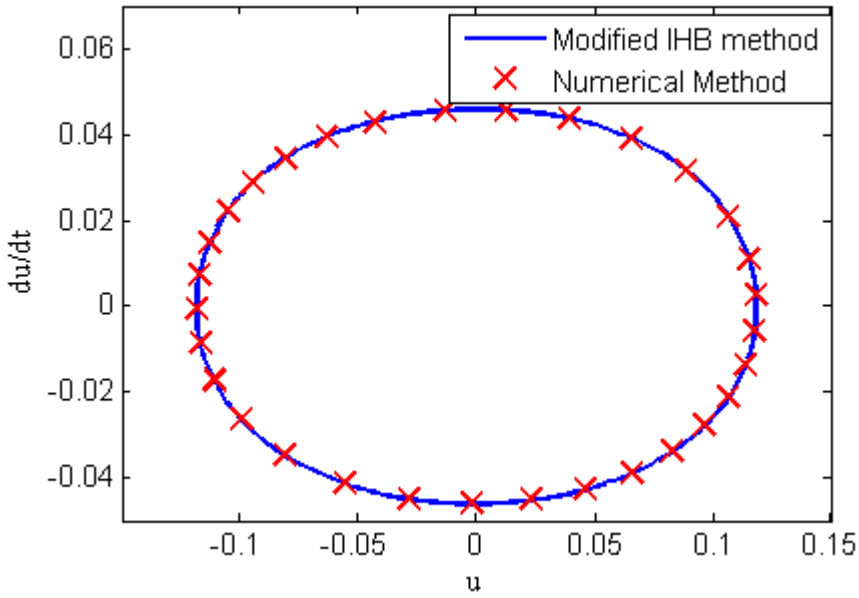

Figure 28: Solutions of Duffing's equation with $n = 20$, $N = 64$, $\xi = 0.02$, $\alpha = 1$, $\varepsilon = 1$, $\omega_f = 0.4$, and $F = 0.1$ from the modified IHB method and Runge–Kutta method

3.2.3 Arc-length Method for the Modified IHB Method

To obtain an amplitude–frequency response curve of Eq. (52), a path of the steady-state solution versus the varying excitation frequency $\omega_f = p\omega$ needs to be cal-

culated. To avoid non-convergence at a sharp peak of an amplitude–frequency response curve, either the selective coefficient method [69] or the arc-length method with the path-following technique [53] can be used. In the modified IHB method, since the Jacobian of nonlinear algebraic equations with a current excitation frequency is approximated via iterations from its initial guess, which is the Jacobian of the nonlinear equations with a previous excitation frequency, constitution of the solution of the current equations is the same as that of the previous equations. Hence, the arc-length method with the path-following technique is a suitable method, and $x = \{q^{\mathrm{T}} \;\; \omega\}^{\mathrm{T}}$ is chosen as the newvariable. The augmenting equation of the arc-length method is defined by

$$g(x) - \eta = 0 \tag{68}$$

where g is a path function and η is a path parameter. A combination of Eqs. (55) and (68) forms a complete set of equations:

$$\begin{cases} \frac{1}{\pi}\int_0^{2\pi} \mathbf{C}_s(\omega^2 \mathbf{C}_s''^{\mathrm{T}} A + 2\omega_o \xi \mathbf{C}_s'^{\mathrm{T}} A + (\alpha + \varepsilon \mathbf{C}_s^{\mathrm{T}} A \mathbf{C}_s^{\mathrm{T}} A)\mathbf{C}_s^{\mathrm{T}} A - F\cos p\tau) d\tau = 0_{2n+1} \\ g(\{q^{\mathrm{T}} \;\; \omega\}^{\mathrm{T}}) - \eta = 0 \end{cases} \tag{69}$$

A path of the steady-state solution can be traced by actively incrementing η. The incremental equation of Eq. (69) with some η is

$$\Phi_x \Delta x = \begin{Bmatrix} \Phi_q & \Phi_\omega \\ dg/dx^{\mathrm{T}} \end{Bmatrix} \Delta x = - \begin{Bmatrix} r_x \\ g(x) - \eta \end{Bmatrix} \tag{70}$$

where $\Delta x = \{\Delta q^{\mathrm{T}} \;\; \Delta\omega\}^{\mathrm{T}}$ and Φ_x is the Jacobian of Eq. (69); Φ_ω can be obtained via the FFT from Eqs. (62)–(65) with $f_o(\mathbf{C}_s^{\mathrm{T}} q_k, \tau)$ and r_{q_k} replaced by

$2\omega_o \mathbf{C}''^{\mathrm{T}}_s q + 2\xi \mathbf{C}'^{\mathrm{T}}_s q$ and Φ_ω, respectively. When the solution of Eq. (69) with that path parameter η and the approximated Jacobian with respect to q, i.e., B_q, are obtained, η is updated by $\eta + \Delta\eta$, and

$$x_0 = x_p + x_d \Delta\eta \tag{71}$$

where x_p is the solution of Eq. (69) with the previous η and

$$x_d = \frac{(x_p - x_b)}{||x_p - x_b||}$$

in which x_b is the solution of Eq. (69) with η being that before the previous one, is the unit vector for predicting the direction of change of the solution of Eq. (69) with the updated η and is used as an initial guess of the new variable x of Eq. (69) with the updated η. If the path function is

$$g(x) = x_d^{\mathrm{T}}(x - x_p)$$

the derivative of g with respect to x is $dg/dx^{\mathrm{T}} = x_d^{\mathrm{T}}$. An initial guess of the Jacobian of Eq. (69) with the updated η is chosen to be

$$\mathrm{B}_{x,0} = \left\{ \begin{array}{cc} \mathrm{B}_{q,0} & \mathrm{B}_{\omega,0} \\ & x_d^{\mathrm{T}} \end{array} \right\} \tag{72}$$

where $\mathrm{B}_{q,0} = \mathrm{B}_q$ is an initial guess of Φ_q and $\mathrm{B}_{\omega,0} = \Phi_\omega$ In updating $\mathrm{B}_{x,k}$ using Broyden's method in the k^{th} iteration, all the entries of $\mathrm{B}_{x,k}$ can be changed. However, the last row of $\mathrm{B}_{x,k}$ will remain a constant vector x_d^{T}, which is proved below.

Replacing Φ_x in Eq. (70) by $\mathrm{B}_{x,k}$ and x by x_k in the resulting equations yields

$$\mathrm{B}_{x,k}\Delta x = \left\{ \begin{array}{c} \mathrm{B}_{q,k}\Delta q \;\; \mathrm{B}_{\omega,k}\Delta x \\ x_d^{\mathrm{T}}\Delta x \end{array} \right\} = -r_k \tag{73}$$

where $r_k = \{r_{x_k}^{\mathrm{T}} \;\; g(x_k) - \eta\}^{\mathrm{T}}$ is the residual of Eq. (70) at x_k. The last row in Eq. (73) is

$$x_d^{\mathrm{T}}\Delta x = -g(x_k) + \eta \tag{74}$$

The residual of Eq. (70) in the $(k+1)^{\mathrm{th}}$ iteration at $\mathrm{x}_{k+1} = \mathrm{x}_k + \Delta\mathrm{x}$ is $r_{k+1} = \{r_{x_{k+1}}^{\mathrm{T}} \;\; g(x_{k+1}) - \eta\}^{\mathrm{T}}$. The last entry of r_{k+1} is

$$g(x_{k+1}) - \eta = g(\mathrm{x}_k + \Delta\mathrm{x}) - \eta \tag{75}$$

Using $g(x) = x_d^{\mathrm{T}}(x - x_p)$ in above equation yields

$$g(\mathrm{x}_k + \Delta\mathrm{x}) - \eta = x_d^{\mathrm{T}}(x_k - x_p) - \eta + x_d^{\mathrm{T}}\Delta x \tag{76}$$

Substituting Eq. (74) into Eq. (76) yields

$$x_d^{\mathrm{T}}(x_k - x_p) - \eta + x_d^{\mathrm{T}}\Delta x = g(x_k) - \eta - g(x_k) + \eta = 0$$

which means that $r_{k+1} = \{r_{x_{k+1}}^{\mathrm{T}} \;\; 0\}^{\mathrm{T}}$. Using $y_k = r_{k+1} - r_k$ and $\mathrm{s}_k = \Delta x$ in Eq. (67)

to update $\mathrm{B}_{x,k}$ yields

$$\begin{aligned}
\mathrm{B}_{x,k+1} &= \mathrm{B}_{x,k} + \frac{(r_{k+1} - r_k - \mathrm{B}_{q,k} s_k)\Delta x^{\mathrm{T}}}{\Delta x^{\mathrm{T}} \Delta x} \\
&= \mathrm{B}_{x,k} + \frac{r_{k+1} \Delta x^{\mathrm{T}}}{\Delta x^{\mathrm{T}} \Delta x} \\
&= \mathrm{B}_{x,k} + \frac{\{r_{x_{k+1}}^{\mathrm{T}} \;\; 0\}^{\mathrm{T}} \Delta x^{\mathrm{T}}}{\Delta x^{\mathrm{T}} \Delta x} \\
&= \mathrm{B}_{x,k} + \frac{\{\Delta x \cdot r_{x_{k+1}}^{\mathrm{T}} \;\; 0\}^{\mathrm{T}}}{\Delta x^{\mathrm{T}} \Delta x}
\end{aligned} \tag{77}$$

which means that the last row of $\mathrm{B}_{x,k+1}$ is equal to that of $\mathrm{B}_{x,k}$. Hence, the last row of $\mathrm{B}_{x,k}$ for any k is equal to that of $\mathrm{B}_{x,0}$, which is x_d^{T}, and the invariance property of the last row of $\mathrm{B}_{x,k}$ is proved.

3.2.4 Stability of Periodic Solutions

Stability of a steady-state solution from the modified IHB method can be evaluated by Floquet theory. Assume u_{ss} is the steady-state solution that satisfies Eq. (52) and δu is a small perturbation around u_{ss}. Using $u = u_{ss} + \delta u$ in Eq. (52) yields

$$\omega^2 \delta u" + 2\omega\xi \, \delta u' + (\alpha + 3\varepsilon u_{ss}^2)\delta u = -f_0(u_{ss}, \tau) = 0 \tag{78}$$

Transforming Eq. (78) to a state-space form with a state-space variable $V = \{\delta u \;\; \delta u'\}^{\mathrm{T}}$ yields

$$V' = \left\{ \begin{array}{c} \delta u' \\ \delta u" \end{array} \right\} = \left\{ \begin{array}{cc} 0 & 1 \\ -\frac{(\alpha + 3\varepsilon u_{ss}^2)}{\omega^2} & -\frac{2\xi}{\omega} \end{array} \right\} \left\{ \begin{array}{c} \delta u \\ \delta u' \end{array} \right\} = \Theta(\tau) V \tag{79}$$

where $\Theta(\tau)$ is a periodic matrix with respect to τ, whose period is 2π. Stability of Eq. (78) can be evaluated by calculating eigenvalues of the transformation matrix Q that transforms V at $\tau = 2n\pi$ to that at $\tau = 2(n+1)\pi$. The transformation matrix Q can be calculated using Hsu's method [57] in the form

$$Q = \prod_{i_Q=1}^{N_Q} \exp(\Delta\tau \cdot \Theta(i_Q \cdot \Delta\tau)) \tag{80}$$

where N_Q is the number of equal divisions of the period and $\Delta\tau = 2\pi/N_Q$ is the length of one division. If all of the eigenvalues of Q is inside a unit circle, the steady-state solution is stable; otherwise, the solution is unstable. Furthermore, if the unstable solution yields an eigenvalue that is less than -1, a period-doubling bifurcation occurs and there are stable subharmonic responses [53]. When there are two complex conjugate eigenvalues that escape from the unit circle, a Hopf bifurcation occurs. An amplitude–frequency response curve of Duffing's equation calculated using the arclength method with the path-following technique is shown in Fig. 29, and stability of the solution is indicated.

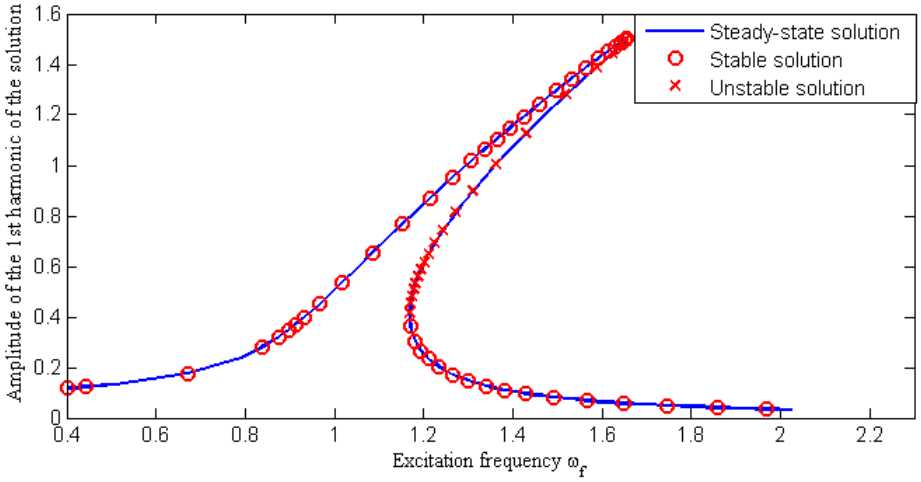

Figure 29: Amplitude-frequency response curve of Duffing's equation with $n = 20$, $N = 64$, $\xi = 0.02$, $\alpha = 1$, $\varepsilon = 1$, and $F = 0.1$, where stability of the solution is indicated

3.2.5 Bifurcations of Mathieu-Duffing Equation by IHB Method

Mathieu-Duffing equation represents a parametrically excited nonlinear system:

$$\ddot{u} + 2\hat{\xi}\dot{u} - (\hat{\alpha} + \beta \sin \Omega t)u + \gamma u^3 = 0 \tag{81}$$

where $\hat{\xi} = 0.125$ is the damping ratio, $\hat{\alpha} = 1$ is a linear stiffness coefficient, β is the amplitude of the parametric excitation, $\Omega = 2$ is the frequency of the excitation, and $\gamma = 1$ is a nonlinear stiffness coefficient. Bifurcations occur when β varies, and the modified IHB method can be used to study it. The dimensionless time variable

is $\tau = \omega t$; substituting the expression into Eq. (81) yields

$$\omega^2 u" + 2\omega\hat{\xi}u' - (\hat{\alpha} + \beta \sin p\tau)u + \gamma u^3 = 0 \tag{82}$$

where $p = \Omega/\omega$ indicates the number of period-doubling bifurcations. If $p = 1, 2, 4, \ldots$ are selected in Eq. (82), period-$1, 2, 4, \ldots$ solutions can be calculated. The period-p solution can be solved by the modified IHB method with a controlled amplitude that is a Fourier coefficient of the solution of Eq. (82). Making harmonic balance for Eq. (82) with $u = \mathbf{C}_s^{\mathrm{T}} A$ yields

$$\frac{1}{\pi}\int_0^{2\pi} \mathbf{C}_s(\omega^2 \mathbf{C}"_s^{\mathrm{T}} A + 2\omega_o \xi \mathbf{C}'^{\mathrm{T}}_s A - (\hat{\alpha} + \beta \sin p\tau - \gamma \mathbf{C}_s^{\mathrm{T}} A \mathbf{C}_s^{\mathrm{T}} A)\mathbf{C}_s^{\mathrm{T}} A) d\tau = 0_{2n+1} \tag{83}$$

The incremental equation of Eq. (83) is

$$\Phi_A \Delta A + \Phi_\beta \Delta\beta = -r_{X_0} \tag{84}$$

where Φ_A is the Jacobian of Eq. (83) with respect to A, $\Phi_\beta = -\frac{1}{\pi}\int_0^{2\pi} \mathbf{C}_s \sin p\tau \mathbf{C}_s^{\mathrm{T}} A d\tau$ is the Jacobian of Eq. (83) with respect to β, and r_{X_0} is the residual of Eq. (83) with $\{A^{\mathrm{T}} \;\; \beta\}^{\mathrm{T}}$ replaced by a trial solution $X_0 = \{A_0^{\mathrm{T}} \;\; \beta_0\}^{\mathrm{T}}$. Let the amplitude of the n_c^{th} cosine term of Fourier series of u, which is the $(n_c+1)^{\mathrm{th}}$ entry of A, be the controlled amplitude. The solution of A in Eq. (83) is

$$q = \{a_0 \; \cdots \; a_{n_c-1} \; \beta \; a_{n_c+1} \; \cdots \; a_n \; b_1 \; \cdots \; b_n\}^{\mathrm{T}}$$

and Eq. (84) becomes

$$\Phi_q \Delta q = -r_q \tag{85}$$

where Φ_q is the Jacobian of Eq. (83) with respect to q, which is Φ_A with its n_c^{th} column replaced by Φ_β, Δq is the increment of q, and r_q is the residual of Eq. (83) at q.With some trials, the solution of Fourier coefficients with $\beta_0 = 3.6$ is

$$\begin{aligned} A_0 = \{&0.7881 \;\; -1.3956 \;\; 0.2686 \;\; 0.1121 \;\; -0.0260 \;\; 0.0026 \;\; -0.0008 \;\; -0.0001 \\ &= 0.0001 \;\; 0 \;\; 1.9884 \;\; -0.1693 \;\; 0.0471 \;\; -0.0175 \;\; -0.0042 \;\; 0.0021 \;\; -0.0003 \;\; 0 \;\; 0\} \end{aligned}$$

when $n = 9$. In the procedure to find A_0, the initial guess of Φ_q can be obtained from the Jacobian of linear algebraic equations given in Sec. 3.2.2. The modified IHB method can be used to obtain the bifurcation diagram of Mathieu-Duffing equation.

When β increases from $\beta_0 = 3.6$, solutions of Mathieu-Duffing equation are stable period-1 solutions, as shown in Fig. 30. The second entry of

$$A_1 = \{a_0^{(1)} \;\cdots\; a_n^{(1)} \; b_1^{(1)} \;\cdots\; b_n^{(1)}\}^{\mathrm{T}}$$

which is the vector of Fourier coefficients of a period-1 solution, is used as the controlled amplitude, i.e., $n_c = 1$. The controlled amplitude is increased with a step size of 0.0005, until the period-1 solution is unstable at the critical point $\beta_1 = 4.825$. Let the solution of Eq. (83) at β_1 be

$$A_1 = \{a_0^{(1)*} \;\cdots\; a_n^{(1)*} \; b_1^{(1)*} \;\cdots\; b_n^{(1)*}\}^{\mathrm{T}}$$

The vector of Fourier coefficients of a period-2 solution is

$$A_2 = \{a_0^{(2)} \ \cdots \ a_{2n}^{(2)} \ b_1^{(2)} \ \cdots \ b_{2n}^{(2)}\}^{\mathrm{T}}$$

The initial guess of A_2 is given by $a_0^{(2)} = a_0^{(1)*}$, $a_{2j}^{(2)} = a_j^{(1)*}$, $b_{2j}^{(2)} = b_j^{(1)*}$, where $j = 1, \ldots, n$, and $a_{2j-1}^{(2)} = 0$, $b_{2j-1}^{(2)} = 0$, where $j = 1, \ldots, n$. The controlled amplitude for bifurcation solutions is $a_1^{(2)}$, and it is increased with a step size of 0.0001, until the period-2 solution is unstable at the critical point $\beta_2 = 5.194$. With the same procedure, the critical point corresponding to the unstable period-4 solution is $\beta_4 = 5.253$. Period-2 and period-4 solutions are shown in Figs. 31 and 32, respectively. The bifurcation diagram of $u(\tau = 0)$ versus β is shown in Fig. 33.

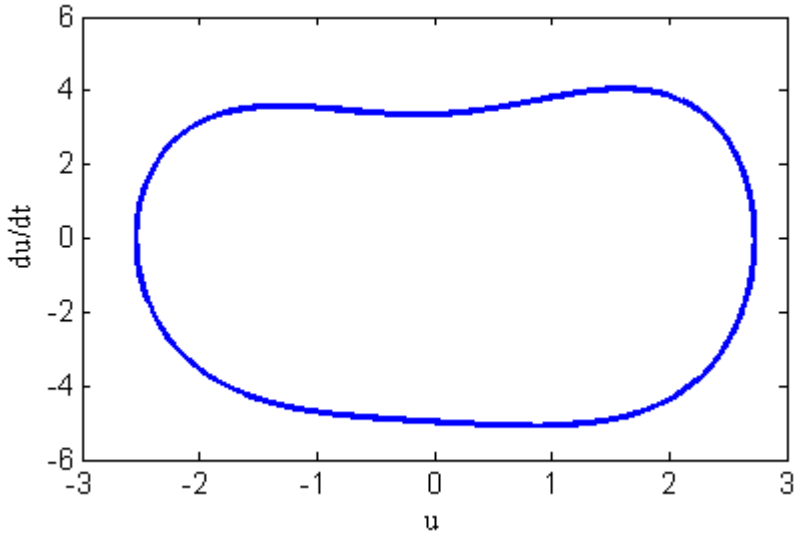

Figure 30: Period-1 solution of Mathieu-Duffing equation with $\beta = 4.1906$

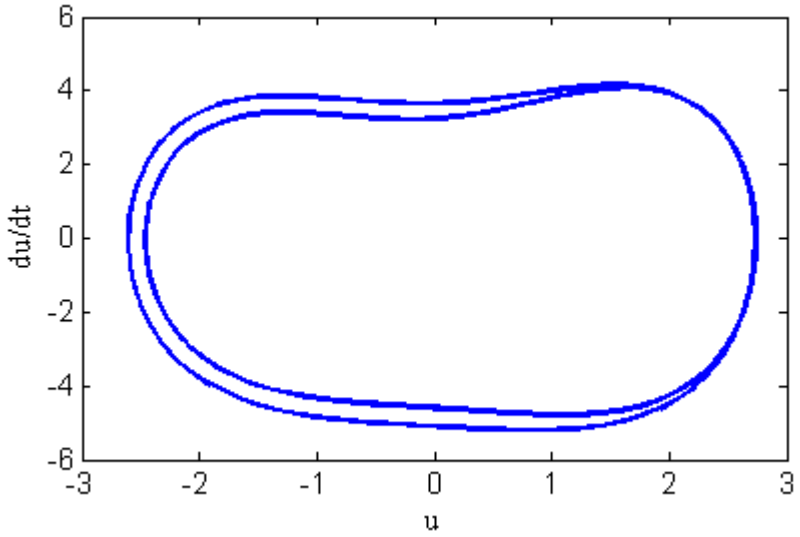

Figure 31: Period-2 solution of Mathieu-Duffing equation with $\beta = 4.8390$

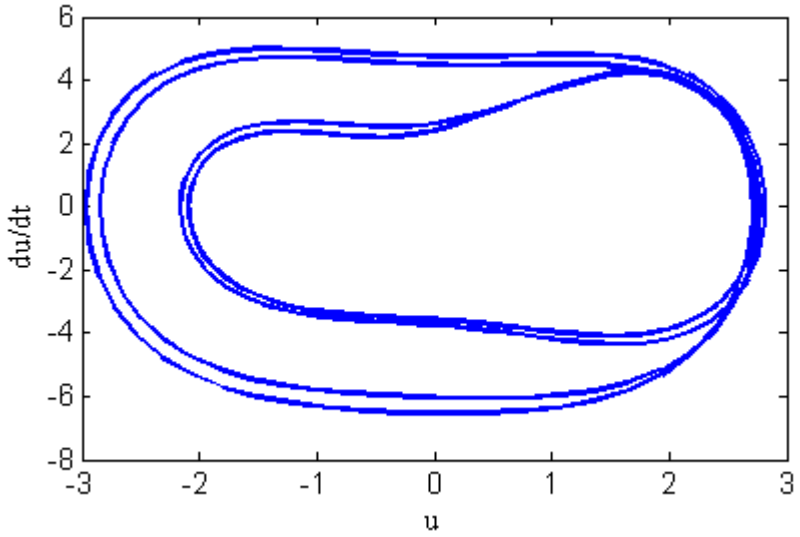

Figure 32: Period-4 solution of Mathieu-Duffing equation with $\beta = 5.2508$

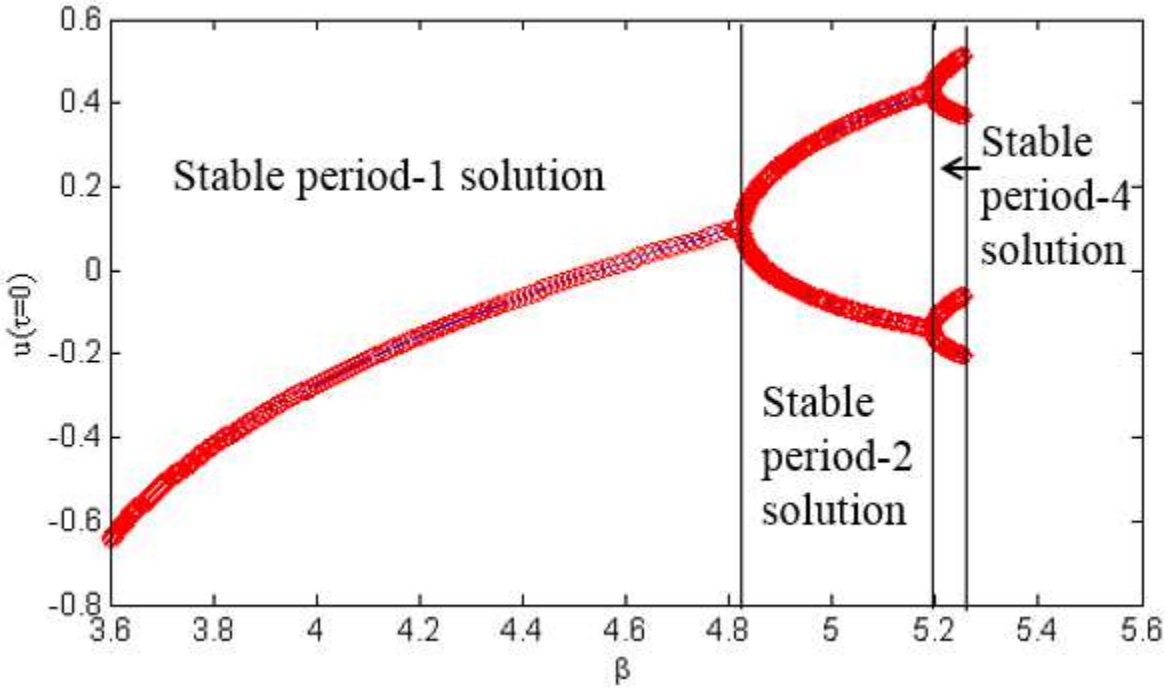

Figure 33: Bifurcation diagram of Mathieu-Duffing equation

3.3 Spatial and Temporal Hamonic Balance (STHB) Method

3.3.1 Introduction to the STHB Method

In Sec. 3.2, we introduce the modified IHB method to obtain the periodic solution of ordinary differential equations and conduct the stability analysis. However, there are a lot of problems involving partial differential equations (PDFs), such as the beam vibration, flexiable structure dynamics and other higher dimensional systems. The essence of the spatial and temporal harmonic balance (STHB) method is to treat the temporal coordinate the same as the spatial coordinate when the desired steady-

state solution is periodic. In this sense, the dimension of the spatial coordinate can be any positive integer, and the STHB method shown here for a one-dimensional continuous system can be readily extended for higher dimensional systems.

To solve a governing PDE of a one-dimensional continuous system, a global spatial discretization method can be used, if the geometric shape of the system is simple and smooth. Exact eigenfunctions of the system can be used to find the exact solution of the PDE. However, when exact eigenfunctions do not exist, Galerkin method can be used, which employs a series of trial functions as basis functions to determine approximate solutions [70]. When an associated set of ordinary differential equations (ODEs) of the PDE in terms of generalized coordinates is obtained by Galerkin method, periodic steady-state responses of the system can be obtained by the harmonic balance method [49], the harmonic balance Newton-Raphson (HBNR) method [71], and the incremental harmonic balance (IHB) method [48]. Ferri [72] showed the equivalance of the HBNR and IHB methods. Ling and Wu [63] incorporated the fast Fourier transform (FFT) into the IHB method to reduce computation time. Guillen and Pierre [73] used Broyden's method in the harmonic balance method. Wang and Zhu [32] introduced a modified IHB method where the FFT and Broyden's method are used. Stability analysis of periodic steady-state responses of a nonlinear PDE can be conducted on a set of linearized equations of the associated set of ODEs, which describes a linear-time-periodic (LTP) system. There are two stability analysis methods: a numerical method to obtain eigenvalues of the transformation matrix of the LTP system [57], and Hill's method to calculate eigenvalues of Toeplitz form of its system matrix [74].

A global spatial discretization method usually needs complicated calculation in derivation of the associated set of ODEs. In this work, a new STHB method is developed to solve for periodic steady-state responses of a one-dimensional second-order continuous system with geometric nonlinearity and fixed-fixed boundary conditions. Spatial harmonic balance procedures with series of sine and cosine basis functions can be efficiently conducted by the fast discrete sine transform (DST) and the fast discrete cosine transform (DCT), respectively [75]. The temporal harmonic balance procedure with basis functions of Fourier series can be efficiently conducted by the FFT. The residual and the exact Jacobian matrix of an associated set of algebraic equations that are temporal harmonic balanced equations of the ODEs, which are used in Newton-Raphson method, can be directly obtained by spatial and temporal harmonic balance procedures for the PDE, where derivation of the associated set of ODEs can be avoided. The relationship of Jacobian matrix of the algebraic equations and Toeplitz form of the system matrix of the LTP system is derived in this work. Stability analysis of periodic solutions from the STHB method can be conducted by Hill's method without derivation of the ODEs.

Some useful formulas for the development of the STHB method are established in Sec. 3.3.2. The development of the STHB method for a fixed-fixed string with geometric nonlinearity is illustrated in Sec. 3.3.3, where a summarized algorithm of the STHB method is shown. Stability analysis of periodic steady-state responses of the string is established in Sec. 3.3.4, where its results and stability are shown by frequency-response curves with different nonlinearities and numbers of trial functions. Periodic responses of a string with a complex boundary condition with a spring at the boundary are obtained by the STHB method in Sec. 3.3.5, where the

spectral Tau method [76] is used to deal with the boundary condition.

3.3.2 Preliminaries for Deriving the STHB Method

a) For matrices **A**, **B**, **C** and **D** of such sizes that matrix products **AC** and **BD** can be formed, the mixed-product property of Kronecker product is

$$(\mathbf{A}\otimes\mathbf{B})(\mathbf{C}\otimes\mathbf{D}) = (\mathbf{AC})\otimes(\mathbf{BD}) \tag{86}$$

where $\otimes$ denotes Kronecker product. Two formulas that can be derived from the mixed-product property are

$$(\mathbf{AB})\otimes\mathbf{E}_N = (\mathbf{A}\otimes\mathbf{E}_N)(\mathbf{B}\otimes\mathbf{E}_N) \tag{87}$$

$$\mathbf{M}(\mathbf{p}^{\mathrm{T}}\otimes\mathbf{E}_N) = (\mathbf{p}^{\mathrm{T}}\otimes\mathbf{E}_N)(\mathbf{E}_{2M+1}\otimes\mathbf{M}) \tag{88}$$

where $\mathbf{E}_N$ and $\mathbf{E}_{2M+1}$ are $N\times N$ and $(2M+1)\times(2M+1)$ identity matrices, respectively, $\mathbf{p}$ is a $(2M+1)\times 1$ column vector, $\mathbf{M}$ is a $N\times N$ matrix, and the superscript T denotes transpose of a vector or matrix. The proof of Eqs. (87) is straightforward by writing $\mathbf{E}_N$ as $\mathbf{E}_N\mathbf{E}_N$ and using the mixed-product property. For the proof of Eq. (88), noting that $\mathbf{M} = \{1\}\otimes\mathbf{M}$, where $\{1\}$ is a 1×1 matrix with the element of 1, and using the mixed-product property on the left-hand side of Eq. (88) yield

$$\mathbf{M}(\mathbf{p}^{\mathrm{T}}\otimes\mathbf{E}_N) = \mathbf{p}^{\mathrm{T}}\otimes\mathbf{M} \tag{89}$$

Using the mixed-product property on the right-hand side of Eq. (89) again yields the right-hand side of Eq. (88).

b) A function $\Gamma(x,t)$ with $x \in [0,1]$ and $t \in [0,2\pi]$ can be approximated by a finite series of basis functions

$$\Gamma(x,t) = \sum_{n=1}^{N} \sum_{m=-M}^{M} c_{nm} \phi_m(t) \eta_n(x) \tag{90}$$

where $\phi_m(t) = \exp(\mathrm{j}mt)$ is the basis function of Fourier series in the temporal coordinate, j denotes the imaginary unit, $\eta_n(x)$ is the basis function in the spatial coordinate, M is the truncated number of Fourier series, N is the number of basis functions in the spatial coordinate, and c_{nm} is the coefficient of $\phi_m(t)\eta_n(x)$. Sets of $\phi_m(t)$ and $\eta_n(x)$ are denoted by vectors $\Phi = \{\phi_{-M}(t) \ \cdots \ \phi_M(t)\}^{\mathrm{T}}$ and $\mathbf{H} = \{\eta_1(x) \ \cdots \ \eta_N(x)\}^{\mathrm{T}}$, respectively, and a $N \times (2M+1)$ coefficient matrix denoted by $\mathbf{C}$ is formed with c_{nm} being its element on the n^{th} row and the $(m + M + 1)^{th}$ column. If $\eta_n(x) = \sin(n\pi x)$, the set of $\eta_n(x)$ is denoted by $\mathbf{H} = \mathbf{H}_s$. If $\eta_n(x) = \cos[(n-1)\pi x]$, the set of $\eta_n(x)$ is denoted by $\mathbf{H} = \mathbf{H}_c$. Evaluating $\Gamma(x,t)$ at $\left\{x_k := \frac{k}{N_S}\right\}_{k=1,\ ...,\ N_s-1}$ and $\left\{t_i := \frac{2\pi i}{M_S}\right\}_{i=1,\ ...,\ M_s}$, where $N_S > N$ and $M_S > 2M$, yields a $(N_S - 1) \times M_S$ matrix

$$\tilde{\Gamma} = \begin{Bmatrix} \Gamma(x_1,t_1) & \cdots & \Gamma(x_1,t_{M_S}) \\ \vdots & \ddots & \vdots \\ \Gamma(x_{N_S-1},t_1) & \cdots & \Gamma(x_{N_S-1},t_{M_S}) \end{Bmatrix} \tag{91}$$

For $\eta_n(x) = \sin(n\pi x)$, Eq. (91) can be expressed by$\tilde{\Gamma} = \tilde{\mathbf{H}}_s^{\mathrm{T}} \mathbf{C}_s \tilde{\Phi}$, where

$$\tilde{\mathbf{H}}_s = \begin{Bmatrix} \sin(\pi \frac{1}{N_S}) & \cdots & \sin(N\pi \frac{1}{N_S}) \\ \vdots & \ddots & \vdots \\ \sin(\pi \frac{N_S-1}{N_S}) & \cdots & \sin(N\pi \frac{N_S-1}{N_S}) \end{Bmatrix} \tag{92}$$

$$\tilde{\Phi} = \begin{Bmatrix} \exp\left(\mathrm{j}(-M)\frac{2\pi}{M_S}\right) & \cdots & \exp\left(\mathrm{j}(-M)\frac{2\pi M_S}{M_S}\right) \\ \vdots & \ddots & \vdots \\ \exp\left(\mathrm{j}M\frac{2\pi}{M_S}\right) & \cdots & \exp\left(\mathrm{j}M\frac{2\pi M_S}{M_S}\right) \end{Bmatrix} \tag{93}$$

$\mathbf{C}_s$ is a coefficient matrix that can be obtained by

$$\mathbf{C}_s = \frac{1}{\pi} \tilde{\mathbf{H}}_s \tilde{\Gamma} \tilde{\Psi}^{\mathrm{T}} \tag{94}$$

in which $1/\pi$ is a mormalization coefficient, and

$$\tilde{\Psi} = \begin{Bmatrix} \exp\left(\mathrm{j}M\frac{2\pi}{M_S}\right) & \cdots & \exp\left(\mathrm{j}M\frac{2\pi M_S}{M_S}\right) \\ \vdots & \ddots & \vdots \\ \exp\left(\mathrm{j}(-M)\frac{2\pi}{M_S}\right) & \cdots & \exp\left(\mathrm{j}(-M)\frac{2\pi M_S}{M_S}\right) \end{Bmatrix} \tag{95}$$

The element of $\mathbf{C}_s$ on the n^{th} row and the $(m+M+1)^{th}$ column is the coefficient c_{nm} of $\phi_m(t)\eta_n(x) = \exp(\mathrm{j}mt)\sin(n\pi x)$. Premultiplication of $\tilde{\Gamma}$ by $2\tilde{\mathbf{H}}_s$, which is a spatial harmonic balance procedure, can be efficiently calculated by the fast DST, and its postmultiplication by $\frac{1}{2\pi}\tilde{\Psi}^{\mathrm{T}}$, which is a temporal harmonic balance procedure, can be calculated by the FFT. For $\eta_n(x) = \cos[(n-1)\pi x]$, Eq. (91) can be

expressed by $\tilde{\Gamma} = \tilde{\mathbf{H}}_c^{\mathrm{T}} \mathbf{C}_c \tilde{\Phi}$, where

$$\tilde{\mathbf{H}}_c = \begin{Bmatrix} \cos(0\pi\frac{1}{N_S}) & \cdots & \cos[(N-1)\pi\frac{1}{N_S}] \\ \vdots & \ddots & \vdots \\ \cos(0\pi\frac{N_S-1}{N_S}) & \cdots & \cos[(N-1)\pi\frac{N_S-1}{N_S}] \end{Bmatrix} \tag{96}$$

and $\mathbf{C}_c$ is a coefficient matrix that can be obtained by

$$\mathbf{C}_c = \frac{1}{\pi} \tilde{\mathbf{H}}_c \tilde{\Gamma} \tilde{\Psi}^{\mathrm{T}} \tag{97}$$

Premultiplication of $\tilde{\Gamma}$ by $2\tilde{\mathbf{H}}_c$, which is a spatial harmonic balance procedure, can be efficiently calculated by the fast DCT. The element of $\mathbf{C}_c$ on the n^{th} row and the $(m+M+1)^{th}$ column is the coefficient c_{nm} of $\phi_m(t)\eta_n(x) = \exp(\mathrm{j}mt)\cos[(n-1)\pi x]$.

c) A periodic $N \times N$ matrix $\mathbf{S}(t)$ with the normalized fundamental frequency can be expressed by

$$\mathbf{S}(t) = \sum_{m=-M}^{M} \exp(\mathrm{j}mt)\mathbf{S}_m = \hat{\Phi}^{\mathrm{T}} \mathbf{S}_T \tag{98}$$

where M is the number of harmonic functions used to describe $\mathbf{S}(t)$, $\hat{\Phi}^{\mathrm{T}} = \Phi^{\mathrm{T}} \otimes \mathbf{E}_N$, $\mathbf{S}_m$ is a $N \times N$ matrix coefficient, and $\mathbf{S}_T = [\mathbf{S}_{-M}^{\mathrm{T}} \ \cdots \ \mathbf{S}_M^{\mathrm{T}}]^{\mathrm{T}}$. A truncated Toeplitz form of $\mathbf{S}(t)$ is

$$\mathbf{S}_{\mathscr{T}} = \begin{bmatrix} \mathbf{S}_0 & \cdots & \mathbf{S}_{-M} & \cdots & \mathbf{0} \\ \vdots & \ddots & \vdots & \ddots & \vdots \\ \mathbf{S}_M & \cdots & \mathbf{S}_0 & \cdots & \mathbf{S}_{-M} \\ \vdots & \ddots & \vdots & \ddots & \vdots \\ \mathbf{0} & \cdots & \mathbf{S}_M & \cdots & \mathbf{S}_0 \end{bmatrix} \tag{99}$$

An arbitrary $N \times 1$ column vector $\xi(t)$ with the normalized fundamental frequency can be expressed by

$$\xi(t) = \sum_{m=-M}^{M} \exp(\mathrm{j}mt)\xi_m = \hat{\Phi}^{\mathrm{T}}\xi_T \tag{100}$$

where $\xi_T = [\xi_{-M}^{\mathrm{T}} \ \cdots \ \xi_M^{\mathrm{T}}]^{\mathrm{T}}$. Due to the property of Toeplitz transform [74], and using Eqs. (98) and (100), one has

$$\int_0^{2\pi} \frac{\mathrm{d}t}{\pi} \hat{\Psi}\hat{\Phi}^{\mathrm{T}}\mathbf{S}_T\hat{\Phi}^{\mathrm{T}}\xi_T = \int_0^{2\pi} \frac{\mathrm{d}t}{\pi} \hat{\Psi}\mathbf{S}(t)\xi(t) = \mathbf{S}_{\mathscr{J}}\xi_T \tag{101}$$

where $\hat{\Psi} = \Psi \otimes \mathbf{E}_N$ and $\Psi = \{\phi_M(t) \ \cdots \ \phi_{-M}(t)\}^{\mathrm{T}}$ is the complex conjugate of Φ. Since ξ_T is arbitrary, one can conclude

$$\int_0^{2\pi} \frac{\mathrm{d}t}{\pi} \hat{\Psi}\hat{\Phi}^{\mathrm{T}}\mathbf{S}_T\hat{\Phi}^{\mathrm{T}} = \mathbf{S}_{\mathscr{J}} \tag{102}$$

3.3.3 The STHB Method for a Fixed-Fixed String with Nonlinearity

The govening equation of a fixed-fixed string with geometric nonlinearity in the normalized spatial and temporal coordinates is [77]

$$\omega^2 w_{tt} + \omega c_d w_t - w_{xx} - k_d w_x^2 w_{xx} - y_0 \sin(\pi x)\cos t = 0 \tag{103}$$

where $w(x,t)$ is the transverse displacement of the string, $y_0 \sin(\pi x)\cos t$ is the external excitation, ω is the angular excitation frequency before normalization, c_d

is the damping coefficient, and k_d is the nonlinear stiffness coefficient. Boundary conditions of the string are

$$w(0,t) = w(1,t) = 0 \tag{104}$$

For this type of boundary conditions, a set of trial functions of $w(x,t)$ can be $\mathbf{H}_s = \{\eta_1(x) \ \cdots \ \eta_N(x)\}^{\mathrm{T}}$ with $\eta_n(x) = \sin(n\pi x)$, and a solution of $w(x,t)$ is

$$w(x,t) = \sum_{n=1}^{N} q_n(t)\eta_n(x) = \mathbf{H}_s^{\mathrm{T}}\mathbf{Q} \tag{105}$$

where $\mathbf{Q} = \{q_1(t) \ \cdots \ q_N(t)\}^{\mathrm{T}}$ is a set of generalized coordinates. The first and second partial derivatives of $w(x,t)$ with respective to x are

$$w_x(x,t) = (\mathbf{G}\mathbf{H}_s)^{\mathrm{T}}\mathbf{Q} \tag{106}$$

$$w_{xx}(x,t) = (\mathbf{G}_2\mathbf{H}_s)^{\mathrm{T}}\mathbf{Q} = \mathbf{H}_s^{\mathrm{T}}\mathbf{G}_2\mathbf{Q} \tag{107}$$

respectively, where $\mathbf{G}\mathbf{H} = \{\pi\cos(\pi x) \ \cdots \ N\pi\cos(N\pi x)\}^{\mathrm{T}}$ with $\mathbf{G}$ being the first-order differential operator of $\mathbf{H}_s$, and $\mathbf{G}_2$ is the second-order differential operator of $\mathbf{H}_s$, which is a diagonal matrix with diagonal elements being $\{-\pi^2 \ \cdots \ -N^2\pi^2\}$. Substituting Eqs. (105)-(107) into Eq. (103) yields

$$\omega^2\mathbf{H}_s^{\mathrm{T}}\ddot{\mathbf{Q}} + \omega c_d\mathbf{H}_s^{\mathrm{T}}\dot{\mathbf{Q}} - \mathbf{H}_s^{\mathrm{T}}\mathbf{G}_2\mathbf{Q} - k_d[(\mathbf{G}\mathbf{H}_s)^{\mathrm{T}}\mathbf{Q}]^2(\mathbf{H}_s^{\mathrm{T}}\mathbf{G}_2\mathbf{Q}) - \mathbf{H}_s^{\mathrm{T}}\mathbf{f} = 0 \tag{108}$$

where the single and double overdots denotes the first and second time derivatives, and $\mathbf{f} = \{y_0\cos t \ 0 \ \cdots \ 0\}^{\mathrm{T}}$ is a $N \times 1$ column vector. Conducting a spatial harmonic

balance procedure for Eq. (108) by premultiplying $2\mathbf{H}_s$ on it and integrating the resultant equation from 0 to 1 yields an associated set of ODEs of Eq. (103)

$$\omega^2\ddot{\mathbf{Q}} + \omega c_d\dot{\mathbf{Q}} - \mathbf{G}_2\mathbf{Q} - \mathscr{L}(\mathbf{Q}) - \mathbf{f} = \mathbf{0}_N \tag{109}$$

where

$$\mathscr{L}(\mathbf{Q}) = 2\int_0^1 dx\mathbf{H}_s k_d[(\mathbf{G}\mathbf{H}_s)^{\mathrm{T}}\mathbf{Q}]^2(\mathbf{H}_s^{\mathrm{T}}\mathbf{G}_2\mathbf{Q}) \tag{110}$$

is a nonlinear function of $\mathbf{Q}$, and $\mathbf{0}_N$ is a $N\times 1$ zero vector.

For calculation of periodic solutions of $\mathbf{Q}$, the n^{th} element of $\mathbf{Q}$ can be expressed as a superposition of basis functions of Fourier series: $q_n(t) = \sum_{m=-M}^{M} a_{n,m}\phi_m(t)$, where $a_{n,m}$ is a constant coefficient of $\phi_m(t)$. By defining $\mathbf{a}_m = \{a_{1m}\ \cdots\ a_{Nm}\}^{\mathrm{T}}$, concise expressions of $\mathbf{Q}$, $\dot{\mathbf{Q}}$, and $\ddot{\mathbf{Q}}$ are

$$\mathbf{Q} = \hat{\Phi}^{\mathrm{T}}\mathbf{a} \tag{111}$$

$$\dot{\mathbf{Q}} = \hat{\Phi}^{\mathrm{T}}\hat{\mathbf{D}}\mathbf{a} \tag{112}$$

$$\ddot{\mathbf{Q}} = \hat{\Phi}^{\mathrm{T}}\hat{\mathbf{D}}^2\mathbf{a} \tag{113}$$

respectively, where $\mathbf{a} = \{\mathbf{a}_{-M}^{\mathrm{T}}\ \cdots\ \mathbf{a}_M^{\mathrm{T}}\}^{\mathrm{T}}$, $\hat{\mathbf{D}} = \mathbf{D}\otimes\mathbf{E}_N$, and $\mathbf{D}$ is the first-order differential operator of Φ, which is a diagonal matrix with diagonal elements being $\{-\mathrm{j}M\ \cdots\ \mathrm{j}M\}$. Substituting Eqs. (111-113) into Eq. (109) and conducting a temproal harmonic balance procedure for the resultant equation by premultiplying $\frac{1}{2\pi}\hat{\Psi}$ on it and integrating the resultant equation from 0 to 2π yield an associated set of

algebraic equations of Eq. (103)

$$\omega^2\hat{\mathbf{D}}^2\mathbf{a}+\omega c_d\hat{\mathbf{D}}\mathbf{a}-\hat{\mathbf{G}}_2\mathbf{a}-\mathbf{L}(\mathbf{a})-\hat{\mathbf{f}}=\mathbf{0}_{(2M+1)N} \tag{114}$$

where $\hat{\mathbf{G}}_2=\mathbf{E}_{2M+1}\otimes\mathbf{G}_2$ is derived from $\int_0^{2\pi}\frac{dt}{2\pi}\hat{\Psi}\mathbf{G}_2\mathbf{Q}$ using Eq. (88) with $\mathbf{M}=\mathbf{G}_2$ and $\mathbf{p}=\Phi$, $\mathbf{L}(\mathbf{a})=\int_0^{2\pi}\frac{dt}{2\pi}\hat{\Psi}\mathscr{L}(\mathbf{Q})$ is a nonlinear matrix-valued function, $\hat{\mathbf{f}}=\int_0^{2\pi}\frac{dt}{2\pi}\hat{\Psi}\mathbf{f}$, and $\mathbf{0}_{(2M+1)N}$ is a $(2M+1)N\times 1$ zero vector. If the string is linear with $k_d=0$, the solution of Eq. (114) with vanishing $\mathbf{L}(\mathbf{a})$ is $\mathbf{a}=\mathbf{J}_{\text{lin}}^{-1}\hat{\mathbf{f}}$, where the superscript -1 denotes the inverse of a square matrix, and

$$\mathbf{J}_{\text{lin}}=\omega^2\hat{\mathbf{D}}^2+\omega c_d\hat{\mathbf{D}}-\hat{\mathbf{G}}_2 \tag{115}$$

is Jacobian matrix of the linear string, which is a diagonal matrix. For Eq. (114) with the nonlinear term, Newton-Raphson method can be used to find its solutions. With a guess solution $\mathbf{a}$, the residual of Eq. (114) is

$$\mathbf{R}(\mathbf{a})=\mathbf{J}_{\text{lin}}\mathbf{a}-\mathbf{L}(\mathbf{a})-\hat{\mathbf{f}} \tag{116}$$

The nonlinear term $\mathbf{L}(\mathbf{a})$ is

$$\mathbf{L}(\mathbf{a})=\int_0^{2\pi}\frac{dt}{\pi}\int_0^1 dx\hat{\Psi}\mathbf{H}_s k_d\hat{w}_x^2(\mathbf{a})\hat{w}_{xx}(\mathbf{a}) \tag{117}$$

where $\hat{w}_x(\mathbf{a})=(\mathbf{G}\mathbf{H}_s)^{\mathrm{T}}\hat{\Phi}^{\mathrm{T}}\mathbf{a}$ and $\hat{w}_{xx}(\mathbf{a})=\mathbf{H}_s^{\mathrm{T}}\mathbf{G}_2\hat{\Phi}^{\mathrm{T}}\mathbf{a}$. Let $\Gamma(x,t)=k_d\hat{w}_x^2(\mathbf{a})\hat{w}_{xx}(\mathbf{a})$,

which can be expressed as

$$\Gamma(x,t) = \mathbf{H}_s^{\mathrm{T}}\hat{\Phi}^{\mathrm{T}}\beta = \sum_{n=1}^{N}\sum_{m=-M}^{M} b_{nm}\exp(\mathrm{j}mt)\sin(n\pi x) \tag{118}$$

where $\beta = \{\mathbf{b}_{-M}^{\mathrm{T}} \cdots \mathbf{b}_{M}^{\mathrm{T}}\}^{\mathrm{T}}$ and $\mathbf{b}_m = \{b_{1m} \cdots b_{Nm}\}^{\mathrm{T}}$. By constructing $\tilde{\Gamma}$ for $\Gamma(x,t)$ using Eq. (91), the coefficient matrix $\mathbf{C}_s$ can be calculated using Eq. (94), whose element on the n^{th} row and the $(m+M+1)^{th}$ column is the coefficient b_{nm}, and β can be constructed by b_{nm}. Substituting Eq. (118) into Eq. (117) yields $\mathbf{L}(\mathbf{a}) = \beta$. Thus the residual $\mathbf{R}(\mathbf{a})$ can be obtained.

Jacobian matrix of $\mathbf{R}(\mathbf{a})$ is $\mathbf{J}(\mathbf{a}) = \mathbf{J}_{\mathrm{lin}} - \frac{\partial \mathbf{L}}{\partial \mathbf{a}}$, and

$$\frac{\partial \mathbf{L}}{\partial \mathbf{a}} = \int_0^{2\pi}\frac{dt}{\pi}\int_0^1 dx\hat{\Psi}\mathbf{H}_s(\Gamma_1\frac{\partial \hat{w}_x}{\partial \mathbf{a}} + \Gamma_2\frac{\partial \hat{w}_{xx}}{\partial \mathbf{a}}) \tag{119}$$

where $\Gamma_1 = \frac{\partial \Gamma}{\partial \hat{w}_x} = 2k_d\hat{w}_x\hat{w}_{xx}$, $\Gamma_2 = \frac{\partial \Gamma}{\partial \hat{w}_{xx}} = k_d\hat{w}_x^2$, $\frac{\partial \hat{w}_x}{\partial \mathbf{a}} = (\mathbf{G}\mathbf{H}_s)^{\mathrm{T}}\hat{\Phi}^{\mathrm{T}}$, and $\frac{\partial \hat{w}_{xx}}{\partial \mathbf{a}} = \mathbf{H}_s^{\mathrm{T}}\mathbf{G}_2\hat{\Phi}^{\mathrm{T}}$. By assuming $\Gamma_1 = \mathbf{H}_s^{\mathrm{T}}\hat{\Phi}^{\mathrm{T}}\beta_1$ and $\Gamma_2 = \mathbf{H}_c^{\mathrm{T}}\hat{\Phi}^{\mathrm{T}}\beta_2$, where β_1 and β_2 can be obtained by constructing $\tilde{\Gamma}_1$ and $\tilde{\Gamma}_2$ for Γ_1 and Γ_2 using Eq. (91) and calculating coefficient matrices $\mathbf{C}_s$ and $\mathbf{C}_c$ using Eqs. (94) and (97), respectively, Eq. (119) can be written as

$$\frac{\partial \mathbf{L}}{\partial \mathbf{a}} = \int_0^{2\pi}\frac{dt}{2\pi}\hat{\Psi}[\int_0^1 2dx\mathbf{H}_s\mathbf{H}_s^{\mathrm{T}}\hat{\Phi}^{\mathrm{T}}\beta_1(\mathbf{G}\mathbf{H}_s)^{\mathrm{T}} + \int_0^1 2dx\mathbf{H}_s\mathbf{H}_c^{\mathrm{T}}\hat{\Phi}^{\mathrm{T}}\beta_2\mathbf{H}_s^{\mathrm{T}}\mathbf{G}_2]\hat{\Phi}^{\mathrm{T}} \tag{120}$$

By the derivation in **Appendix A**, Eq. (120) can be rewritten as

$$\frac{\partial \mathbf{L}}{\partial \mathbf{a}} = \int_0^{2\pi}\frac{dt}{2\pi}\hat{\Psi}\hat{\Phi}^{\mathrm{T}}[(\mathbf{E}_{2M+1}\otimes\mathbf{M}_1)\hat{\beta}_1 + (\mathbf{E}_{2M+1}\otimes\mathbf{M}_2)\hat{\beta}_2\mathbf{G}_2]\hat{\Phi}^{\mathrm{T}} \tag{121}$$

where $\hat{\beta}_1 = \beta_1 \otimes \mathbf{E}_N$, $\hat{\beta}_2 = \beta_2 \otimes \mathbf{E}_N$, $\mathbf{M}_1 = \int_0^1 2dx \mathbf{H}_s \mathbf{H}_s^{\mathrm{T}} \otimes (\mathbf{G}\mathbf{H}_s)^{\mathrm{T}}$ and $\mathbf{M}_2 = \int_0^1 2dx \mathbf{H}_s \mathbf{H}_c^{\mathrm{T}} \otimes \mathbf{H}_s^{\mathrm{T}}$ are constant matrices, whose elements on the k^{th} row and the $[N(i-1)+j]^{th}$ column are

$$m_{k,N(i-1)+j} = [\delta(i+j-k) + \delta(|i-j|-k)\mathrm{sgn}(i-j)]/2 \tag{122}$$

$$\mu_{k,N(i-1)+j} = [\delta(i+j-k-1) + \delta(|i-1-j|-k)\mathrm{sgn}(j-i+1)]/2 \tag{123}$$

respectively, with $i,\ j \in \{1\ \cdots\ N\}$, $\delta(x)$ is Dirac delta function, and $\mathrm{sgn}(x)$ is the sign function. Using the property of Toeplitz transform in Eq. (102) for Eq. (121) yields

$$\frac{\partial \mathbf{L}}{\partial \mathbf{a}} = \int_0^{2\pi} \frac{\mathrm{d}t}{\pi} \hat{\Psi}\hat{\Phi}^{\mathrm{T}} \mathbf{S}_T \hat{\Phi}^{\mathrm{T}} = \mathbf{S}_{\mathscr{T}} \tag{124}$$

where

$$\mathbf{S}_T = (\mathbf{E}_{2M+1} \otimes \mathbf{M}_1)\hat{\beta}_1 + (\mathbf{E}_{2M+1} \otimes \mathbf{M}_2)\hat{\beta}_2 \mathbf{G}_2 \tag{125}$$

and $\mathbf{S}_{\mathscr{T}}$ is a truncated Toeplitz form of $\mathbf{S}(t) = \hat{\Phi}^{\mathrm{T}} \mathbf{S}_T$ shown in Eq. (99). Jacobian matrix of $\mathbf{R}(\mathbf{a})$ can be explicitly calculated by $\mathbf{J}(\mathbf{a}) = \mathbf{J}_{\mathrm{lin}} - \mathbf{S}_{\mathscr{T}}$. The guess solution $\mathbf{a}$ of Eq. (114) can be updated by Newton-Raphson method to search a final solution. The algorithm to obtain a periodic solution of Eq. (103) can be automatically and efficiently implemented by a computer program, and it is summarized below.

a1 Choose N, M, N_s and M_s, and construct $\hat{\mathbf{D}}$, $\hat{\mathbf{G}}_2$ and $\mathbf{M}_1$ by Eq. (122) and $\mathbf{M}_2$ by Eq. (123).

a2 For the PDE in Eq. (103) with a guess solution $\mathbf{a}$, calculate the spatial and temporal harmonic balanced residual $\mathbf{L}(\mathbf{a}) = \beta$ for the nonlinear term $\Gamma(x,t) = k_d \hat{w}_x^2(\mathbf{a}) \hat{w}_{xx}(\mathbf{a})$ by constructing $\tilde{\Gamma}$ using Eq. (91) and calculating the coefficient

matrix by Eq. (94).

a3 Calculate spatial and temporal harmonic balanced partial derivatives β_1 and β_2 for $\Gamma_1 = \frac{\partial \Gamma}{\partial \hat{w}_x}$ and $\Gamma_2 = \frac{\partial \Gamma}{\partial \hat{w}_{xx}}$ of the nonlinear term $\Gamma(x,t)$ using the procedure in **a2** with $\Gamma(x,t)$ replaced by Γ_1 and Γ_2, respectively.

a4 Construct the truncated Toeplitz form $\mathbf{S}_{\mathscr{T}}$ of $\mathbf{S}(t) = \hat{\Phi}^{\mathrm{T}}\mathbf{S}_T$ with $\mathbf{S}_T$ given by Eq. (125).

a5 Calculate the residual $\mathbf{R}(\mathbf{a})$ by Eq. (116), where $\mathbf{J}_{\mathrm{lin}}$ is given by Eq. (115) and $\hat{\mathbf{f}}$ is calculated by the FFT.

a6 Calculate Jacobian matrix $\mathbf{J}(\mathbf{a}) = \mathbf{J}_{\mathrm{lin}} - \mathbf{S}_{\mathscr{T}}$, and update $\mathbf{a}$ by Newton-Raphson method.

a7 Reconstruct the periodic solution $w(x,t) = \mathbf{H}_s^{\mathrm{T}}\hat{\Phi}^{\mathrm{T}}\mathbf{a}$ when a final $\mathbf{a}$ is obtained.

3.3.4 Stability Analysis of Periodic Responses and Results

If a periodic solution $\mathbf{Q}_{ss} = \hat{\Phi}^{\mathrm{T}}\mathbf{a}_{ss}$ for the ODEs in Eq. (109) is calculated by a solution $\mathbf{a}_{ss}$ of Eq. (114), a periodic solution of $w(x,t)$ for the PDE in Eq. (103) is obtained. Stability of the solution can be analyzed through a state-space form of a set of linearized equations of Eq. (109) around $\mathbf{Q}_{ss}$:

$$\dot{\gamma} = \mathbf{A}(t)\gamma \tag{126}$$

where $\gamma = \{\delta\mathbf{Q}^{\mathrm{T}}, \delta\dot{\mathbf{Q}}^{\mathrm{T}}\}^{\mathrm{T}}$ is a state vector of pertubation of $\mathbf{Q}_{ss}$ and $\dot{\mathbf{Q}}_{ss}$, the system matrix

$$\mathbf{A}(t) = \begin{Bmatrix} \mathbf{0}_N & \mathbf{E}_N \\ \frac{1}{\omega^2}(\mathbf{G}_2 + \frac{\partial \mathscr{L}}{\partial \mathbf{Q}}) & -\frac{c_d}{\omega}\mathbf{E}_N \end{Bmatrix} \tag{127}$$

is a periodic matrix-valued function, and

$$\frac{\partial \mathscr{L}}{\partial \mathbf{Q}} = 2\int_0^1 dx \mathbf{H}_s(\Gamma_1 \frac{\partial \hat{w}_x}{\partial \mathbf{Q}} + \Gamma_2 \frac{\partial \hat{w}_{xx}}{\partial \mathbf{Q}}) \tag{128}$$

Since $\frac{\partial \hat{w}_x}{\partial \mathbf{a}} = \frac{\partial \hat{w}_x}{\partial \mathbf{Q}}\hat{\mathbf{\Phi}}^{\mathrm{T}}$ and $\frac{\partial \hat{w}_{xx}}{\partial \mathbf{a}} = \frac{\partial \hat{w}_{xx}}{\partial \mathbf{Q}}\hat{\mathbf{\Phi}}^{\mathrm{T}}$, Eq. (119) can be written as

$$\frac{\partial \mathbf{L}}{\partial \mathbf{a}} = \int_0^{2\pi} \frac{dt}{2\pi}\hat{\mathbf{\Psi}}\frac{\partial \mathscr{L}}{\partial \mathbf{Q}}\hat{\mathbf{\Phi}}^{\mathrm{T}} \tag{129}$$

Comparing Eqs. (129) and (124) yields $\frac{\partial \mathscr{L}}{\partial \mathbf{Q}} = \hat{\mathbf{\Phi}}^{\mathrm{T}}\mathbf{S}_T = \mathbf{S}(t)$. Note that $\mathbf{E}_N$ and $\mathbf{G}_2$ are constant matrices. A truncated Toeplitz form of $\mathbf{A}(t)$, denoted by $\mathbf{A}_{\mathscr{T}}$, has the same form as Eq. (99), whose diagonal block is

$$\mathbf{A}_0 = \begin{Bmatrix} \mathbf{0}_N & \mathbf{E}_N \\ \frac{1}{\omega^2}\mathbf{G}_2 & -\frac{c_d}{\omega}\mathbf{E}_N \end{Bmatrix} + \begin{Bmatrix} \mathbf{0}_N & \mathbf{0}_N \\ \frac{1}{\omega^2}\mathbf{S}_0 & \mathbf{0}_N \end{Bmatrix} \tag{130}$$

and off-diagonal blocks are

$$\mathbf{A}_m = \begin{Bmatrix} \mathbf{0}_N & \mathbf{0}_N \\ \frac{1}{\omega^2}\mathbf{S}_m & \mathbf{0}_N \end{Bmatrix},\ m \in \{-M\ \cdots -1, 1 \cdots M\} \tag{131}$$

where $\mathbf{S}_m$ is the coefficient matrix of $\mathbf{S}(t)$, which can be directly obtained from $\mathbf{S}_T$. Thus $\mathbf{A}_{\mathscr{T}}$ can be constructed from Jacobian matrix $\mathbf{J}(\mathbf{a})$. The complex plane can be divided into inifinte strips $\left(\mathrm{j}(2k-1)\pi,\ \mathrm{j}(2k+1)\pi\right]$ with the integer $k \in (-\infty, +\infty)$, and locations of eigenvalues of $\mathbf{A}_{\mathscr{T}}$ are repeated in every strip. Eigenvalues $\lambda = [\lambda_1\ \cdots\ \lambda_N]$ in the fundamental strip $(-\mathrm{j}\pi,\ \mathrm{j}\pi]$ are used to analyze stability of Eq. (126). If all values of $\exp(2\pi\lambda_n)$ with $n \in \{1\ \cdots\ N\}$ are inside the unit circle,

the solution $\mathbf{Q}_{ss}$ is stable; otherwise, it is unstable. Furthermore, in an unstable case, if there are values of $\exp(2\pi\lambda_n)$ less than -1, there occurs a period-doubling bifurcation; if there are values of $\exp(2\pi\lambda_n)$ that are complex, a Hopf bifurcation occurs.

Some parameters in Eq. (103) are chosen as $c_d = 0.8$, $y_0 = 0.5$, $M = 19$, $N_s = 64$ and $M_s = 128$ for simulation purposes. For weak geometric nonlinearity, $k_d = 10$ is used, and for strong geometric nonlinearity, $k_d = 30$ is used. Frequency-response curves of the string for weak and strong nonlinearities are shown in Figs. 34 and 35, respectively, where the ordinate is Euclidean norm of $\mathbf{a}$, and $N = 5$ and 10 are numbers of spatial basis functions used for the two cases. For both cases, curves obtained from $N = 5$ and 10 are almost overlapped, which show convergence of results. In the case of weak nonlinearity, all periodic solutions are stable. In the case of strong nonlinearity, there are unstable solutions, but no period-doubling or Hopf bifurcation occurs. Unstable solutions for $N = 5$ are shown in Fig. 35.

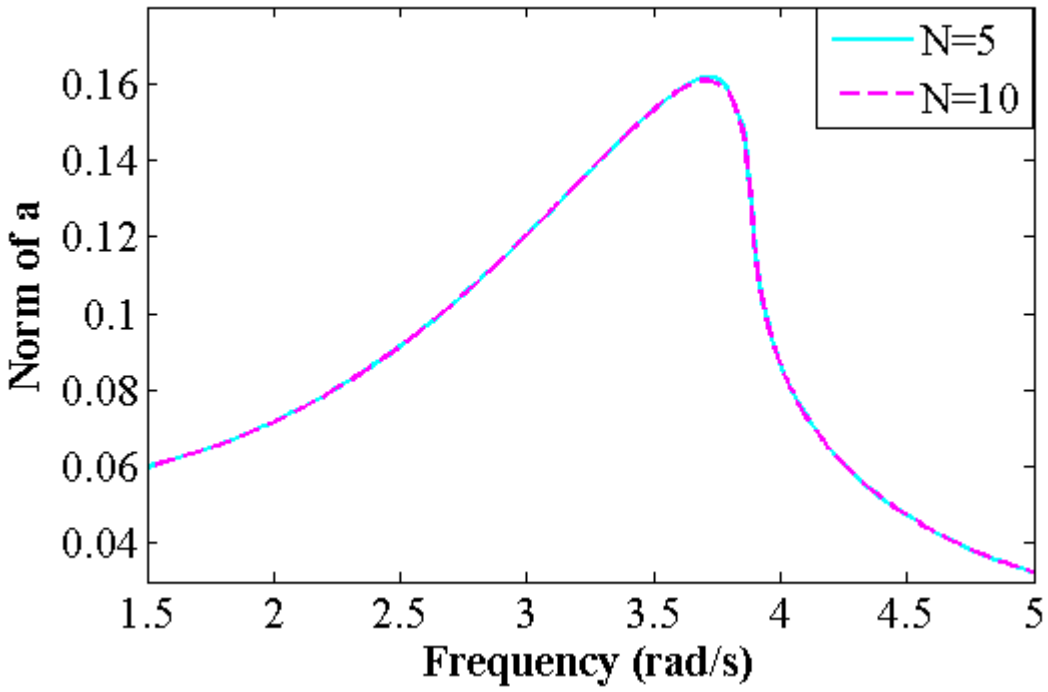

Figure 34: Frequency-response curves for the case of weak nonlinearity with $k_d = 10$; $N = 5$ and 10

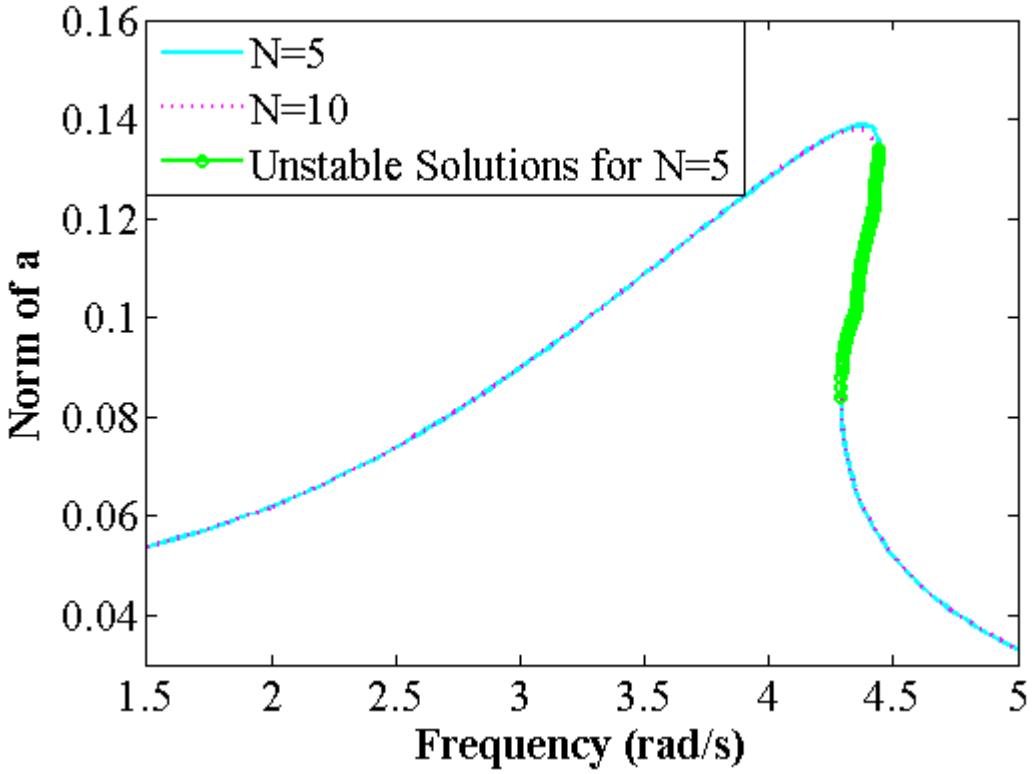

Figure 35: Frequency-response curves for the case of strong nonlinearity with $k_d = 30$; $N = 5$ and 10. Unstable solutions for $N = 5$ are indicated.

3.3.5 The STHB Method for a String with Complex Boundary Condition

Consider a string with its governing equation in Eq. (103). There are a fixed boundary condition and a complex boundary condition with a spring at the boundary:

$$w(0,t) = 0, \quad k_0 w(1,t) = w_x(1,t) \tag{132}$$

where k_0 is the stiffness of the spring. A set of trial functions of $w(x,t)$ in the spectral Tau method are $\{\mathbf{H}_s^{\mathrm{T}}\ e(x)\}^{\mathrm{T}}$, where $e(x)=x$, and a set of test functions are $\mathbf{H}_{s\_1}=\{\eta_1(x)\ \cdots\ \eta_{N+1}(x)\}^{\mathrm{T}}$. A solution of $w(x,t)$ can be

$$w(x,t)=\mathbf{H}_s^{\mathrm{T}}\mathbf{Q}+e(x)q_{N+1} \tag{133}$$

where $q_{N+1}=\sum_{m=-M}^{M}a_{N+1,m}\phi_m(t)=\Phi^{\mathrm{T}}\mathbf{a}_e$. With substitution of Eq. (133) into Eq. (132), the fixed boundary condition $w(0,t)=0$ is automatically satisfied, and the equation for the boundary with the spring becomes

$$k_0[(\mathbf{H}_s^{\mathrm{T}}|_{x=1})\mathbf{Q}+q_{N+1}]-\left((\mathbf{G}\mathbf{H}_s)^{\mathrm{T}}|_{x=1}\right)\mathbf{Q}-q_{N+1}=0 \tag{134}$$

where $(\cdot|_{x=1})$ denotes evaluation of a function at $x=1$. Substituting Eq. (133) into the left-hand side of Eq. (103) yields

$$\begin{aligned}\mathscr{O}(\mathbf{a},\mathbf{a}_e)=&\ \omega^2\mathbf{H}_s^{\mathrm{T}}\ddot{\mathbf{Q}}+\omega c_d\mathbf{H}_s^{\mathrm{T}}\dot{\mathbf{Q}}-\mathbf{H}_s^{\mathrm{T}}\mathbf{G}_2\mathbf{Q}-k_d[(\mathbf{G}\mathbf{H}_s)^{\mathrm{T}}\mathbf{Q}+q_{N+1}]^2(\mathbf{H}_s^{\mathrm{T}}\mathbf{G}_2\mathbf{Q})\\&-\mathbf{H}_s^{\mathrm{T}}\mathbf{f}+\omega^2e(x)\ddot{q}_{N+1}+\omega c_d e(x)\dot{q}_{N+1}\end{aligned} \tag{135}$$

where $\ddot{\mathbf{Q}}$, $\dot{\mathbf{Q}}$, and $\mathbf{Q}$ are given in Eqs. (111)-(113), $\dot{q}_{N+1}=\Phi^{\mathrm{T}}\mathbf{D}\mathbf{a}_e$, and $\ddot{q}_{N+1}=\Phi^{\mathrm{T}}\mathbf{D}^2\mathbf{a}_e$. The spatial and temporal harmonic balanced residual of Eq. (135) is

$$\mathbf{O}(\mathbf{a},\mathbf{a}_e)=\int_0^{2\pi}\frac{dt}{\pi}\int_0^1 dx\hat{\Psi}\mathbf{H}_s\mathscr{O}(\mathbf{a},\mathbf{a}_e) \tag{136}$$

Similar to Eq. (117),$\Gamma(x,t)=\mathscr{O}(\mathbf{a},\mathbf{a}_e)$ can be expressed as $\Gamma(x,t)=\mathbf{H}_s^{\mathrm{T}}\hat{\Phi}^{\mathrm{T}}\beta_e$, where β_e is calculated using Eqs. (91) and (94). Thus the residual $\mathbf{O}(\mathbf{a},\mathbf{a}_e)=\beta_e$ can

be obtained by substituting $\Gamma(x,t) = \mathbf{H}_s^{\mathrm{T}}\hat{\Phi}^{\mathrm{T}}\beta_e$ into Eq. (136). Broyden's method [32] that is a quasi-Newton method can be used to find $\mathbf{a}$ and $\mathbf{a}_e$ to make β_e vanish. Parameters of the string in numerical simulation are the same as those in Sec. 3.2 for the case of weak nonlinearity, except for the spring stiffness k_0. If k_0 is very large such as $k_0 = 10000$, the frequency-response curve of the string with the complex boundary condition is almost the same as that with fixed-fixed boundary conditions, as shown in Fig. 36; if k_0 is small such as $k_0 = 10$, the curve is shifted.

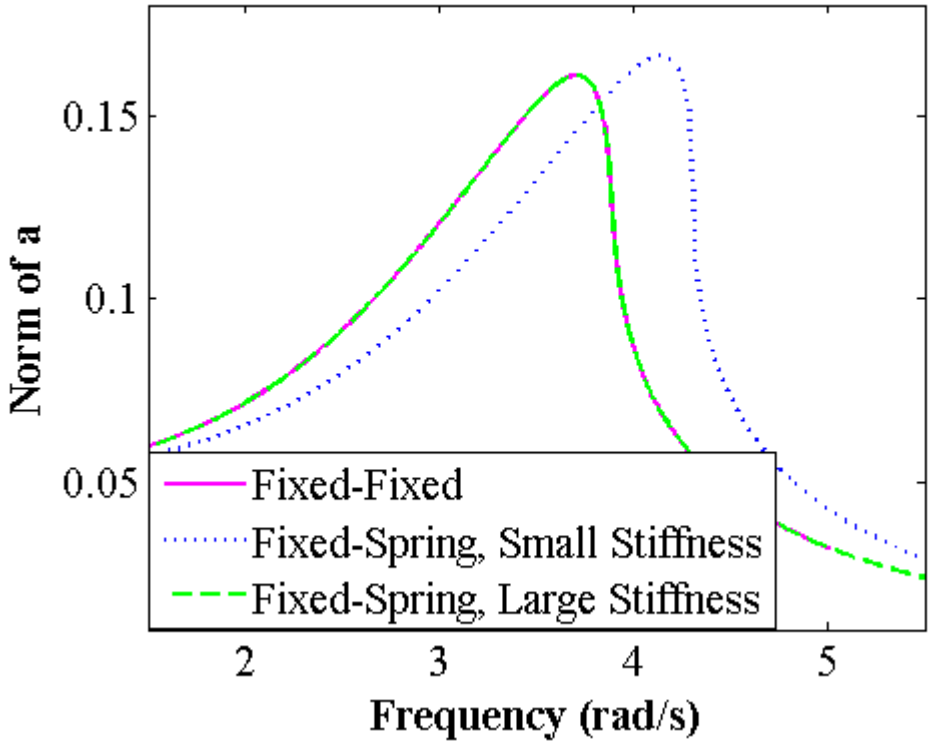

Figure 36: Frequency-response curves for cases of the string with fixed-fixed boundary conditions and fixed-spring bounadry conditions; $k_0 = 10000$ for the large spring stiffness case and $k_0 = 10$ for the small spring stiffness case.

4 Dynamics, Controller Design and Testing of the IVT

4.1 Dynamic Model of the IVT System

In this section, we will introduce a simulation system for the prototype of the IVT, and develop a dynamic model of the system. The simulation system, which is called the IVT system, includes the IVT, a permanent magnetic DC motor as the prime mover of the IVT, a brake as the output load of the IVT, and a stepper motor as the control actuator to adjust the speed ratio of the IVT. The dynamic model of the IVT system is developed for the IVT described in Sec. 2.3. There are some assumptions in deriving the dynamic model of the IVT system: the dynamic effect caused by the control speed ω_c in Eq. (44) is neglected since ω_c is much smaller than the motor speed ω_m or the modulated input speed ω on the driven noncircular gear in Eq. (43); the supply voltage of the DC motor V_m and the output torque from the brake T_U are assumed to be unchanged until a steady state of the IVT is reached; the armature inductance of the DC motor is small and the response time of the armature current is short; and friction in the IVT system is neglected and all components are considered as rigid bodies. There are two subsystems in the IVT system: the permanent magnetic DC motor and the IVT. A dynamic model of the permanent magnetic DC motor is

$$\begin{cases} L_a \dot{i}_a = -R_a i_a - k_e \omega_m + V_m \\ J_{N1} \dot{\omega}_m = k_t i_a - \beta \omega_m - T_m \end{cases} \tag{137}$$

where an overdot denotes time differentiation, and L_a, i_a, R_a, k_e, J_{N1}, k_t, β and T_m are the amature inductance, amature current, amature resistance, velocity constant, moment of inertia of the driving noncircular gear, torque constant, damping coefficient and torque on the driving noncircular gear exerted by the driven noncircular gear, respectively. Considering the assumptions that L_a and β can be neglected and using Eq. (43) in Eq. (137), one has

$$T_m = \frac{k_t}{R_a} V_m - \frac{k_t k_e}{R_a} f\omega - J_{N1} f\dot{\omega} - J_{N1} f_\theta \omega^2 \tag{138}$$

where the subscript θ denotes partial differentiation of a function with respect to θ,

$$f_\theta = \frac{-\pi}{2\sqrt{2}} \sin(\mathrm{mod}(\theta + \frac{\pi}{4}, \frac{\pi}{2}) - \frac{\pi}{4}) \tag{139}$$

is a discontinuous function as shown in Fig. 37, and $\mathrm{mod}(\theta + \frac{\pi}{4}, \frac{\pi}{2})$ gives the remainder on division of $\theta + \frac{\pi}{4}$ by $\frac{\pi}{2}$. The reactive torque on the driven noncircular gear is $-fT_m$.

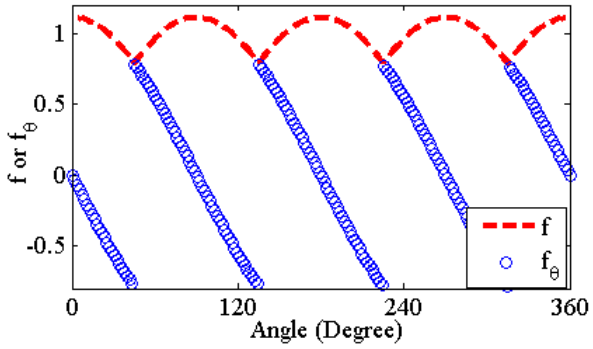

Figure 37: Values of f and f_θ

Lagrange equation is used to derive the dynamic equation of the IVT with the generalized coordinate θ that is the time integration of ω. In the input-control module, since angular speeds of carriers, the input shaft where components of the module are installed, and the driven noncircular gear are all ω, their kinetic energy is

$$T_{w1} = \frac{1}{2}(J_{N2} + J_{\text{carrier}} + J_{\text{inshaft}})\omega^2 \tag{140}$$

where J_{N2}, J_{carrier} and J_{inshaft} are the moments of inertia of the driven noncircular gear, two carriers with planet gears and the input shaft. Since ω_c is much smaller than ω, substituting $\omega_c = 0$ into Eq. (44) yields

$$\omega_{r1} = \omega_{r2} = \frac{2(d_S + d_P)}{d_S + 2d_P}\omega \tag{141}$$

which are proportional to ω and d_s is designed to be equal to d_p. The kinetic energy of two sets of ring gears is

$$T_{w2} = \frac{1}{2}J_{\text{ring}}\frac{4(d_S + d_P)^2}{(d_S + 2d_P)^2}\omega^2 \tag{142}$$

where J_{ring} is the moment of inertia of two sets of ring gears. In the motion-conversion module, angular speeds of crank gears, the crank shaft where crank gears are installed, and rollers are all ω by the specific design of gear ratios, and their kinetic energy is

$$T_{w3} = \frac{1}{2}J_{\text{crk}}\omega^2 \tag{143}$$

where J_{crk} is the moment of inertia of the crank shaft, all crank gears on it, and all rollers with respect to theirs center of mass. Denoting the eccentricity of the

roller is r, the translational speed of the center of mass of rollers is $r\omega$, and their translational kinetic energy is

$$T_{w4} = \frac{1}{2} m_r r^2 \omega^2 \tag{144}$$

where m_r is the mass of all rollers. The speeds of two drivers, v_{d1} and v_{d2}, are given in Eqs. (45) and (46), and the angular speeds of output gears are $\pm v_{di}/r_u$ with $i = 1, 2$. The kinetic energy of drivers and output gears are

$$T_{w5} = \frac{1}{2}[m_d(v_{d1}^2 + v_{d2}^2) + J_u \frac{(v_{d1}^2 + v_{d2}^2)}{r_u^2}] \tag{145}$$

where m_d is the mass of a driver, J_u is the moment of inertia of two output gears, and r_u, as used in Sec. 2.3, is the radius of the output gears. Using Eqs. (45) and (46), we have

$$v_{d1}^2 + v_{d2}^2 = r^2 \omega^2$$

and

$$T_{w5} = \frac{1}{2} m_{\mathrm{dr}} r^2 \omega^2 \tag{146}$$

where

$$m_{\mathrm{dr}} = m_d + \frac{J_u}{r_u^2}$$

From Eq. (47), the kinetic energy of the output shaft and the brake is

$$T_{w6} = \frac{1}{2} J_U \frac{8r^2}{\pi^2 r_u^2} f^2 \omega^2 \tag{147}$$

where J_U is the moment of inertia of the output shaft ad the brake. The kinetic energy can be sorted into three categories:

$$T_a = T_{w1} + T_{w2} + T_{w3} = \frac{1}{2} J_a \omega^2$$

$$T_b = T_{w4} + T_{w5} = \frac{1}{2} J_b r^2 \omega^2$$

and

$$T_c = T_{w6} = \frac{1}{2} J_c f^2 r^2 \omega^2$$

where

$$J_a = J_{N2} + J_{\text{carrier}} + J_{\text{inshaft}} + J_{\text{crk}} + J_{\text{ring}} \frac{4(d_S + d_P)^2}{(d_S + 2d_P)^2}$$

$J_b = m_r + m_{\text{dr}}$ and

$$J_c = J_U \frac{8}{\pi^2 r_u^2}$$

The potential energy of the IVT is that of rollers, which is

$$V_t = m_r g(-\sin\theta + \cos\theta) r \tag{148}$$

The generalized force is

$$Q_t = f T_m - \frac{2\sqrt{2} r}{\pi r_u} f T_U \tag{149}$$

Defining the Lagrangian of the IVT as $L_t = T_a + T_b + T_c - V_t$, using Lagrange equation

$$\frac{d}{dt} \frac{\partial L_t}{\partial \omega} - \frac{\partial L_t}{\partial \theta} = Q_t \tag{150}$$

and substituing Eq. (138) into Eq. (150), one obtains the dynamic equation of the IVT:

$$J(r,\theta)\ddot{\theta} = G(\theta)r - \frac{1}{2}J_\theta(\theta)\dot{\theta}^2 - F_m(\theta)\dot{\theta} + f_1(\theta, V_m) - f_2(\theta, T_U)r \tag{151}$$

where $J = J_a + J_b r^2 + J_c r^2 f^2 + J_d f^2$ is a time-varying moment of inertia of the IVT system, $J_d = J_{N1}$, $J_\theta = 2(J_c r^2 + J_d) f f_\theta$, $G = g(\sin\theta + \cos\theta)$, $F_m = \frac{k_t k_e}{R_a} f^2$, $f_1 = \frac{k_t}{R_a} f V_m$, and $f_2 = \frac{2\sqrt{2} f T_U}{\pi r_u}$. Note that J is positive definite. Values of all parameters of the IVT is listed in Table 1. From the values, we can obtain that $J_a = 0.0237\ \text{kg}\cdot\text{m}^2$, $J_b = 2.1264\ \text{kg}$, $J_c = 0.3388\ \text{kg}$, $F_m = 2.375 f^2$, $f_1 = 3.1667 f V_m$ and $f_2 = 40.5548 f T_U$.

Table 1: Parameters of the IVT

Label	Value	Label	Value
R_a	$0.24\ \Omega$	k_e	$0.75\ \text{V}\cdot\text{s/rad}$
k_t	$0.76\ \text{N}\cdot\text{m/A}$	J_{N1}	$0.002347\ \text{kg}\cdot\text{m}^2$
J_{N2}	$0.002293\ \text{kg}\cdot\text{m}^2$	J_{inshaft}	$0.00002\ \text{kg}\cdot\text{m}^2$
J_{carrier}	$0.001618\ \text{kg}\cdot\text{m}^2$	J_{ring}	$0.00663\ \text{kg}\cdot\text{m}^2$
J_{crk}	$0.007995\ \text{kg}\cdot\text{m}^2$	m_r	$1.16\ \text{kg}$
m_{dr}	$0.9664\ \text{kg}$	J_U	$0.000206\ \text{kg}\cdot\text{m}^2$
r_u	$0.0222\ \text{m}$	g	$9.8\ \text{kg}\cdot\text{m}/s^2$

4.2 Dynamic Analysis of the IVT System for Design of its Open Loop Control

4.2.1 Design of an Open Loop Control using the IHB Method

The dynamic model for the IVT system is a nonlinear second-order ordinary differential equation as shown in Eq. (151). The purpose to develop the dynamic model is to study the dynamic performance of the IVT and then develop a control law for the IVT, so that the prime mover for the IVT can have a good running performance. The performance of a prime mover highly depends on its angular speed. In practice, the average of its output speed over a revolution of its output shaft is usually desired to be some constant to achieve the highest efficiency with a low control effort. here, our goal of the controller of the IVT system is to make the average of the motor speed ω_m over a revolution, which is equal to $\omega = \dot{\theta}$ over 2π in θ, converge to a desired constant ω_0 for any V_m and T_U in their working regions by adjusting the value of r. Working regions of V_m and T_U here are 2 V $\leq V_m \leq$ 12 V and 1.5 Nm $\leq T_U \leq$ 9 Nm, respectively.

The controller studied here includes a feedback control and an open loop control. Design of the open loop control is to find the value of r based on the dynamic equation of the IVT system in Eq. (151), so that the average of the steady-state ω over 2π in θ is equal to ω_0 for any V_m and T_U. The value of r, denoted by $u_{ol}(V_m, T_U; \omega_0)$, should be a function of V_m, T_U and ω_0. When $\omega_0 = 100$ RPM is assumed to be a constant here, $u_{ol}(V_m, T_U)$ is expressed as a function of V_m and T_U. Since changing rates of V_m and T_U are usually much smaller than the speed of the prime mover, V_m and T_U are assumed to be constants before ω converges to its

steady state.

A numerical integral method to find r is to calculate the time response of ω using Eq. (151) with a guess r until it goes to steady state, and then estimate the average of ω over 2π in θ. If the difference of the estimation and ω_0 is less than a tolerance, the desired r is achieved; otherwise, the procedure will be repeated with other guesses of r until the difference is less than the tolerance. Clearly, it is a time-consuming method. Alternatively, the IHB method introduced in Sec. 3, which is aimed to find periodic solution for linear and nonlinear equations, is suitable here. With use of the IHB method, the transient response of ω is skipped, and the desired r to make the average of ω at steady state equal to ω_0 can be found by Newton method.

At the steady state, the angular speed ω is a periodic variable with an average ω_0, and the angle $\theta = \omega_0 t + \theta_1$ is the integration of ω, where θ_1 is a periodic variable with zero mean. To find a solution of $r = u_{ol}(V_m, T_U)$ so that Eq. (151) holds with $\theta = \omega_0 t + \theta_1$, the modified IHB method in [32] can be used here. With use of a dimensionless time variable $\tau_p = \omega_0 t$, one has

$$\theta = \tau_p + \mathbf{C}_s^{\mathrm{T}} \mathbf{q}_p \tag{152}$$

$$\dot{\theta} = \omega_0 \frac{d\theta}{d\tau_p} = \omega_0 (1 + \mathbf{C}_s^{\mathrm{T}} \mathbf{D}_p \mathbf{q}_p) \tag{153}$$

$$\ddot{\theta} = \omega_0^2 \frac{d^2\theta}{d\tau_p^2} = \omega_0^2 \mathbf{C}_s^{\mathrm{T}} \mathbf{D}_p^2 \mathbf{q}_p \tag{154}$$

where a superscript T denotes a transpose of a matrix or a vector, θ_1 is approximated

by a truncated Fourier series $\mathbf{C}_s^{\mathrm{T}}\mathbf{q}_p$, a variable vector

$$\mathbf{q}_p = \{q_{c1} \ \cdots \ q_{cn} \ q_{s1} \ \cdots q_{sn}\}^{\mathrm{T}}$$

is coefficients of the Fourier series,

$$\mathbf{C}_s = \{\cos\tau_p \ \cdots \ \cos n\tau_p \ \sin\tau_p \ \cdots \sin n\tau_p\}^{\mathrm{T}}$$

is a set of truncated bases of the Fourier series, and

$$\mathbf{D}_p = \begin{Bmatrix} \mathbf{0}_n & \mathbf{D}_1 \\ -\mathbf{D}_1 & \mathbf{0}_n \end{Bmatrix}$$

is a differentiation operator for $\mathbf{C}_s$, in which $\mathbf{0}_n$ is a $n \times n$ zero matrix and $\mathbf{D}_1$ is a diagonal matrix with diagonal elements being $\{1 \ \cdots \ n\}$. Given guesses of $\mathbf{q}_p$ and r, substituting Eqs. (152)-(154) into Eq. (151) yields its residual

$$R_p = \omega_0^2[J\mathbf{C}_s^{\mathrm{T}}\mathbf{D}_p^2\mathbf{q}_p + \frac{1}{2}J_\theta(1+\mathbf{C}_s^{\mathrm{T}}\mathbf{D}_p\mathbf{q}_p)^2] + \omega_0 F_m(1+\mathbf{C}_s^{\mathrm{T}}\mathbf{D}_p\mathbf{q}_p) - Gr - f_1 + f_2 r \tag{155}$$

The harmonic balanced residual of R_p is $\mathbf{R}_p = \frac{1}{\pi}\int_0^{2\pi}\tilde{\mathbf{C}}_s R_p d\tau$, where

$$\tilde{\mathbf{C}}_s = \{\frac{1}{2} \ \cos\tau_p \ \cdots \ \cos n\tau_p \ \sin\tau_p \ \cdots \sin n\tau_p\}^{\mathrm{T}}$$

and the integration can be efficiently implemented by the fast Fourier transform [32]. Given a guess of an approximated Jacobian matrix $\mathbf{B}_p$ for the vector-valued function $\mathbf{R}_p$ with respect to the variable vector $\mathbf{x}_p = \{r \ \mathbf{q}_p^{\mathrm{T}}\}^{\mathrm{T}}$, Boyden's method can

be used to update r, $\mathbf{q}_p$ and $\mathbf{B}_p$:

$$\hat{\mathbf{x}}_p = \mathbf{x}_p - \mathbf{B}_p^{-1}\mathbf{R}_p \tag{156}$$

$$\hat{\mathbf{B}}_p = \mathbf{B}_p + \frac{(\mathbf{y}_p - \mathbf{B}_p\mathbf{s}_p)\mathbf{s}_p^{\mathrm{T}}}{\mathbf{s}_p^{\mathrm{T}}\mathbf{s}_p} \tag{157}$$

where a scalar, a vector or a matrix with an overhat denotes its update, $\mathbf{s}_p = \hat{\mathbf{q}}_p - \mathbf{q}_p$, and $\mathbf{y}_p = \hat{\mathbf{R}}_p - \mathbf{R}_p$, in which $\hat{\mathbf{R}}_p$ is the harmonic balanced residual calculated with the updated variable vector $\hat{\mathbf{x}}_p = \{\hat{r}\ \hat{\mathbf{q}}_p^{\mathrm{T}}\}^{\mathrm{T}}$ in Eq. (155). Solutions of $\mathbf{q}_p$ and r, which are denoted by $\bar{\mathbf{q}}_p$ and $\bar{r}$, respectively, are obtained when the Euclidean norm of $\mathbf{R}_p$ is less than a preset tolerance 10^{-10}. The maximal r designed for the IVT is 0.012 m here. In the case that $\bar{r}$ calculated from the modified IHB method for some V_m and T_U is smaller than or equal to 0.012 m, the open loop control value $u_{ol}(V_m, T_U)$ is equal to $\bar{r}$; in the case that $\bar{r}$ calculated for some V_m and T_U is larger than 0.012 m, $u_{ol}(V_m, T_U)$ is set to 0.012 m. In the later case, the average of ω is larger than ω_0, and the IVT system works at an over-drive mode. Values of $\bar{r}$ are calculated when V_m and T_U are chosen for all combinations in $V_m \in \{2\ \ 2.4\ \cdots\ 11.6\ \ 12\}$ and $T_U \in \{1.5\ \ 2\ \cdots\ 8.5\ \ 9\}$, and they are shown in Fig. 38(a); the relation of $\bar{r}$ with V_m

and T_U can be fitted by a polynomial:

$$\begin{aligned} r_f(V_m, T_U) = {} & 3.2 \times 10^{-5} T_U^4 - 2.3 \times 10^{-5} V_m T_U^3 \\ & - 6.65 \times 10^{-4} T_U^3 + 4.7 \times 10^{-4} V_m T_U^2 \\ & + 4.6 \times 10^{-3} T_U^2 - 3.23 \times 10^{-3} V_m T_U \\ & - 2.1 \times 10^{-5} V_m^2 - 1.17 \times 10^{-2} T_U \\ & + 8.85 \times 10^{-3} V_m + 6.43 \times 10^{-3} \end{aligned} \tag{158}$$

The boundary $\bar{r} = 0.012$, which is calculated by $r_f(V_m, T_U) = 0.012$, to distinguish different cases for the open loop control law is shown in Fig. 38(b), and it can be approximated by a linear function of V_m and T_U:

$$f_B(V_m, T_U) = V_m - 1.579 T_U - 0.632 = 0 \tag{159}$$

On the upper left side of the boundary, $\bar{r}$ is larger than 0.012, i.e., $f_B > 0$; on the other side, $\bar{r}$ is smaller than 0.012, i.e., $f_B < 0$. The open loop control law is

$$u_{ol}(V_m, T_U) = \begin{cases} r_f(V_m, T_U), & \text{if } f_B(V_m, T_U) \leq 0 \\ 0.012, & \text{if } f_B(V_m, T_U) > 0 \end{cases} \tag{160}$$

If $f_B \leq 0$, the steady-state solution of ω from the modified IHB method can be expressed as $\bar{\omega} = \omega_0(1 + \mathbf{C}_s^{\mathrm{T}} \mathbf{D}_p \bar{\mathbf{q}}_p)$, and a numerical solution of ω can be calculated from Eq. (151) with the given $\bar{r}$ using Runge-Kutta method. A steady-state solution of ω from the modified IHB method and its numerical solution that approaches steady state are shown in Fig. 39, where $n = 7$, $V_m = 6$ V, $T_U = 6$ Nm and $\bar{r} =$

0.0067 m, and they match well.

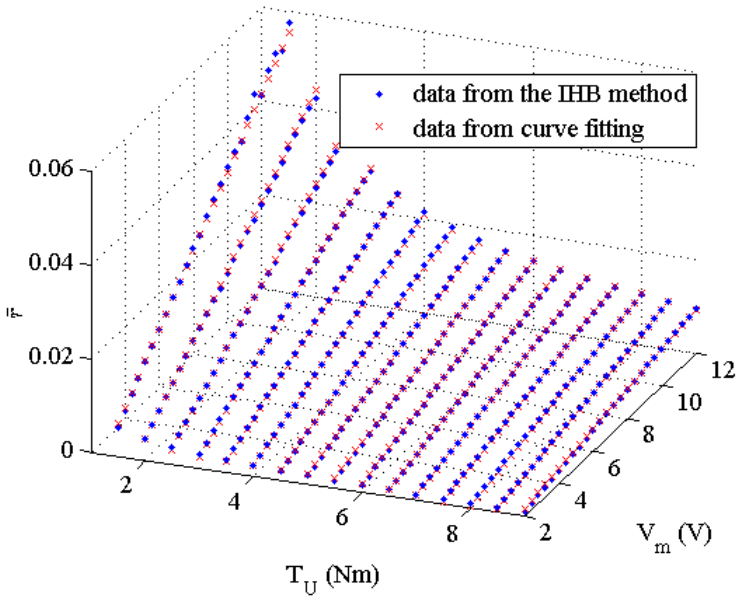

(a)

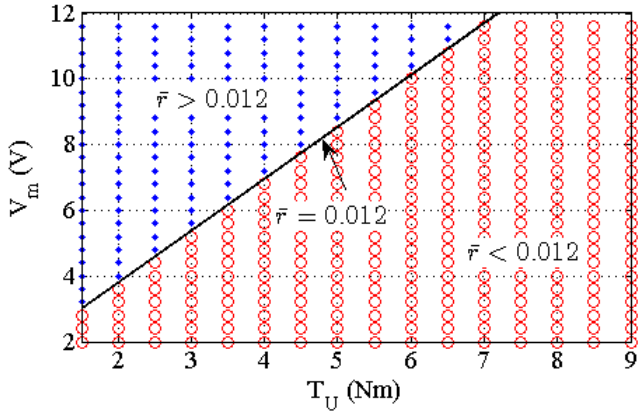

(b)

Figure 38: (a)Values of $\bar{r}$, (b) the boundary $\bar{r} = 0.012$ to distinguish different cases for the open loop control law; $\bar{r} > 0.012$ on the upper left side of the boundary and $\bar{r} < 0.012$ on the other side.

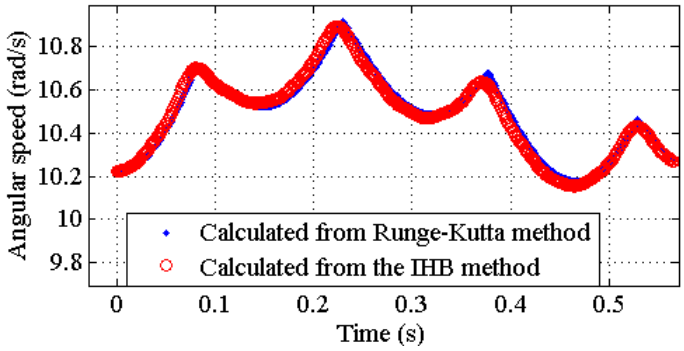

Figure 39: Comparison between steady-state solutions of ω from the modified IHB method and Runge-Kutta method with $V_m = 6$ V, $T_U = 6$ Nm and $\bar{r} = 0.0067$ m

4.2.2 Existence and Convergence of Periodic Solutions for the IVT System

Some analytical properties, such as existence and convergence, of a periodic solution at steady state for Eq. (151) with $r = u_{ol}$ are studied here. A set defined by

$$\Omega_{u1} = \{(V_m, T_U) : \ 2 \leq V_m \leq 12, \ 1.5 \leq T_U \leq 9, \ f_B(V_m, T_U) \leq 0\}$$

is part of working regions of V_m and T_U, where the open loop control value u_{ol} is equal to r_f, and a set defined by

$$\Omega_{u2} = \{(V_m, T_U) : \ 2 \leq V_m \leq 12, \ 1.5 \leq T_U \leq 9, \ f_B(V_m, T_U) > 0\}$$

is the other part of working regions of V_m and T_U, where $u_{ol} = 0.012$. The entire working regions of V_m and T_U are denoted by $\Omega_u = \Omega_{u1} \cup \Omega_{u2}$. There is a proposition to summarize a useful condition for parameters in Eq. (151) with $r = u_{ol}$.

Proposition 1

For Eq. (151) with $r = u_{ol}$, i.e.,

$$J(u_{ol},\theta)\ddot{\theta} = \Gamma - \frac{1}{2}J_\theta(\theta)\dot{\theta}^2 - F_m(\theta)\dot{\theta} \tag{161}$$

where

$$\Gamma = G(\theta)u_{ol} + f_1(\theta, V_m) - f_2(\theta, T_U)u_{ol}$$

its parameters given in Sec. 2.2 ensure that there is a positive number δ_1, s.t. $\Gamma \geq \delta_1$ for all $(V_m,\ T_U) \in \Omega_u$ and $t \in \mathbb{R}^+$.

Proof: Define

$$\hat{\Gamma}(V_m, T_U) = \inf_{t\geq 0}(Gr_f) + (\frac{k_t}{R_a}V_m - \frac{2\sqrt{2}T_U}{\pi r_u}r_f)\inf_{t\geq 0} f$$

Since r_f is non-negative, $\inf_{t\geq 0} G = -9.8\times\sqrt{2}$, and $\inf_{t\geq 0} f = \frac{1}{\sqrt{2}}$, one has

$$\hat{\Gamma}(V_m, T_U) = -(9.8\times\sqrt{2})r_f + \frac{1}{\sqrt{2}}(\frac{k_t}{R_a}V_m - \frac{2\sqrt{2}T_U}{\pi r_u}r_f)$$

Values of $\hat{\Gamma}$ for $(V_m,\ T_U) \in \Omega_u$ are calculated and plotted in Fig. 40, as well as boundaries $\hat{\Gamma} = 0$ and $f_B = 0$. On the upper left side of the boundary $\hat{\Gamma} = 0$, $\hat{\Gamma}$ is smaller than zero; on the other side, $\hat{\Gamma}$ is larger than zero. The boundary $\hat{\Gamma} = 0$ is on the upper left side of $f_B = 0$, i.e., $f_B(V_m, T_U) > 0$, which indicates that there is $\delta_1 > 0$, s.t. $\hat{\Gamma}(V_m, T_U) \geq \delta_1$ for all $(V_m,\ T_U) \in \Omega_{u1}$ that is on the lower right side of

$f_B = 0$. Since $\hat{\Gamma} > 0$ for $(V_m,\ T_U) \in \Omega_{u1}$, one has $\frac{k_t}{R_a} V_m - \frac{2\sqrt{2}T_U}{\pi r_u} r_f > 0$, which means

$$\begin{aligned}\inf_{t\geq 0}\Gamma &= \inf_{t\geq 0}(Gr_f) + \inf_{t\geq 0}[(\frac{k_t}{R_a}V_m - \frac{2\sqrt{2}T_U}{\pi r_u}r_f)f] \\ &= \hat{\Gamma}(V_m, T_U) \geq \delta_1\end{aligned}$$

i.e., $\Gamma \geq \delta_1$ for all $(V_m,\ T_U) \in \Omega_{u1}$ and $t \in \mathbb{R}^+$. Considering Fig. 38(b), for any $(V_m,\ T_U) \in \Omega_{u2}$, there is $(V_m^{\partial},\ T_U) \in \Omega_{u1}$, s.t. $V_m^{\partial} < V_m$ and $f_B(V_m^{\partial}, T_U) = 0$, i.e., $r_f(V_m^{\partial}, T_U) = 0.012$. Defining $r_{\partial} = 0.012$ that is the value of u_{ol} for $(V_m,\ T_U) \in \Omega_{u2}$, one has

$$\begin{aligned}\Gamma &= Gr_{\partial} + f_1 - f_2 r_{\partial} \\ &= Gr_{\partial} + (\frac{k_t}{R_a}V_m - \frac{2\sqrt{2}T_U}{\pi r_u}r_{\partial})f] \\ &> Gr_{\partial} + (\frac{k_t}{R_a}V_m^{\partial} - \frac{2\sqrt{2}T_U}{\pi r_u}r_{\partial})f] \\ &= \Gamma(r_f(V_m^{\partial}, T_U), \theta; V_m^{\partial}, T_U) \geq \delta_1\end{aligned}$$

Thus, $\Gamma \geq \delta_1$ for all $(V_m,\ T_U) \in \Omega_u$ and $t \in \mathbb{R}^+$. **Q**. **E**. **D**.

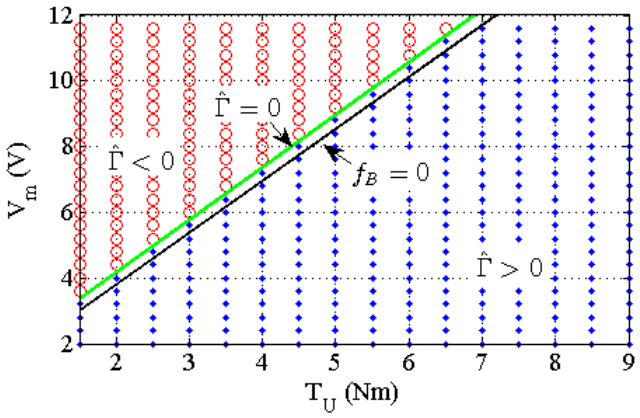

Figure 40: Boundary $\hat{\Gamma} = 0$ compared with the boundary $f_B = 0$; $\hat{\Gamma} < 0$ for the upper left side of the boundary and $\hat{\Gamma} > 0$ for the other side.

The following two propositions show that a solution for Eq. (151) has lower and upper bounds. All the three propositions will be used in the proof of existence and convergence of a periodic solution at steady state for Eq. (151) with $r = u_{ol}$.

Proposition 2

For a periodic differential equation in the form of Eq. (161), if $\Gamma \geq \delta_1$, J is positive definite, and J_θ exists, then there is a positive number δ_4, s.t. for any positive number $\bar{\delta}_4$ that is smaller than δ_4, $\Omega_c = \{\omega = \dot{\theta} : \ \omega > \bar{\delta}_4\}$ is an invariant set.

Proof: Since Eq. (161) is a periodic equation, J_θ and F_m are bounded, and there are $\delta_2, \ \delta_3 > 0$, s.t.

$$\sup_{t \geq 0} |J_\theta| \leq \delta_2, \ \sup_{t \geq 0} |F_m| \leq \delta_3$$

There is $\delta_4 = \min\{2, \frac{\delta_1}{\delta_2+\delta_3}\} > 0$, s.t. for any $0 < \omega \leq \delta_4$, one has

$$\begin{aligned} J\dot{\omega} = \Gamma - \frac{J_\theta}{2}\omega^2 - F_m\omega &> \delta_1 - \frac{1}{2}\delta_2\delta_4^2 - \delta_3\delta_4 \\ &\geq \delta_1 - \delta_2\delta_4 - \delta_3\delta_4 \\ &\geq 0 \end{aligned}$$

Since J is positive definite, $\dot{\omega} > 0$ holds for any $0 < \omega \leq \delta_4$. Thus, for any $\bar{\delta}_4$ with $0 < \bar{\delta}_4 < \delta_4$, Ω_c is an invariant set. **Q**. **E**. **D**.

Since ω is always positive, a coordinate transform defined by a monotonic and continuous function $\theta(t) = \int_0^t \omega d\sigma$ is a bijective map from $\mathbb{R}^+$ to $\mathbb{R}^+$, and Eq. (161) with respect to the new coordinate θ is

$$J(u_{ol}, \theta)\omega\omega' = \Gamma - \frac{1}{2}J_\theta(\theta)\omega^2 - F_m(\theta)\omega \tag{162}$$

where a prime denotes the derivative of a function with respect to θ, $\omega\omega' = \dot{\omega}$, and $J_\theta = J'$ if r is constant; this equation is continuous in ω, which is a sufficient condition for the equation to be Lipchitz, and is piecewise continuous in θ. The inverse of the coordinate transform $t(\theta) = \int_0^\theta \frac{1}{\omega} d\sigma$ exists due to the bijective map, and solutions calculated from Eq. (162) are equivalent to those from Eq. (161). A trajectory of ω at θ with an initial condition $\omega(\theta_0)$ is $\phi(\theta, \omega(\theta_0), \theta_0)$, which is briefly denoted by $\omega(\theta)$. The lower bound of $\omega(\theta)$ is given by **Proposition 2**, and its upper bound is given by the following proposition.

Proposition 3

For a periodic differential equation in the form of Eq. (162), if J is positive definite, J_θ exists, and F_m is positive definite, then for any $\theta_0 \in \mathbb{R}^+$ and $\omega(\theta_0) \in \Omega_c$, there is a positive number

$$\delta_5 = \max\left\{ \bar{\delta}\sqrt{\frac{\sup_{\theta\geq 0} J}{\inf_{\theta\geq 0} J}}, \omega(\theta_0)\sqrt{\frac{\sup_{\theta\geq 0} J}{\inf_{\theta\geq 0} J}} \right\}$$

where

$$\bar{\delta} = \frac{\sup_{\theta\geq 0} J \sup_{\theta\geq 0} \Gamma}{\inf_{\theta\geq 0} J \inf_{\theta\geq 0} F_m}$$

s.t. $\omega(\theta) \leq \delta_5$ for any $\theta > \theta_0$.

Proof: It is proved by contradiction. Since $\sup_{\theta\geq 0} J$ is larger than $\inf_{\theta\geq 0} J$, one always has $\omega(\theta_0) < \delta_5$. For some θ_0 and $0 < \omega(\theta_0) < \bar{\delta}_5$, there is $\theta_1 > \theta_0$ s.t. $\omega(\theta_1) \geq \delta_5$. Without loss of generality, there is no $\theta \in [\theta_0,\ \theta_1)$ s.t. $\omega(\theta_1) > \delta_5$. Since ω is continuous, there is θ_2, s.t. for any $\theta_2 \leq \theta \leq \theta_1$, $\omega(\theta_2) = \max\{\omega(\theta_0), \bar{\delta}\} \leq \omega(\theta)$. Since Γ and J are bounded, F_m is positive and $\omega(\theta) \geq \max\{\omega(\theta_0), \bar{\delta}\}$; from Eq.

(162), one has

$$\begin{aligned}
2\omega(\theta)\omega(\theta)' =&(\omega(\theta)^2)' = \frac{2\Gamma}{J} - \frac{J_\theta}{J}\omega(\theta)^2 - \frac{2F_m}{J}\omega(\theta) \\
&\leq 2\frac{\sup\limits_{\theta\geq 0}\Gamma}{\inf\limits_{\theta\geq 0} J} - \frac{J_\theta}{J}\omega(\theta)^2 - 2\frac{\inf\limits_{\theta\geq 0} F_m}{\sup\limits_{\theta\geq 0} J}\omega(\theta) \\
&\leq 2\frac{\sup\limits_{\theta\geq 0}\Gamma}{\inf\limits_{\theta\geq 0} J} - \frac{J_\theta}{J}\omega(\theta)^2 - 2\frac{\inf\limits_{\theta\geq 0} F_m}{\sup\limits_{\theta\geq 0} J}\bar{\delta} \\
&\leq -\frac{J_\theta}{J}\omega(\theta)^2
\end{aligned}$$

i.e., $(\omega(\theta)^2)_\theta \leq -\frac{J_\theta}{J}\omega(\theta)^2$. By Gronwall-Bellman Lemma [33], one has

$$\begin{aligned}
\omega(\theta)^2 &\leq \omega(\theta_2)^2 \exp\int_{\theta_2}^{\theta_1}(-\frac{J_\theta}{J}d\sigma) \\
&= \omega(\theta_2)^2 \exp\int_{\theta_2}^{\theta_1} d(\ln\frac{1}{J}) \\
&= \omega(\theta_2)^2 \frac{J(\theta_2)}{J(\theta_1)} \\
&\leq \max\{\omega(\theta_0),\bar{\delta}\}^2 \left(\frac{\sup\limits_{\theta\geq 0} J}{\inf\limits_{\theta\geq 0} J}\right)
\end{aligned}$$

i.e.,

$$\omega(\theta) \leq \max\{\omega(\theta_0),\bar{\delta}\}\sqrt{\frac{\sup\limits_{\theta\geq 0} J}{\inf\limits_{\theta\geq 0} J}} = \delta_5$$

for any $\theta_2 \leq \theta \leq \theta_1$, which contradicts $\omega(\theta_1) > \delta_5$. **Q**. **E**. **D**.

Existence of a periodic solution with a period of 2π for Eq. (162) with $r = u_{ol}$

can be shown if one has

$$\omega_\delta(\theta) = \omega - \omega_T = 0 \text{ as } \theta \to +\infty \tag{163}$$

where ω represents $\omega(\theta)$ and ω_T represents $\omega(\theta - 2\pi)$. Since J, Γ and F_m are periodic functions with a period of 2π, the dynamic equation for ω_T with respect to θ is

$$J(u_{ol}, \theta)\omega_T \omega_T' = \Gamma - \frac{1}{2}J_\theta(\theta)\omega_T^2 - F_m(\theta)\omega_T \tag{164}$$

The derivative of ω_δ with respect to θ is

$$\begin{aligned}
\omega_\delta' &= \omega' - \omega_T' \\
&= \frac{1}{J\omega}(\Gamma - \frac{1}{2}J_\theta\omega^2 - F_m\omega) - \frac{1}{J\omega_T}(\Gamma - \frac{1}{2}J_\theta\omega_T^2 - F_m\omega_T) \\
&= \frac{\Gamma}{J\omega} - \frac{\Gamma}{J\omega_T} - \frac{1}{2}\frac{J_\theta}{J}(\omega - \omega_T) \\
&= \Phi\omega_\delta
\end{aligned} \tag{165}$$

where $\Phi = -\frac{\Gamma}{J\omega\omega_T} - \frac{J_\theta}{2J}$. The following theorem shows that $\omega_\delta(\theta)$ asymptotically approaches zero.

Theorem 1

For a periodic differential equation in the form of Eq. (162), if Γ, J and F_m are positive definite, and J_θ exists, then ω converges to a periodic solution for Eq. (162), i.e., Eq. (163) holds.

Proof: A Lyapunov function for Eq. (162) is defined as $V_\delta = \frac{1}{2}J\omega_\delta^2$. With use

of Eq. (165), the derivative of V_δ with respect to θ is

$$\begin{aligned} V_\delta' &= J\omega_\delta\omega_\delta' + \frac{1}{2}J_\theta\omega_\delta^2 \\ &= -\frac{\Gamma}{\omega\omega_T}\omega_\delta^2 - \frac{1}{2}J_\theta\omega_\delta^2 + \frac{1}{2}J_\theta\omega_\delta^2 \\ &= -\frac{\Gamma}{\omega\omega_T}\omega_\delta^2 = -\frac{2\Gamma}{J\omega\omega_T}V_\delta \end{aligned}$$

From **Proposition 2** and **Proposition 3**, ω and ω_T are positive and bounded. Thus, there is a positive number $\delta_6 < \frac{2\Gamma}{J\omega\omega_T}$, s.t.

$$(V_\delta^2)' = 2V_\delta V_\delta' = -\frac{4\Gamma}{J\omega\omega_T}V_\delta^2 < -2\delta_6 V_\delta^2 \tag{166}$$

which means that V_δ^2 exponentially approaches zero by **Theorem 4.10** in [35], i.e., $\omega_\delta = \omega - \omega_T$ asymptotically approaches zero. **Q**. **E**. **D**.

Existence of a periodic solution for Eq. (162) and its convergence are given in **Theorem 1**. However, it does not show that solutions with different initial conditions converge to a unique periodic solution. Due to **Theorem 1**, one can assume that there exists a periodic solution of ω for Eq. (162), which is denoted by $\bar{\omega}(\theta)$. For ω with an arbitrary initial condition, the deviation of ω from $\bar{\omega}$ is denoted by $\Delta\omega = \omega - \bar{\omega}$. Since $\bar{\omega}$ is a solution for Eq. (162), it satisfies

$$J\bar{\omega}' = \frac{\Gamma}{\bar{\omega}} - \frac{1}{2}J_\theta\bar{\omega} - F_m \tag{167}$$

Thus, the derivative of $\Delta\omega$ with respect to θ is

$$\begin{aligned}\Delta\omega' &= \frac{1}{J}(\frac{\Gamma}{\omega} - \frac{1}{2}J_\theta\omega - F_m - J\bar{\omega}') \\ &= \frac{1}{J}[(\frac{\Gamma}{\omega} - \frac{\Gamma}{\bar{\omega}}) - \frac{1}{2}J_\theta(\omega - \bar{\omega})] \\ &= -\frac{\Gamma}{J(\bar{\omega}+\Delta\omega)\bar{\omega}}\Delta\omega - \frac{J_\theta}{2J}\Delta\omega \end{aligned} \tag{168}$$

The following theorem shows that ω with an arbitrary initial condition converges to a unique periodic solution $\bar{\omega}(\theta)$.

Theorem 2

For a periodic differential equation in the form of Eq. (162), if Γ, J and F_m are positive definite, and J_θ exists, then ω with an arbitrary initial condition $\omega(\theta_0) \in \Omega_c$ converges to a unique periodic solution $\bar{\omega}(\theta)$, i.e., $\Delta\omega = 0$ is an asymptotically stable equilibrium for Eq. (168).

Proof: Let $\mu = \frac{\Delta\omega}{\bar{\omega}}$; one has

$$\Delta\omega' = (\mu\bar{\omega})' = \mu'\bar{\omega} + \mu\bar{\omega}_\theta \tag{169}$$

Substituting Eq. (169) into Eq. (168) yields

$$\mu' = (-\frac{\Gamma}{J\bar{\omega}^2(1+\mu)} - \frac{J_\theta}{2J} - \frac{\bar{\omega}'}{\bar{\omega}})\mu \tag{170}$$

which is a periodic differential equation. A Lyaponuv function is defined as $V(\theta) = \frac{1}{2}\mu^2 J(\theta)\bar{\omega}^2$, which is a positive definite function. Since $\Gamma > 0$ and $\mu + 1 = \frac{\omega}{\bar{\omega}} > 0$

from **Proposition 2** and **Proposition 3**, the derivative of V with respect to θ is

$$\begin{aligned} V(\theta)' &= \mu\mu' J\bar{\omega}^2 + \frac{1}{2}\mu^2 J_\theta \bar{\omega}^2 + \mu^2 J\bar{\omega}\bar{\omega}' \\ &= J\bar{\omega}^2(-\frac{\Gamma}{J\bar{\omega}^2(1+\mu)} - \frac{J_\theta}{2J} - \frac{\bar{\omega}'}{\bar{\omega}})\mu^2 + (\frac{J_\theta}{2}\bar{\omega}^2 + J\bar{\omega}\bar{\omega}')\mu^2 \\ &= -\frac{\Gamma}{(1+\mu)}\mu^2 \leq 0 \end{aligned}$$

which is true for any $\mu \in \Omega_0 = \{\mu \in \mathbb{R} : \ \mu + 1 > 0\}$, and the set $\Omega_v = \{\mu \in \Omega_0 : V^{'} = 0\}$ only contains $\mu = 0$. Since $\mu = \frac{\omega}{\bar{\omega}} - 1$ is bounded due to **Proposition 3**, its limit set Ω_s is nonempty. Following the procedure of **Lemma 5.3.71** in [34], which is Lasalle's invariant principle for periodic systems, one has $\Omega_s \subseteq \Omega_v$. Since Ω_v only contains $\mu = 0$, $\mu = 0$ is an asymptotically stable equilibrium for Eq. (170), i.e., ω with an arbitrary initial condition $\omega(\theta_0) \in \Omega_c$ converges to $\bar{\omega}$. On the other hand, since $\frac{\Gamma}{\omega} - \frac{1}{2}J_\theta\omega - F_m$ is uniformly differentiable in ω on Ω_c and piecewisely continuous in θ, Eq. (162) with an initial condition $\omega(\theta_0)$ has a unique solution [35], which proves that ω converges to a unique $\bar{\omega}$. **Q**. **E**. **D**.

From **Proposition 1**, Γ is designed to be positive definite in the IVT system, and in reality J and F_m are always positive definite as shown in Eq. (151). Thus, the open loop control u_{ol} can make $\omega \in \Omega_c$ converge to an unique periodic solution $\bar{\omega}$ when V_m and T_U are given, which shows stability of the open loop control.

4.3 Design of an Integral Time-Delay Feedback Control for the IVT System

Since there are always some differences between the mathematic model of the IVT system and the real system, the average of ω over 2π in θ cannot be exactly adjusted to ω_0 by the open loop control, and a robust feedback control should be incorporated with the open loop control. Since one has no access to the average of ω in real time, it is approximated by a time-delay variable

$$\omega_a = \frac{2\pi}{\int_{\theta(t)-2\pi}^{\theta(t)} \frac{d\sigma}{\omega}}$$

which is the average of ω in a period of 2π prior to the current angular position. If ω converges to a periodic solution, ω_a converges to the average of ω. Thus, the goal of the feedback control is the convergence of ω_a to ω_0. In order to eliminate the static error between ω_a and ω_0, an integral time-delay feedback control for the IVT system can be designed as

$$\begin{cases} J\omega' = \frac{Gr+f_1-f_2r}{\omega} - \frac{1}{2}J_\theta\omega - F_m \\ r' = k(\omega_a - \omega_0) + k_2(\omega - \omega_T) \end{cases} \tag{171}$$

where k is the integral gain, k_2 is a gain that can provide damping, and they should be selected so that the system in Eq. (171) is at least locally stable. If uncertainty of the IVT system is not significant, ω and r can be adjusted close to their correct solutions by the open loop control, and one just needs to study local stability of the feedback control system in Eq. (171). In Eq. (171) whose independent variable

$\theta = \int_0^t \omega d\sigma$ is not a time variable, the constant delay 2π in θ is also referred to as the "time delay" in this work. There is no ambiguity of the term "time delay" since no explicitly expressed delay in t is used here. A new variable $z = \int_{\theta(t)-2\pi}^{\theta(t)} \frac{d\sigma}{\omega}$ is used to represent the time-delay integral in ω_a, and Eq. (171) changes to

$$\begin{cases} J\omega' = \frac{Gr+f_1-f_2 r}{\omega} - \frac{1}{2}J_\theta \omega - F_m \\ r' = k(\frac{2\pi}{z} - \omega_0) + k_2(\omega - \omega_T) \\ z' = \frac{1}{\omega} - \frac{1}{\omega_T} \end{cases} \tag{172}$$

where $\omega_T = \omega(\theta - 2\pi)$. To study local stability of the time-delay system in Eq. (171), Eq. (172) can be analogous to a distributed-parameter system without time delay, where an additional coordinate x is analogous to a space coordinate. A new dependent variable $u(\theta, x)$ is defined as $u(\theta, x) = \omega(\theta - x)$ with $\theta \in \mathbb{R}$ and $x \in [0,\ 2\pi]$, where $\omega(\theta - x)$ is the speed with a delay x, which corresponds to the current speed $\omega(\theta)$; at boundaries $x = 0$ and $x = 2\pi$, $u(\theta, 0) = \omega$ and $u(\theta, 2\pi) = \omega_T$, respectively. The analogy is shown in Fig. 41. The governing equation of $u(\theta, x) = \omega(\theta - x)$ is $u_x + u_\theta = 0$, and its boundary conditions can be obtained from Eq. (172). In Eq. (172), only $\omega_T = u(\theta, 2\pi)$ is a variable at the boundary $x = 2\pi$, and others are variables at $x = 0$. Thus, the governing equation and boundary conditions

for the distributed-parameter system are

$$\begin{cases} u_x + u_\theta = 0 & (37.a) \\ Ju_\theta(\theta,0) = \frac{Gr+f_1-f_2 r}{u(\theta,0)} - \frac{1}{2}J_\theta u(\theta,0) - F_m & (37.b) \\ r' = k(\frac{2\pi}{z} - \omega_0) + k_2[u(\theta,0) - u(\theta,2\pi)] & (37.c) \\ z' = \frac{1}{u(\theta,0)} - \frac{1}{u(\theta,2\pi)} & (37.d) \end{cases} \tag{173}$$

By assuming that correct solutions of ω, r and z at steady state are $\bar{\omega}$, $\bar{r}$ and $\bar{z} = \frac{2\pi}{\omega_0}$, respectively, local stability of Eq. (173) can be studied on its linearization around $\bar{u}(\theta,x) = \bar{\omega}(\theta - x)$, $\bar{r}$ and $\bar{z} = \frac{2\pi}{\omega_0}$. With $\Delta u(\theta,x) = \omega(\theta - x) - \bar{\omega}(\theta - x)$, $\Delta r = r - \bar{r}$ and $\Delta z = z - \bar{z}$, a linearized equation of Eq. (173) is

$$\begin{cases} \Delta u_x + \Delta u_\theta = 0 & (174.a) \\ \Delta u_\theta(\theta,0) = A\Delta r + B\Delta u(\theta,0) & (174.b) \\ \Delta r' = K\Delta z + k_2[\Delta u(\theta,0) - \Delta u(\theta,2\pi)] & (174.c) \\ \Delta z' = C[\Delta u(\theta,0) - \Delta u(\theta,2\pi)] & (174.d) \end{cases} \tag{174}$$

where A, B and C are periodic functions of θ and they are given in **Appendix B**, and $K = -\frac{k\omega_0^2}{2\pi}$ is constant. The derivation of Eq. (174) is given in **Appendix B**.

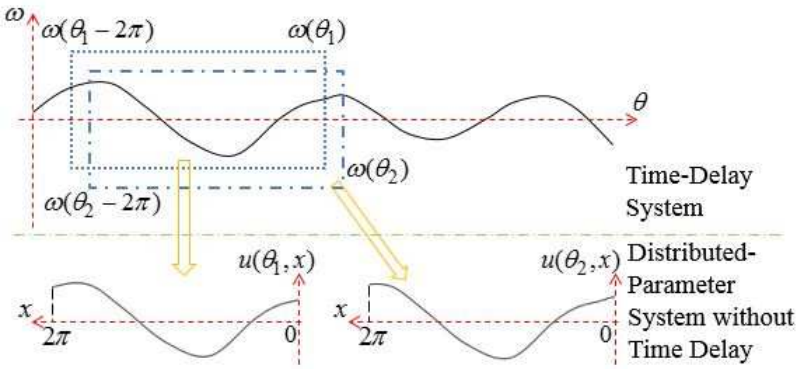

Figure 41: Analogy between a time-delay system and a distributed-parameter system without time delay; the left graph for the distributed-parameter system is the shape of $u(\theta,x)$ at $\theta=\theta_1$ and $x\in[0,\ 2\pi]$, and the right graph is the shape of $u(\theta,x)$ at $\theta=\theta_2$ and $x\in[0,\ 2\pi]$.

To numerically study stability of Eq. (174) by the spectral Tau method, the first N^{th}-order Chebyshev polynomials can be used as trial functions to spatially discretize the distributed-parameter system in Eq. (174). In order to simplify the illustration of the process, N is selected as an even number. The first N^{th}-order Chebyshev polynomials defined in the domain $x\in[0,\ 2\pi]$ are $T_i(x)=\cos i\alpha(x)$ with $i=0,\cdots,N$, where $\alpha(x)=\arccos(\frac{x}{\pi}-1)$. A set of trial functions is $\mathbf{T}=\{T_0\ \cdots\ T_N\}^{\mathrm{T}}$, and its derivative with respect to x is $\frac{d}{dx}\mathbf{T}=\mathbf{DT}$, where [78]

$$\mathbf{D}=\left\{\begin{array}{cc}\underline{\mathbf{0}}^{\mathrm{T}} & 0\\ \mathbf{D}_r^{\mathrm{T}} & \underline{\mathbf{0}}\end{array}\right\}$$

$$\mathbf{D}_r = \frac{1}{2\pi}\begin{Bmatrix} 2 & 0 & \cdots & & & \\ 0 & 8 & 0 & \cdots & & \\ & & \vdots & & & \\ 2(N-1) & 0 & 4(N-1) & 0 & \cdots & \\ 0 & 4N & 0 & 4N & 0 & \cdots \end{Bmatrix}^{\mathrm{T}}$$

and $\underline{\mathbf{0}}$ is a N^{th}-order zero column vector. Due to orthogonality of $\mathbf{T}$, one has $\frac{2}{\pi}\int_0^\pi \bar{\mathbf{T}}\mathbf{T}^{\mathrm{T}} d\alpha = \mathbf{I}_{N+1}$, where $\bar{\mathbf{T}} = \{\frac{1}{2}T_0\ T_1\ \cdots\ T_N\}^{\mathrm{T}}$ is a set of test functions and $\mathbf{I}_{N+1}$ is the $(N+1)^{th}$-order identity matrix. An approximation of Δu after the discretization is $\Delta u(\theta,x) = \sum_{i=0}^{N} q_i(\theta)T_i(x) = \mathbf{T}^{\mathrm{T}}\mathbf{q}$, where $\mathbf{q} = \{q_0(\theta)\ \cdots\ q_N(\theta)\}^{\mathrm{T}}$ is a set of generalized coordinates. Using $\Delta u(\theta,x) = \mathbf{T}^{\mathrm{T}}\mathbf{q}$ in Eq. (174.a) yields

$$\Delta u_x + \Delta u_\theta = (\frac{d}{dx}\mathbf{T}^{\mathrm{T}})\mathbf{q} + \mathbf{T}^{\mathrm{T}}\mathbf{q}' = \mathbf{T}^{\mathrm{T}}\mathbf{D}^{\mathrm{T}}\mathbf{q} + \mathbf{T}^{\mathrm{T}}\mathbf{q}' = 0$$

Since there is a boundary condition in Eq. (174.b) for Eq. (174.a), the spectral Tau method is used, where a set of test functions with the first $(N-1)^{th}$-order Chebyshev polynomials is $\mathbf{T}_r = \{\frac{1}{2}T_0\ T_1\ \cdots\ T_{N-1}\}^{\mathrm{T}}$. Pre-multiplying $\frac{2}{\pi}\mathbf{T}_r$ on two sides of $\mathbf{T}^{\mathrm{T}}\mathbf{D}^{\mathrm{T}}\mathbf{q} + \mathbf{T}^{\mathrm{T}}\mathbf{q}' = 0$ and integrating the resultant equation from zero to π yield

$$\begin{aligned} &\int_0^\pi \frac{2}{\pi}\mathbf{T}_r\mathbf{T}^{\mathrm{T}} dx(\mathbf{D}^{\mathrm{T}}\mathbf{q} + \mathbf{q}') \\ &\quad = \{\mathbf{I}_N\ \underline{\mathbf{0}}\}(\mathbf{D}^{\mathrm{T}}\mathbf{q} + \mathbf{q}') \\ &\quad = \{\underline{\mathbf{0}}\ \mathbf{D}_r\}\mathbf{q} + \{\mathbf{I}_N\ \underline{\mathbf{0}}\}\mathbf{q}' = \underline{\mathbf{0}} \end{aligned} \tag{175}$$

Substituting $\Delta u(\theta,0) = \mathbf{T}_0^{\mathrm{T}}\mathbf{q}$ into Eq. (174.b), where $\mathbf{T}_0^{\mathrm{T}} = \mathbf{T}^{\mathrm{T}}(0) = \{1\ -1\ 1\ \cdots\ -1\ 1\}$ is an $(N+1)^{th}$-order row vector , yields

$$\mathbf{T}_0^{\mathrm{T}}\mathbf{q}' = A\Delta r + B\mathbf{T}_0^{\mathrm{T}}\mathbf{q} \tag{176}$$

Substituting both $\Delta u(\theta,0) = \mathbf{T}_0^{\mathrm{T}}\mathbf{q}$ and $\Delta u(\theta,2\pi) = \mathbf{T}_I^{\mathrm{T}}\mathbf{q}$ into Eqs. (174.c) and (174.d), where $\mathbf{T}_I$ is an $(N+1)^{th}$-order column vector with all elements being unit, yields

$$\Delta r' = K\Delta z + k_2(\mathbf{T}_0^{\mathrm{T}} - \mathbf{T}_I^{\mathrm{T}})\mathbf{q} \tag{177}$$

$$\Delta z' = C(\mathbf{T}_0^{\mathrm{T}} - \mathbf{T}_I^{\mathrm{T}})\mathbf{q} \tag{178}$$

respectively. With use of Eqs. (175) through (178), the partial differential equation in Eq. (174) can be discretized to an ordinary differential equation (ODE):

$$\eta' = \mathscr{A}\eta \tag{179}$$

where $\eta = \{\mathbf{q}^{\mathrm{T}}\ \Delta r\ \Delta z\}^{\mathrm{T}}$ is a variable vector, $\mathscr{A}$ is a periodic system matrix with a period of 2π and is given in **Appendix C**, and the derivation of the ODE is also shown in **Appendix C**. Stability of Eq. (179) can be analyzed by Floquet theory. The transformation matrix that transforms η from θ to $\theta + 2\pi$ can be numerically calculated [57], and locations of eigenvalues of the transformation matrix indicate stability of the system in Eq. (179). The goal of the feedback control can be interpreted as to find k and k_2 so that all eigenvalues of the transformation matrix are located inside the unit circle.

It is possible to obtain fast convergence of Eq. (179) to the origin for all V_m and T_U in their working regions with use of variable k and k_2 as functions of V_m and T_U. However, constant k and k_2 can also achieve exponential stability for all V_m and T_U, and its control law can be simple. Stability of Eq. (179) with $k = 0.01$ mm$\cdot$rad^{-1} and $k_2 = 0.02$ mm$\cdot$rad^{-1} is evaluated by searching maximum absolute eigenvalues when V_m and T_U are chosen for all combinations in $V_m \in \{2 \;\; 2.4 \;\cdots\; 11.6 \;\; 12\}$ and $T_U \in \{1.5 \;\; 2 \;\cdots\; 8.5 \;\; 9\}$, as shown in Fig. 42. It shows that all maximum absolute eigenvalues are smaller than one, which indicates that Eq. (179) is locally exponentially stable for all V_m and T_U. By choosing proper values of k and k_2, the maximum absolute eigenvalues for some V_m and T_U can be adjusted to some smaller value, which yields faster convergence. For example, if $k = 0.06$ mm$\cdot$rad^{-1} and $k_2 = 0.12$ mm$\cdot$rad^{-1}, the maximum absolute eigenvalue for $V_m = 7$ V and $T_U = 2$ Nm is 0.4871, while it is 0.7776 if $k = 0.01$ mm$\cdot$rad^{-1} and $k_2 = 0.02$ mm$\cdot$rad^{-1}. The example also shows that convergence can be faster with use of more control effort. The IVT system with the combination of the time-delay feedback control and the open loop control is

$$\begin{cases} J\omega' = \frac{Gr+f_1-f_2 r}{\omega} - \frac{1}{2}J_\theta \omega - F_m \\ r = u_{ol}(V_m, T_U) + r_d \\ r_d' = k(\omega_a - \omega_0) + k_2(\omega - \omega_T) \end{cases} \tag{180}$$

With $T_U = 8$ Nm and a sudden drop of V_m from 8 V to 7 V, approximated averages of ω, i.e., ω_a, for the IVT system with and without the time-delay feedback control are shown in Fig. 43. Since the value of r is overestimated for $V_m = 8$ V by the open

loop control in Eq. (160) and it is underestimated for $V_m = 7$ V, there are negative and positive static errors for ω_a with use of the open loop control, respectively. Figure 43 shows that static errors can be eliminated by the feedback control and the speed of convergence is increased. If only the current angular speed ω is used as the feedback, the IVT system with the combination of the feedback control and the open loop control is

$$\begin{cases} J\omega' = \frac{Gr+f_1-f_2 r}{\omega} - \frac{1}{2}J_\theta \omega - F_m \\ r = u_{ol}(V_m, T_U) + r_d \\ r_d' = k(\omega - \omega_0) + k_2 \omega' \end{cases} \tag{181}$$

Performances of feedback control variables with and without time delay are compared. When $k = 0.01$ mm $\cdot$ rad^{-1} and $k_2 = 0.02$ mm $\cdot$ rad^{-1} are used for the feedback control with time delay, and $k = 0.04$ mm $\cdot$ rad^{-1} and $k_2 = 0.15$ mm $\cdot$ rad^{-1} are used for the feedback control without time delay, the two IVT systems with the different feedback controls have similar convergence for ω_a, as shown in Fig. 44. In this condition, the control variable for the feedback control with time delay is much smoother than that without time delay, as shown in Fig. 45, and the control effort with time delay is lower than that without time delay.

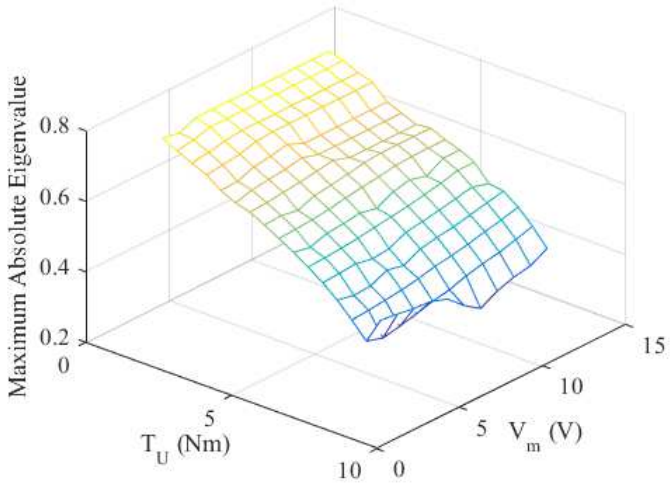

Figure 42: Maximum absolute eigenvalues of the transformation matrix for $\mathscr{A}$

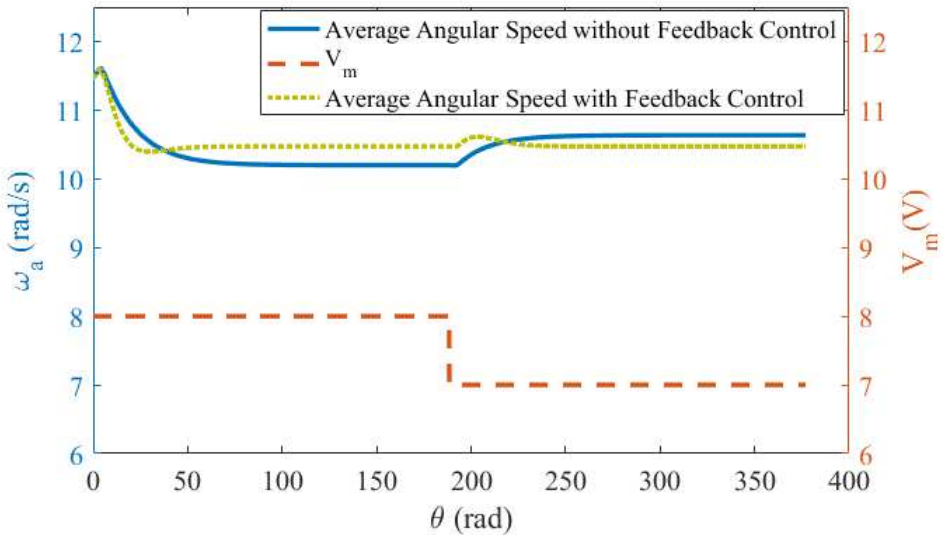

Figure 43: Histories of ω_a with and without the time-delay feedback control, and the history of V_m; the output torque $T_U = 8$ Nm is constant.

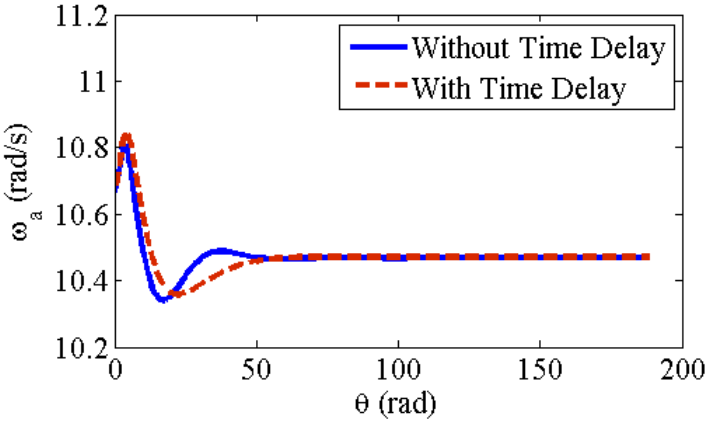

Figure 44: Histories of ω_a for the feedback control with and without time delay, where $T_U = 8$ Nm and $V_m = 8$ V

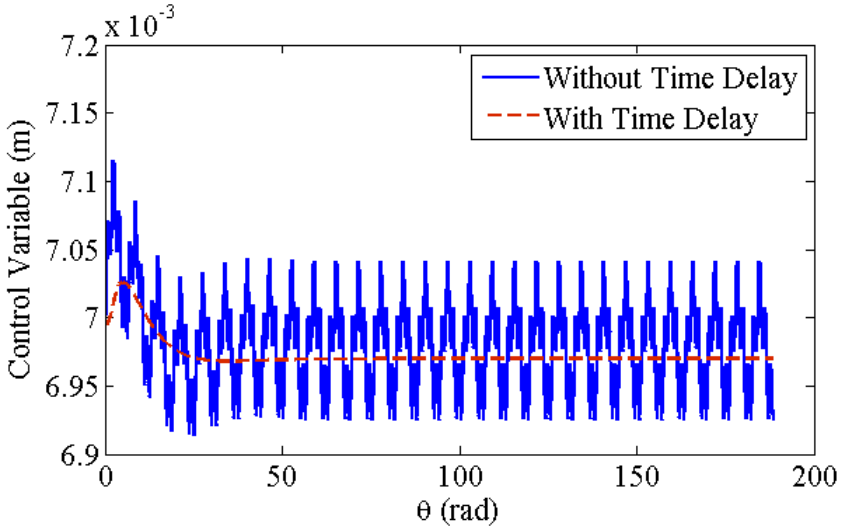

Figure 45: Histories of control variables r for the feedback control with and without time delay, where $T_U = 8$ Nm and $V_m = 8$ V

4.4 Testing of the SGIVT

4.4.1 Experimental Setup

In this section, an experimental setup for the prototype of the SGIVT introduced in Sec. 2.2 was built to evaluate the kinematic performance of the SGIVT, as well as its speed ratio adjustment performance in driving tests. The setup consists of the SGIVT, a DC motor, a stepper motor, a brake, two torque sensors, and four rotary encoders, as shown in Fig. 46. In addition, there are some controllers and power supplies that work with the main components. The components are monitored and controlled through a Data Acquisition (DAQ) interface that communicates with LabVIEW programs on a computer. The DC motor is connected to the shaft where NG1 is installed, and there are an encoder and a torque sensor on the shaft to monitor the speed and the torque of NG1. The DC motor is controlled by an adjustable DC voltage converter to simulate an engine. The stepper motor provides the active control speed, and an encoder is used as a feedback of the stepper motor. The brake connected to the output shaft is powered by another adjustable DC voltage converter to represent resistance, and an encoder and a torque sensor are installed on the output shaft to monitor the speed and the torque of the output shaft. An extra encoder rides on the input shaft of the SGIVT, where NG2 is installed, to monitor the speed of NG2.

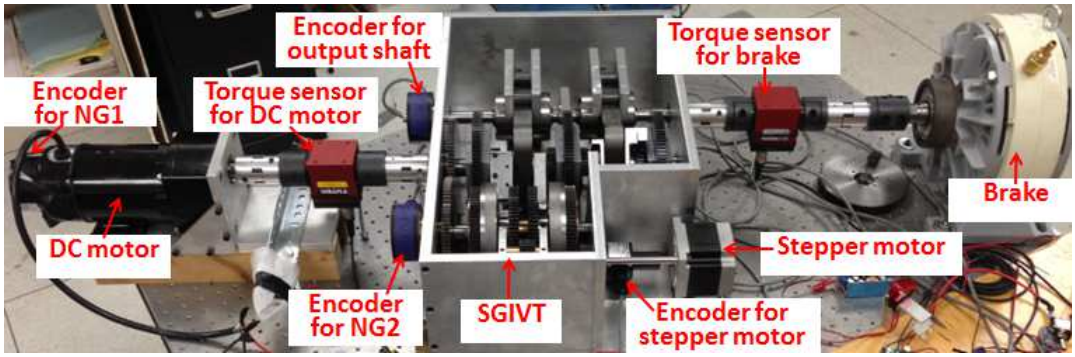

Figure 46: Experimental setup of the SGIVT

4.4.2 Experimental Validation of Average and Instantaneous Speed Ratios

Average and instantaneous speed ratios are experimentally validated by comparing the theoretical and experimental speed ratios. To have an expression for the theoretical speed ratio, the relation between the speed of the stepper motor ω_{CT} and the crank length e is first derived. In this design, control speeds, ω_{ACG} and ω_{ICG} in Sec. 2.2.2, are proportional to ω_{CT} by a factor of $\frac{1}{4}$:

$$\omega_{\mathrm{ACG}} = -\frac{1}{4}\omega_{\mathrm{CG}},\ \omega_{\mathrm{ICG}} = \frac{1}{4}\omega_{\mathrm{CG}} \tag{182}$$

Substituting speed relations $\omega_{\mathrm{CG1}} = -3\omega_{\mathrm{RG1}}/4$ and $\omega_{\mathrm{CG2}} = -3\omega_{\mathrm{RG2}}/4$ into Eq. (23) and substituting Eqs. (20) and (21) into the resultant equation yield

$$v_{\mathrm{CRK}} = \frac{1}{8}(\omega_{\mathrm{SG1}} - \omega_{\mathrm{SG2}})r_{\mathrm{CG}} \tag{183}$$

Substituting speed relations $\omega_{SG1} = -7\omega_{ACG}/18$ and $\omega_{SG2} = -7\omega_{ICG}/18$ into Eq. (182) and substituting the resultant equation into Eq. (183) yield

$$v_{CRK} = \frac{7}{288}\omega_{CT} r_{CG} \tag{184}$$

Integrating v_{CRK} and ω_{CT} with respect to time gives the crank length e and the angle of the stepper motor θ_{CT}, respectively. Integrating two sides of Eq. (184) with respect to time with $r_{CG} = 1$" and changing the unit of θ_{CT} from rad to degree in the resultant equation yield

$$e = \frac{7\pi}{51840}\theta_{CT} \tag{185}$$

which is the theoretical relation between e and θ_{CT}. The maximum crank length is reached when $\theta_{CT} = 3600^o$. Substituting Eq. (185) into Eq. (35) yields the theoretical instantaneous output-to-input speed ratio of the SGIVT without the pair of noncircular gears in terms of θ_{CT} and θ_{in}. When θ_{CT} is fixed, R in Eq. (35) is a periodic function of θ_{in} with a period of 2π. The average output-to-input speed ratio, which is the average value of R over a period of 2π, for a given θ_{CT} is

$$R_{avg}(\theta_{CT}) = \frac{2\sqrt{2}}{\pi}\frac{7\pi}{51840}\frac{\theta_{CT}}{r_{OG}} \approx \frac{7}{27492}\theta_{CT}$$

where $r_{OG} = 1.5$" is used here. To validate this relation, average speed ratios were measured when θ_{CT} is at 0^o, 100^o, ..., 3500^o, 3600^o. The experimental and theoretical average speed ratios are shown in Fig. 47, which match quite well.

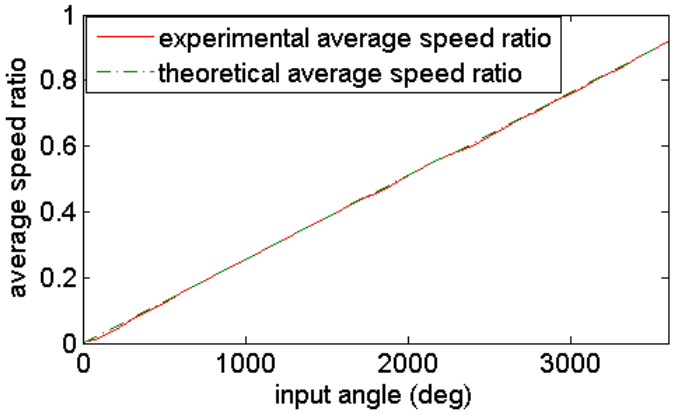

Figure 47: Comparison of experimental and theoretical average speed ratios

Since the linearity of the average speed ratio is experimentally validated in Fig. 47, the instantaneous speed ratio in Eq. (35) can be validated by setting θ_{CT} at an arbitrary value, which was selected as 3600^o. The speed ratio of the SGIVT without the noncircular gears in Eq. (35) and that of the pair of noncircular gears in Eq. (38) are expressed in terms of θ_{in}, which is the angle of the noncircular gear on the input shaft NG2. In the test, the speed of the output shaft and that of the noncircular gear on the engine shaft NG1 were sampled at a constant interval of θ_{in}, i.e., they are sample at every 45^o of θ_{in} (every 15 pulses from the encoder for NG2), and there are 80 sampling points in every period of θ_{in}. Since encoders' resolution, which is 1200 pulses per revolution (0.3^o per pulse), can introduce quantization error in experimental data, the test lasted for 75 periods of θ_{in} to eliminate the quantization error. At every sampling point, there were 75 repeated measurements of the speed of the output shaft or that of NG1, and the mean value of the 75 measurements at every point is the expectation of the speed of the output shaft or that of NG1. The

speed ratio of the pair of noncircular gears and that of the SGIVT without the noncircular gears are obtained by dividing the expected speed of NG1 and that of the output shaft by the expected speed of NG2, respectively, as shown in Fig. 48. The experimental speed ratio of the noncircular gears is seen to be close to the theoretical one, but there are relatively large deviations between the experimental speed ratio of the SGIVT without the noncircular gears and the theoretical one, which are introduced by manufacturing and assembly errors at connections of scotch yokes and assembly errors of cranks, and due to misalignment between pins of cranks and slots of yokes. The errors can be reduced by a more robust design to increase the manufacturing and assembly accuracy. While there are some derivations between the theoretical and experimental speed ratios in Fig. 48, variations of the experimental speed ratio of the SGIVT is significantly reduced by using the pair of noncircular gears. The variance of the speed ratio with the noncircular gears is 1.33% of its average value.

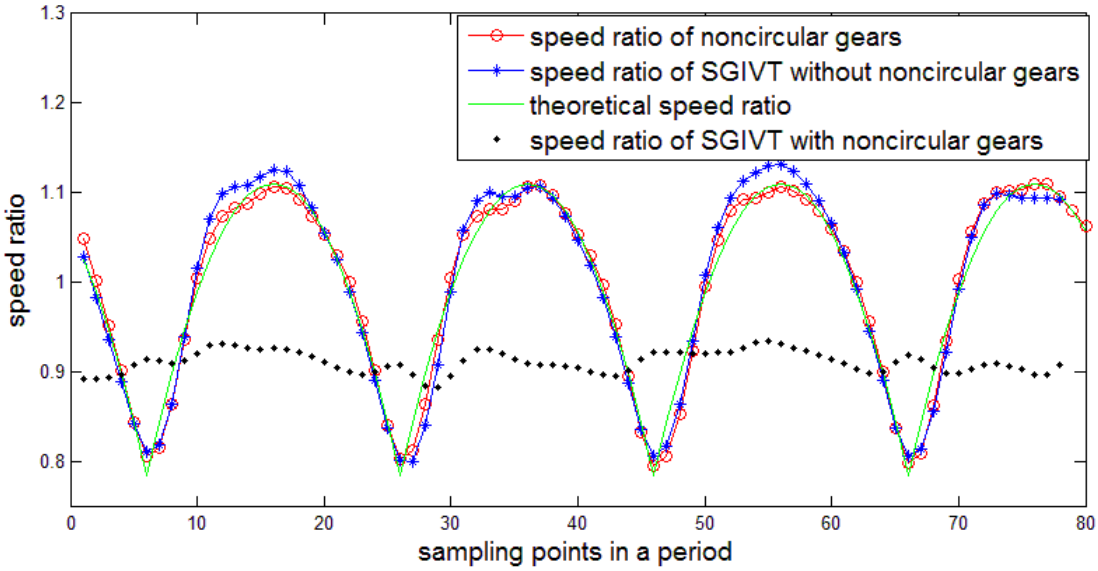

Figure 48: Experimental speed ratio of the noncircular gears, experimental speed ratios of the SGIVT with and without the noncircular gears, and the theoretical speed ratio of the noncircular gears or that of the SGIVT without the noncircular gears

4.4.3 Driving test of the SGIVT

The setup for the driving test is shown in Fig. 46, where the brake simulates resistance of a car and the input voltage of the DC motor simulates throttle opening of the engine of the car. There was a designed time history of the resistance to simulate startup resistance, flat road resistance, uphill resistance and downhill resistance. The purpose of the test was to keep the speed of the DC motor to be constant during the time history, in order to save energy when the prime mover is an engine. A simple feedback controller was built to control the stepper motor to adjust the speed ratio of the SGIVT. The block diagram of the controller is shown

in Fig. 49, and it was implemented in LabVIEW. The reference speed of the DC motor is $\omega_r = 60$ RPM, and the difference between the reference speed and the real speed of the DC motor ω_m is an error denoted by ω_{err}. The error goes through a proportional block and multiplied by a gain K, which provides an increment of the angle of the stepper motor $\Delta\theta_{\text{CT}}$. The increment of the angle is accumulated by the stepper motor, and the accumulated angle θ_{CT} affects the average speed ratio of the SGIVT in the plant block, which can in turn affect ω_m. The new ω_m is sampled and sent back to the controller to generate a new error.

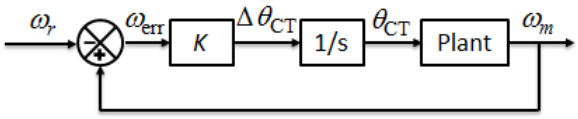

Figure 49: Block diagram of the controller for the SGIVT

The gain of the proportional block influences the response speed and stability of the controller. A large K can increase the response speed but introduce instability in the controller. Hence, a proper value of K should be selected, and a mathematical model of the controller can assist in estimating K. There are three major simplifications for the control system: 1) the plant consists of two parts, the DC motor and the SGIVT; 2) when the speed ratio is changed, the transient state of the SGIVT is not considered and the speed of the DC motor immediately goes to steady state; and 3) the speed of the DC motor and that of the output shaft are the average speeds over a revolution of the input shaft, and instantaneous speed variations are not considered. With these simplifications, the model of the DC motor at steady state is

simply expressed by

$$\dot{\omega}_m = 0 = \frac{K_t}{J_m R_m}(V - K_e \omega_m) - \frac{T_{\text{in}}}{J_{\text{m}}} \tag{186}$$

where K_t is the motor torque constant, J_m is the moment of inertia of the motor shaft, R_m is the electric resistance, V is the input voltage of the DC motor, K_e is the electromotive-force constant, and T_{in} is the input torque of the SGIVT. The relation between T_{in} and the output torque T_{out}, which is the resistance provided by the brake, is

$$T_{\text{in}} = R_{\text{avg}} T_{\text{out}} = \frac{7}{27492}\theta_{\text{CT}} T_{\text{out}}$$

Substituting the above equation into Eq. (186) yields

$$\omega_m = K_1 V - K_2 T_{\text{out}} \theta_{\text{CT}} \tag{187}$$

where $K_1 = 1/K_e$ and $K_2 = 7R_m/27492K_tK_e$. With this relation, a discrete-time model of the controller can be obtained.

It is assumed that the input voltage V and the output load T_{out} in the discrete-time model do not change in a short time period. At time k, the sampled speed of the DC motor and the angle of the stepper motor are $\omega_{m,k}$ and $\theta_{\text{CT},k}$, respectively. Using $\omega_m = K_1 V - K_2 T_{\text{out}} \theta_{\text{CT}}$, the expression for $\omega_{m,k}$ is

$$\omega_{m,k} = K_1 V - K_2 T_{\text{out}} \theta_{\text{CT},k} \tag{188}$$

At next time $k+1$, the error is $\omega_{\text{err},k+1} = \omega_{m,k} - \omega_r$, and the angle of the stepper motor is accumulated from that at time k:

$$\theta_{\text{CT},k+1} = K\omega_{\text{err},k+1} + \theta_{\text{CT},k} = K(K_1 V - K_2 T_{\text{out}}\theta_{\text{CT},k} - \omega_r) + \theta_{\text{CT},k} \tag{189}$$

Replacing $\theta_{\text{CT},k}$ in Eq. (188) by that in Eq. (189) and subtracting Eq. (189) from the resulting equation yield

$$\omega_{m,k+1} = (1 - K_2 T_{\text{out}} K)\omega_{m,k} + K_2 T_{\text{out}} K \omega_r \tag{190}$$

which is a recursive formula for $\omega_{m,k}$ with respect to k. Let l range from k to 0. Multiplying two sides of Eq. (190) with k replaced by l, by $(1 - K_2 T_{\text{out}} K)^{k-l}$, yields

$$(1 - K_2 T_{\text{out}} K)^{k-l}\omega_{m,l+1} = (1 - K_2 T_{\text{out}} K)^{k+1-l}\omega_{m,l} + K_2 T_{\text{out}} K \omega_r (1 - K_2 T_{\text{out}} K)^{k-l} \tag{191}$$

Summing two sides of Eq. (191) with l ranging from k to 0 and subtracting

$$\sum_{i=1}^{k} (1 - K_2 T_{\text{out}} K)^{k+1-i}\omega_{m,i}$$

from two sides of the resulting equation yield

$$\omega_{m,k+1} = (1 - K_2 T_{\text{out}} K)^{k+1}\omega_{m,0} + \omega_r[1 - (1 - K_2 T_{\text{out}} K)^k] \tag{192}$$

The above equation provides three implications on the stability of the controller: 1) V does not affect the stability of the controller, as long as it is a constant; 2) if $|1 -$

$K_2 T_{\text{out}} K| < 1$, $\omega_{m,k+1}$ converges to ω_r as k approaches infinity, and the controller is stable; and 3) when T_{out} is a constant, a larger T_{out} leads to a narrower range of K to make the controller stable. Since V and T_{out} cannot be constants for a large time, $\omega_{m,k+1}$ needs to converge as fast as possible to ensure stability of the controller. Hence, an estimate of K can be $K = 1/(K_2 T_{\text{out}})$, and T_{out} is selected as the largest output torque, which guarantees that the controller be stable for any T_{out}. By Eq. (187), $K_2 T_{\text{out}}$ is the slope of the linear equation there, which can be estimated by fitting a linear equation for the measured speed of the DC motor and the angle of the stepper motor, as shown in Fig. 50, and the estimated slope is $K_2 T_{\text{out}} = 0.0128$, which indicates that the estimated value of K is 78. With a preliminary guess of $K = 78$, the real value of K was obtained by trial and error, and $K = 50$ was finally used.

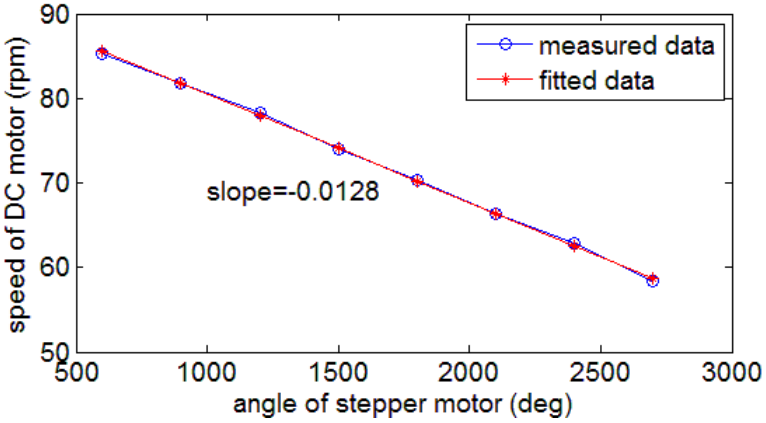

Figure 50: Slope of linear regression from the measured speed of the DC motor and the angle of the stepper motor

The driving test results for $K = 50$ and $\omega_r = 60$ RPM are shown in Fig. 51. The driving test can be divided into six stages. In the first stage, the speed of the DC motor was set to be a constant, 50 RPM, to simulate an idler speed. In the second stage, the input voltage was increased to accelerate the DC motor from the idler speed to the reference speed of 60 RPM, and the controller for the SGIVT started to increase the speed ratio and accelerate the output speed at the end of this stage. At the beginning of the third stage, the resistance steeply increased to simulate the startup resistance, and the input voltage was further increased to overcome the resistance. There was an overshoot in the speed of the DC motor at the beginning; the controller then adjusted the speed back to the reference speed by changing the angle of the stepper motor. At the end of the third stage, the resistance dropped and the output speed increased, while the speed of the DC motor was still a constant. At the beginning of the fourth stage, the input voltage was increased to its maximum value. To adjust the speed of the DC motor back to the reference speed, the angle of the stepper motor went to its maximum value, so that there was a flat curve in its plot. The resistance then steeply increased and the speed of the DC motor dropped. The controller captured this drop and rapidly decreased the angle of the stepper motor, and the speed of the DC motor went back to the reference speed. In the fifth stage, the input voltage was continuously decreased to simulate the stop of a car, and the output speed sharply dropped, while the DC motor voltage was still a constant. In the sixth stage, the controller was shut down and the output speed went to zero, while the DC motor went to the idler speed. The results of the driving test indicate that the SGIVT has the ability to make its input speed constant. A more sophisticated controller that can incorporate nonlinear and transient dynamics of

the SGIVT would be developed in a future work.

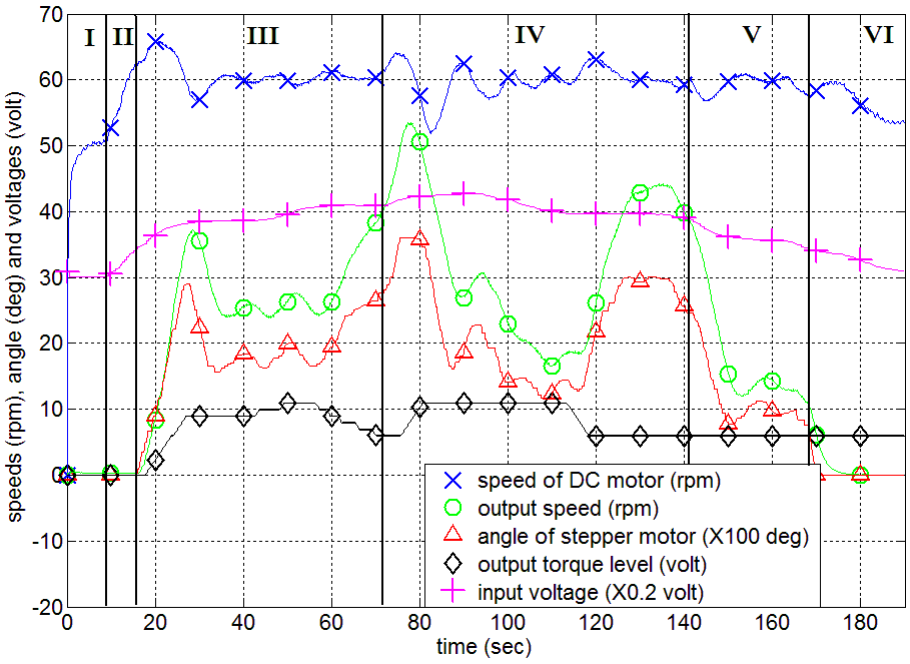

Figure 51: Driving test results of the SGIVT; values of the angle of the stepper motor are scaled down by 100, and those of the input voltage are scaled up by 5

Appendix A: Derivation of Eq. (121) from Eq. (120)

Since $\mathbf{H}_s\mathbf{H}_s^{\mathrm{T}}$ or $\mathbf{H}_s\mathbf{H}_c^{\mathrm{T}}$ are $N \times N$ matrices, using Eq. (88) with $\mathbf{M} = \mathbf{H}_s\mathbf{H}_s^{\mathrm{T}}$ or $\mathbf{M} = \mathbf{H}_s\mathbf{H}_c^{\mathrm{T}}$ and $\mathbf{p} = \Phi$ yields

$$\mathbf{H}_s\mathbf{H}_s^{\mathrm{T}}\hat{\Phi}^{\mathrm{T}} = \hat{\Phi}^{\mathrm{T}}(\mathbf{E}_{2M+1} \otimes \mathbf{H}_s\mathbf{H}_s^{\mathrm{T}}) \tag{193}$$

$$\mathbf{H}_s\mathbf{H}_c^{\mathrm{T}}\hat{\Phi}^{\mathrm{T}} = \hat{\Phi}^{\mathrm{T}}(\mathbf{E}_{2M+1} \otimes \mathbf{H}_s\mathbf{H}_c^{\mathrm{T}}) \tag{194}$$

Noting that

$$(\mathbf{E}_{2M+1} \otimes \mathbf{H}_s\mathbf{H}_s^{\mathrm{T}})\beta_1(\mathbf{G}\mathbf{H}_s)^{\mathrm{T}} = [(\mathbf{E}_{2M+1} \otimes \mathbf{H}_s\mathbf{H}_s^{\mathrm{T}})\beta_1] \otimes [(\mathbf{G}\mathbf{H}_s)^{\mathrm{T}}\mathbf{E}_N] \tag{195}$$

$$(\mathbf{E}_{2M+1} \otimes \mathbf{H}_s\mathbf{H}_c^{\mathrm{T}})\beta_2\mathbf{H}_s^{\mathrm{T}} = [(\mathbf{E}_{2M+1} \otimes \mathbf{H}_s\mathbf{H}_c^{\mathrm{T}})\beta_2] \otimes (\mathbf{H}_s^{\mathrm{T}}\mathbf{E}_N) \tag{196}$$

since $(\mathbf{E}_{2M+1} \otimes \mathbf{H}_s\mathbf{H}_s^{\mathrm{T}})\beta_1$, $(\mathbf{E}_{2M+1} \otimes \mathbf{H}_s\mathbf{H}_c^{\mathrm{T}})\beta_2$, $\mathbf{G}\mathbf{H}_s$ and $\mathbf{H}_s$ are $N \times 1$ column vectors, and using the mixed-product property on right-hand sides of Eqs. (195) and (196) yield

$$(\mathbf{E}_{2M+1} \otimes \mathbf{H}_s\mathbf{H}_s^{\mathrm{T}})\beta_1(\mathbf{G}\mathbf{H}_s)^{\mathrm{T}} = [(\mathbf{E}_{2M+1} \otimes \mathbf{H}_s\mathbf{H}_s^{\mathrm{T}}) \otimes (\mathbf{G}\mathbf{H}_s)^{\mathrm{T}}]\hat{\beta}_1 \tag{197}$$

$$(\mathbf{E}_{2M+1} \otimes \mathbf{H}_s\mathbf{H}_c^{\mathrm{T}})\beta_2\mathbf{H}_s^{\mathrm{T}} = [(\mathbf{E}_{2M+1} \otimes \mathbf{H}_s\mathbf{H}_c^{\mathrm{T}}) \otimes \mathbf{H}_s^{\mathrm{T}}]\hat{\beta}_2 \tag{198}$$

Substituting Eqs. (193) and (194) into Eq. (120), using Eqs. (197) and (198) in the resultant equation, respectively, and using associativity of Kronecker product yield Eq. (121).

Appendix B: Derivation of Eq. (174)

Derivation of Eq. (174.a) is straightforward since $u_x + u_\theta = 0$ is a linear equation. Linearizations of J, $u(\theta,0)$ and r are $J = \bar{J} + \bar{J}_r \Delta r$, $u(\theta,0) = \bar{\omega} + \Delta u(\theta,0)$, and $r = \bar{r} + \Delta r$, respectively, where $\bar{J}$ is J with r evaluated at $\bar{r}$ and $\bar{J}_r = 2J_b\bar{r} + 2J_c\bar{r}f^2$. By eliminating second- and higher-order perturbations, linearization of the left-hand side of Eq. (173.b) is

$$(\bar{J} + \bar{J}_r \Delta r)(\bar{\omega}' + \Delta u_\theta(\theta,0)) = \bar{J}\bar{\omega}' + \bar{J}\Delta u_\theta(\theta,0) + \bar{J}_r\bar{\omega}'\Delta r \tag{199}$$

and linearization of the right-hand side of Eq. (173.b) is

$$\frac{Gr + f_1 - f_2 r}{u(\theta,0)} - \frac{1}{2}J_\theta u(\theta,0) - F_m = \bar{J}\bar{\omega}' + \frac{G - f_2}{\bar{\omega}}\Delta r - \frac{G\bar{r} + f_1 - f_2\bar{r}}{\bar{\omega}^2}\Delta\omega - \frac{\bar{J}_\theta}{2}\Delta\omega - \frac{\bar{J_{\theta r}}\bar{\omega}}{2}\Delta r \tag{200}$$

where $\bar{J}\bar{\omega}' = \frac{G\bar{r} + f_1 - f_2\bar{r}}{\bar{\omega}} - \frac{1}{2}\bar{J}_\theta\bar{\omega} - F_m$, $\bar{J}_\theta$ is J_θ with r evaluated at $\bar{r}$, and $\bar{J_{\theta r}} = 4J_c\bar{r}ff_\theta$. From Eqs. (199) and (200), Eq. (174.b) can be obtained with

$$A = \frac{1}{\bar{J}}\left(-\bar{J}_r\bar{\omega}' - \frac{\bar{J_{\theta r}}\bar{\omega}}{2} + \frac{G - f_2}{\bar{\omega}}\right)$$

$$B = -\frac{1}{\bar{J}}\left(\frac{G\bar{r} + f_1 - f_2\bar{r}}{\bar{\omega}^2} + \frac{\bar{J}_\theta}{2}\right)$$

With $\bar{z} = \frac{2\pi}{\omega_0}$ and linearization of $u(\theta, x)$ being $u(\theta, x) = \bar{\omega} + \Delta u(\theta, x)$, linearization of Eq. (173.c) is

$$\begin{aligned}\Delta r' &= k(\frac{2\pi}{\bar{z}} - \omega_0) + (-k\frac{2\pi}{\bar{z}^2}\Delta z) + k_2[\Delta u(\theta, 0) - \Delta u(\theta, 2\pi)] \\ &= K\Delta z + k_2[\Delta u(\theta, 0) - \Delta u(\theta, 2\pi)]\end{aligned}$$

where $K = -\frac{k\omega_0^2}{2\pi}$. Since $\bar{\omega}(\theta) = \bar{\omega}(\theta + 2\pi)$, Eq. (174.d) can be obtained with $C = -\frac{1}{\bar{\omega}^2}$.

Appendix C: Derivation of the Linear Time-Periodic System in Eq. (179)

Using Eqs. (175)-(178) in Eq. (174) yields

$$\mathscr{I}\eta' = \bar{\mathscr{A}}\eta$$

where

$$\mathscr{I} = \left\{\begin{array}{cc|cc} \mathbf{I}_N & \underline{\mathbf{0}} & \underline{\mathbf{0}} & \underline{\mathbf{0}} \\ \mathbf{T}_h^{\mathrm{T}} & 1 & 0 & 0 \\ \hline \underline{\mathbf{0}}^{\mathrm{T}} & 0 & 1 & 0 \\ \underline{\mathbf{0}}^{\mathrm{T}} & 0 & 0 & 1 \end{array}\right\}$$

$\mathbf{T}_h^{\mathrm{T}} = \{1 \ -1 \ \cdots \ 1 \ -1\}$ is an N^{th}-order row vector, $\mathbf{I}_N$ is the N^{th}-order identity matrix, and

$$\bar{\mathscr{A}} = \left\{\begin{array}{cc|cc} \underline{\mathbf{0}} & -\mathbf{D}_r & \underline{\mathbf{0}} & \underline{\mathbf{0}} \\ B & -B\mathbf{T}_h^{\mathrm{T}} & A & 0 \\ \hline & k_2(\mathbf{T}_0^{\mathrm{T}} - \mathbf{T}_I^{\mathrm{T}}) & 0 & K \\ & C(\mathbf{T}_0^{\mathrm{T}} - \mathbf{T}_I^{\mathrm{T}}) & 0 & 0 \end{array}\right\}$$

The inverse of $\mathscr{I}$ is

$$\mathscr{I}^{-1} = \left\{\begin{array}{cc|cc} \mathbf{I}_N & \underline{\mathbf{0}} & \underline{\mathbf{0}} & \underline{\mathbf{0}} \\ -\mathbf{T}_h^{\mathrm{T}} & 1 & 0 & 0 \\ \hline \underline{\mathbf{0}}^{\mathrm{T}} & 0 & 1 & 0 \\ \underline{\mathbf{0}}^{\mathrm{T}} & 0 & 0 & 1 \end{array}\right\}$$

and

$$\mathscr{A} = \mathscr{J}^{-1}\bar{\mathscr{A}} = \left\{\begin{array}{cc|cc} \underline{\mathbf{0}} & -\mathbf{D}_r & \underline{\mathbf{0}} & \underline{\mathbf{0}} \\ B & \mathbf{T}_h^{\mathrm{T}}\mathbf{D}_r - B\mathbf{T}_h^{\mathrm{T}} & A & 0 \\ \hline & k_2(\mathbf{T}_0^{\mathrm{T}} - \mathbf{T}_I^{\mathrm{T}}) & 0 & K \\ & C(\mathbf{T}_0^{\mathrm{T}} - \mathbf{T}_I^{\mathrm{T}}) & 0 & 0 \end{array}\right\}$$

is a periodic system matrix for Eq. (179). Since the first element in $\mathbf{T}_0^{\mathrm{T}} - \mathbf{T}_I^{\mathrm{T}}$ is zero, the first column $[\underline{\mathbf{0}}^{\mathrm{T}}\ B\ 0\ 0]^{\mathrm{T}}$ and the $(n+2)^{th}$ column $[\underline{\mathbf{0}}^{\mathrm{T}}\ A\ 0\ 0]^{\mathrm{T}}$ are linearly dependent, and one eigenvalue of the transformation matrix for $\mathscr{A}$ is unit. However, this unit eigenvalue is unchanged and not affected by uncertainty since it comes from the introduction of the integral variable $z = \int_{\theta(t)-2\pi}^{\theta(t)} \frac{d\sigma}{\omega}$. Thus, the unit eigenvalue does not change stability of Eq. (179), and it is not considered in searching maximum absolute eigenvalues of the transformation matrix.

References

[1] Manwell, J. F., McGowan, J. G., and Rogers, A. L., 2010. *Wind energy explained: theory, design and application*. John Wiley & Sons.

[2] Ragheb, M., and Ragheb, A., 2011. *Wind Turbines TheoryâThe Betz Equation and Optimal Rotor Tip Speed Ratio. Fundamental and Advanced Topics in Wind Power*. InTech.

[3] Hansen, A., Iov, F., Blaabjerg, F., and Hansen, L., 2004. "Review of contemporary wind turbine concepts and their market penetration". *Wind Engineering,* **28**(3), pp. 247–263.

[4] Muljadi, E., Pierce, K., and Migliore, P., 1998. "Control strategy for variable-speed, stall-regulated wind turbines". In American Control Conference, 1998. Proceedings of the 1998, Vol. 3, IEEE, pp. 1710–1714.

[5] Ko, H.-S., Yoon, G.-G., Kyung, N.-H., and Hong, W.-P., 2008. "Modeling and control of dfig-based variable-speed wind-turbine". *Electric Power Systems Research,* **78**(11), pp. 1841–1849.

[6] Nallavan, G., Dhanasekaran, R., and Vasudevan, M., 2011. "Power electronics in wind energy conversion systemsâa survey across the globe". In Electronics Computer Technology (ICECT), 2011 3rd International Conference on, Vol. 1, IEEE, pp. 416–419.

[7] Miltenovic, V., Velimirovic, M., Banic, M., and Miltenovic, A., 2011. "Design of windturbines drive train based on cvt". *Balk. J. Mech. Transm,* **1**(1), pp. 46–56.

[8] Lechner, G., and Naunheimer, H., 1999. *Automotive transmissions: fundamentals, selection, design and application*. Springer Science & Business Media.

[9] Setlur, P., Wagner, J. R., Dawson, D. M., and Samuels, B., 2003. "Nonlinear control of a continuously variable transmission (cvt)". *IEEE Transactions on control systems technology,* **11**(1), pp. 101–108.

[10] Fischetti, M., 2006. "No more gears". *Scientific American,* **294**(1), pp. 92–93.

[11] Miltenovic, A., Velimirovic, M., Banic, M., and Milovancevic, M., 2008. "Modern trends in development and application of cvt transmitters". *Konstruisanje Maina,* **11**(1), pp. 23–30.

[12] Cotrell, J., 2005. *Assessing the potential of a mechanical continuously variable transmission for wind turbines*. Citeseer.

[13] Gorla, C., and Cesana, P., 2011. "Efficiency models of wind turbines gearboxes with hydrostatic cvt". *Balk. J. Mech. Transm,* **1**(2), pp. 17–24.

[14] Rydberg, K.-E., 1998. Hydrostatic drives in heavy mobile machinery–new concepts and development trends. Tech. rep., SAE Technical Paper.

[15] Muller, H., Poller, M., Basteck, A., Tilscher, M., and Pfister, J., 2006. "Grid compatibility of variable speed wind turbines with directly coupled synchronous generator and hydro-dynamically controlled gearbox". In Sixth International Workshop on Large-Scale Integration of Wind Power and Transmission Networks for Offshore Wind Farms, pp. 307–315.

[16] Asl, H., Azad, N., and McPhee, J., 2012. "Converter characteristics in automatic drivelines: Lock-up clutch and engine braking simulation". *SAE International, Paper*(12PFL-0362).

[17] Liu, J., and Peng, H., 2010. "A systematic design approach for two planetary gear split hybrid vehicles". *Vehicle System Dynamics,* **48**(11), pp. 1395–1412.

[18] Hoeijmakers, M. J., and Ferreira, J. A., 2006. "The electric variable transmission". *IEEE transactions on industry applications,* **42**(4), pp. 1092–1100.

[19] Kerr, J., 2005. All gear infinitely variable transmission. US Patent 6849023B1.

[20] Lee, G. D., 2011. Variable speed transmission with variable orbital path, Feb. 22. US Patent 7,892,129.

[21] Han, K. S., 2013. System and method for providing a constant output from a variable flow input, Mar. 5. US Patent 8,388,481.

[22] Zhu, W., and Wang, X., 2014. "Modeling and control of an infinitely variable speed converter". *Journal of Dynamic Systems, Measurement, and Control,* **136**(3), p. 031015.

[23] Wang, X., and Zhu, W., 2014. "Design, modeling, and simulation of a geared infinitely variable transmission". *Journal of Mechanical Design,* **136**(7), p. 071011.

[24] Wang, X., and Zhu, W., 2016. "Design, modeling, and experimental validation of a novel infinitely variable transmission based on scotch yoke systems". *Journal of Mechanical Design,* **138**(1), p. 015001.

[25] Wang, X., and Zhu, W. "Design and stability analysis of an integral time-delay feedback control combined with an open loop control for an infinitely variable transmission system". *Journal of Dynamic Systems, Measurement, and Control*.

[26] Ross, M., 1997. "Fuel efficiency and the physics of automobiles". *Contemporary Physics,* **38**(6), pp. 381–394.

[27] Ryu, W., and Kim, H., 2008. "Cvt ratio control with consideration of cvt system loss". *International Journal of Automotive Technology,* **9**(4), pp. 459–465.

[28] Yildiz, Y., Annaswamy, A. M., Yanakiev, D., and Kolmanovsky, I., 2011. "Spark-ignition-engine idle speed control: an adaptive control approach". *IEEE Transactions on Control Systems Technology,* **19**(5), pp. 990–1002.

[29] Pesgens, M., Vroemen, B., Stouten, B., Veldpaus, F., and Steinbuch, M., 2006. "Control of a hydraulically actuated continuously variable transmission". *Vehicle System Dynamics,* **44**(5), pp. 387–406.

[30] Pfiffner, R., Guzzella, L., and Onder, C., 2003. "Fuel-optimal control of cvt powertrains". *Control engineering practice,* **11**(3), pp. 329–336.

[31] Wang, X., Li, Z., and Zhu, W., 2016. "Dynamic analysis of a geared infinitely variable transmission". *Journal of Computational and Nonlinear Dynamics*.

[32] Wang, X., and Zhu, W., 2015. "A modified incremental harmonic balance method based on the fast fourier transform and broyden's method". *Nonlinear Dynamics,* **81**(1-2), pp. 981–989.

[33] Sastry, S. S., 2013. *Nonlinear systems: analysis, stability, and control*, Vol. 10. Springer Science & Business Media.

[34] Vidyasagar, M., 1993. *Nonlinear systems analysis*. Prentice-Hall, Inc.

[35] Khalil, H., 2002. *Nonlinear Systems*. Prentice Hall.

[36] Canova, M., Guezennec, Y., and Yurkovich, S., 2009. "On the control of engine start/stop dynamics in a hybrid electric vehicle". *Journal of dynamic systems, measurement, and control,* **131**(6), p. 061005.

[37] Phat, V. N., and Niamsup, P., 2006. "Stability of linear time-varying delay systems and applications to control problems". *Journal of Computational and Applied Mathematics,* **194**(2), pp. 343–356.

[38] Mondie, S., Kharitonov, V. L., et al., 2005. "Exponential estimates for retarded time-delay systems: an lmi approach". *IEEE Transactions on Automatic Control,* **50**(2), pp. 268–273.

[39] Ramrez, M., Villafuerte, R., Gonzlez, T., and Bernal, M., 2015. "Exponential estimates of a class of time–delay nonlinear systems with convex representations". *International Journal of Applied Mathematics and Computer Science,* **25**(4), pp. 815–826.

[40] Cao, J., and Wang, J., 2004. "Delay-dependent robust stability of uncertain nonlinear systems with time delay". *Applied Mathematics and Computation,* **154**(1), pp. 289–297.

[41] Butcher, E. A., and Bobrenkov, O. A., 2011. "On the chebyshev spectral continuous time approximation for constant and periodic delay differential equations". *Communications in Nonlinear Science and Numerical Simulation,* **16**(3), pp. 1541–1554.

[42] Insperger, T., and Stpn, G., 2002. "Semi-discretization method for delayed systems". *International Journal for numerical methods in engineering,* **55**(5), pp. 503–518.

[43] Bayly, P., Halley, J., Mann, B. P., and Davies, M., 2003. "Stability of interrupted cutting by temporal finite element analysis". *Journal of Manufacturing Science and Engineering,* **125**(2), pp. 220–225.

[44] Wang, X., and Zhu, W., 2016. "A new spatial and temporal incremental harmonic balance method for obtaining steady-state responses of a one-dimensional continuous system". *Journal of Applied Mechanics*.

[45] Tsay, M.-F., and Fong, Z.-H., 2005. "Study on the generalized mathematical model of noncircular gears". *Mathematical and computer modelling,* **41**(4), pp. 555–569.

[46] Mook, D., and Nayfeh, A., 1979. *Nonlinear oscillations*. John Wiley & Sons, New York.

[47] Bajkowski, J., and Szempliska-Stupnicka, W., 1986. "Internal resonances effectsâsimulation versus analytical methods results". *Journal of Sound and Vibration,* **104**(2), pp. 259–275.

[48] Lau, S., Cheung, Y., and Wu, S., 1982. "A variable parameter incrementation method for dynamic instability of linear and nonlinear elastic systems". *Journal of Applied Mechanics,* **49**(4), pp. 849–853.

[49] Szempliska-Stupnicka, W., 1978. "The generalized harmonic balance method for determining the combination resonance in the parametric dynamic systems". *Journal of Sound and Vibration,* **58**(3), pp. 347–361.

[50] Lau, S., and Cheung, Y., 1981. "Amplitude incremental variational principle for nonlinear vibration of elastic systems". *Journal of Applied Mechanics,* **48**(4), pp. 959–964.

[51] Lau, S., Cheung, Y., and Wu, S.-Y., 1983. "Incremental harmonic balance method with multiple time scales for aperiodic vibration of nonlinear systems". *Journal of Applied Mechanics,* **50**(4a), pp. 871–876.

[52] Cheung, Y., Chen, S., and Lau, S., 1990. "Application of the incremental harmonic balance method to cubic non-linearity systems". *Journal of Sound and Vibration,* **140**(2), pp. 273–286.

[53] Leung, A., and Chui, S., 1995. "Non-linear vibration of coupled duffing oscillators by an improved incremental harmonic balance method". *Journal of Sound and Vibration,* **181**(4), pp. 619–633.

[54] Sinha, S., and Pandiyan, R., 1994. "Analysis of quasilinear dynamical systems with periodic coefficients via liapunovâfloquet transformation". *International Journal of Non-Linear Mechanics,* **29**(5), pp. 687–702.

[55] Sinha, S., Pandiyan, R., and Bibb, J., 1996. "Liapunov-floquet transformation: Computation and applications to periodic systems". *Journal of Vibration and Acoustics,* **118**(2), pp. 209–219.

[56] David, A., and Sinha, S., 2000. "Versal deformation and local bifurcation analysis of time-periodic nonlinear systems". *Nonlinear Dynamics,* **21**(4), pp. 317–336.

[57] Hsu, C., and Cheng, W.-H., 1973. "Applications of the theory of impulsive parametric excitation and new treatments of general parametric excitation problems". *Journal of Applied Mechanics,* **40**(1), pp. 78–86.

[58] Friedmann, P., Hammond, C., and Woo, T.-H., 1977. "Efficient numerical treatment of periodic systems with application to stability problems". *International Journal for Numerical Methods in Engineering,* **11**(7), pp. 1117–1136.

[59] Raghothama, A., and Narayanan, S., 1999. "Bifurcation and chaos in geared rotor bearing system by incremental harmonic balance method". *Journal of Sound and Vibration,* **226**(3), pp. 469–492.

[60] Raghothama, A., and Narayanan, S., 2000. "Bifurcation and chaos in escape equation model by incremental harmonic balancing". *Chaos, Solitons & Fractals,* **11**(9), pp. 1349–1363.

[61] Huang, J., and Zhu, W., 2014. "Nonlinear dynamics of a high-dimensional model of a rotating euler–bernoulli beam under the gravity load". *Journal of Applied Mechanics,* **81**(10), p. 101007.

[62] Xu, G., and Zhu, W., 2010. "Nonlinear and time-varying dynamics of high-dimensional models of a translating beam with a stationary load subsystem". *Journal of Vibration and Acoustics,* **132**(6), p. 061012.

[63] Ling, F., and Wu, X., 1987. "Fast galerkin method and its application to determine periodic solutions of non-linear oscillators". *International Journal of Non-Linear Mechanics,* **22**(2), pp. 89–98.

[64] Mitra, R., Banik, A., and Chatterjee, S., 2013. "Dynamic stability of time-delayed feedback control system by fft based ihb method". *WSEAS Trans. Appl. Theor. Mech,* **4**(8), pp. 292–303.

[65] Lu, W., Ge, F., Wu, X., and Hong, Y., 2013. "Nonlinear dynamics of a submerged floating moored structure by incremental harmonic balance method with fft". *Marine Structures,* **31**, pp. 63–81.

[66] Broyden, C. G., 1965. "A class of methods for solving nonlinear simultaneous equations". *Mathematics of computation,* **19**(92), pp. 577–593.

[67] Gay, D. M., 1979. "Some convergence properties of broyden's method". *SIAM Journal on Numerical Analysis,* **16**(4), pp. 623–630.

[68] Shen, J., Lin, K., Chen, S., and Sze, K., 2008. "Bifurcation and route-to-chaos analyses for mathieu–duffing oscillator by the incremental harmonic balance method". *Nonlinear Dynamics,* **52**(4), pp. 403–414.

[69] Leung, A., 1989. "Nonlinear natural vibration analysis of beams by selective coefficient increment". *Computational mechanics,* **5**(1), pp. 73–80.

[70] Meirovitch, L., 1997. *Principles and techniques of vibrations*, Vol. 1. Prentice Hall New Jersey.

[71] Tamura, H., Tsuda, Y., and Sueoka, A., 1981. "Higher approximation of steady oscillations in nonlinear systems with single degree of freedom: Suggested multi-harmonic balance method". *Bulletin of JSME,* **24**(195), pp. 1616–1625.

[72] Ferri, A., 1986. "On the equivalence of the incremental harmonic balance method and the harmonic balance-newton raphson method". *Journal of Applied Mechanics,* **53**(2), pp. 455–457.

[73] Guillen, J., and Pierre, C., 1999. "An efficient, hybrid, frequency-time domain method for the dynamics of large-scale dry-friction damped structural systems.". In IUTAM Symposium on Unilateral Multibody Contacts, Springer, pp. 169–178.

[74] Wereley, N. M., 1990. "Analysis and control of linear periodically time varying systems". PhD thesis, Massachusetts Institute of Technology.

[75] Chivukula, R. K., and Reznik, Y. A., 2011. "Fast computing of discrete cosine and sine transforms of types vi and vii". In SPIE Optical Engineering+ Applications, International Society for Optics and Photonics, pp. 813505–813505.

[76] Johnson, D. Chebyshev polynomials in the spectral tau method and applications to eigenvalue problems.

[77] Mote, C., 1966. "On the nonlinear oscillation of an axially moving string". *Journal of Applied Mechanics,* **33**(2), pp. 463–464.

[78] Sinha, S., and Butcher, E. A., 1996. “Solution and stability of a set of pth order linear differential equations with periodic coefficients via chebyshev polynomials”. *Mathematical Problems in Engineering,* **2**(2), pp. 165–190.